Mixing, Mass Transfer and Cell Production in a Continuous Bioreactor

by

Shu Fang

A dissertation submitted to the Graduate Faculty of
Auburn University
in partial fulfillment of the
requirements for the Degree of
Doctor of Philosophy
Auburn, Alabama
August 4th, 2018

Key words: computational fluid dynamics, multiphase bioreactor, oxygen transport phenomena, roller bottle, cell cultivation, spiroid

Approved by

Dr. Thomas Hanley, Chair, Professor of Chemical Engineering
Dr. R. Eric Berson, Professor of Chemical Engineering, University of Louisville
Dr. Allan David, Associate Professor of Chemical Engineering
Dr. Mario Eden, Professor of Chemical Engineering
Dr. Paul Todd, Chief Scientist Emeritus, Techshot, Inc.

Abstract

This research investigated a novel continuous bioreactor which has the advantages of enhanced oxygen transfer, low shear stress, ease of operation and scalability. The bioreactor showed significant improvement in gas-liquid and medium mixing through its unique design, leading to higher cell production. The bioreactor had both an outer shell cylinder and an inner core cylinder, each with adjustable rotational velocities to control the mixing in the reactor. Inlet flows were controlled to provide additional medium and oxygen to the reactor volume. Moreover, a spiroid tube was attached to the wall of the outer cylinder, providing enhanced gas-liquid interfacial area thus improving oxygen transfer.

Computational fluid dynamics (CFD) simulations were performed to analyze the resulting hydrodynamic properties (shear stress, velocity distribution, eddy viscosity and turbulence kinetic energy) in the multiphase bioreactor, and the results were used to determine the optimum operating conditions for oxygen transfer experiments. Mathematical models were also developed to simulate the experimental dynamic behaviors of oxygen transfer process and to obtain the volumetric mass transfer coefficients (k_La) in the bioreactor at a variety of operating conditions operating conditions.

To increase the potential for cell production, this bioreactor was further scaled up by 9 nine times, from 1.11×10^{-4} m^3 to 0.986×10^{-3} m^3. Oxygen measurements were conducted to characterize the bioreactor with and without spiroid. The comparisons proved the advantages of using spiroid as a method to improve oxygen transfer performance or adding spiroid to the

bioreactor could help reduce the oxygen saturation time by two times. Furthermore, biological tests (using E. coli, K91BlueKan) were used to further verity the potentials in the cellular production of this bioreactor under various operating conditions (batch and continuous modes, different rotational rates and different flow rates). By measuring the cell growth and glucose consumptions for the microorganism in the bioreactor with and without spiroid under different operating conditions, the results not only further demonstrated the advantages of using the spiroid in oxygen delivery (increase 15% cells in the batch and reduced 33% operating time), but also showed great potentials in harvesting cells continuously.

Acknowledgments

First, I would like to express my sincere gratitude to my advisor Dr. Thomas R. Hanley for his support to my Ph.D. study. Without his guidance, this Ph.D. study would not be completed. His input, patience and immense knowledge helped me establish the research skills and navigate me through challenges and difficulties occurred in the project.

I would also like to thank Dr. Paul W. Todd for his supervision, paper edition, and technical support. Besides, my sincere thanks also go to Dr. Allan E. David, who provided microorganism strains and the relative analytical instruments for my biological experiments. I would also like to extend my thanks to Dr. Young Suk Choi for the cell culture training. Moreover, I would like to acknowledge my committee members Dr. R. Eric Berson, Dr. Allan E. David, Dr. Mario Eden, Dr. Paul W. Todd and my university reader Dr. Anthony G. Moss for their insightful comments and suggestions.

I thank all the graduate students (previous and present) in my group for their hard work and help. I would also like to thank my friends here in Auburn for their support and accompany that make the life in Auburn delightful.

Last but not the least, my sincere thanks go to my parents. Without their relentless love, continuous supports and encouragements, I would not be able to complete this journey.

Table of Contents

List of Tables

List of Figures

List of Abbreviations

c_{L0}	initial dissolved oxygen concentration in liquid phase, mol·L^{-1}
c_L	dissolved oxygen concentration in liquid phase (water), mol·L^{-1}
c_L^*	saturated oxygen concentration in liquid phase at certain temperature, mol·L^{-1}
c_f	final dissolved oxygen concentration in the bioreactor, mol·L^{-1}
c_{in}	dissolved oxygen concentration entering spiroid loop, mol·L^{-1}
c_{out}	dissolved oxygen concentration exiting from spiroid, mol·L^{-1}
C_1	constant, $C_1 = max\left[0.43, \frac{\eta}{\eta+5}\right]$
$C_{1\varepsilon}$	constant, 1.44
C_2	constant, 1.9
$C_{3\varepsilon}$	constant, $C_{3\varepsilon} = tanh\left\|\frac{v_{//}}{v_{\perp}}\right\|$
F_{Nk}	force per unit volume which exerts on the inclusion, N·m^{-3}
$F_{O_2,In}$	molar flow rate into the spiroid tube, mol·s^{-1}
$F_{O_2,Out}$	molar flow rate out of the spiroid tube, mol·s^{-1}
g	gravitational acceleration, m·s^{-2}
g_i	ith direction component of the gravitational vector, m·s^{-2}
G_b	generation term due to the buoyancy, $G_b = \beta g_i \frac{\mu_t \partial T}{Pr_t \partial x_i}$ or

	$G_b = -g_i \frac{\mu_t \partial \rho}{\rho Pr_t \partial x_i}$ (for idea gases), J·(s^{-1}·m^{-3}) or kg·(m^{-1}·s^{-3})
G_k	generation term due to the mean velocity gradients, $G_k = -\rho \overline{v_i' v_j'} \frac{\partial v_j}{\partial x_i}$ or $G_k = \mu_t S^2$ (Boussinesq hypothesis), J·(s^{-1}·m^{-3}) or kg·(m^{-1}·s^{-3})
I_N	mass interaction term, kg· (m^{-3}·s^{-1})
k	turbulence kinetic energy per unit mass, J· kg^{-1} or m^2·s^{-2}
$k_L a$	volumetric gas-liquid mass transfer coefficient, s^{-1}
$k_L a_C$	volumetric gas-liquid mass transfer coefficient in bioreactor chamber, s^{-1}
$k_L a_{sp}$	volumetric gas-liquid mass transfer coefficient in spiroid loop, s^{-1}
RPM	rotational velocity of the reactor, round per minute
S_{ij}	mean strain rate, $S_{ij} = \frac{1}{2}\left(\frac{\partial v_j}{\partial x_i} + \frac{\partial v_i}{\partial x_j}\right)$, s^{-1}
S_k	user-defined source term, J· (s^{-1}·m^{-3}) or kg· (m^{-1}·s^{-3})
S_ε	user-defined source term, J· (s^{-1}·m^{-3}) or kg· (m^{-1}·s^{-3})
t	time, s
v	volumetric flow rate through spiroid loop, L·s^{-1}
$v_{//}$	component of flow velocity parallel to the gravitational vector, m·s^{-1}
$v_\perp$	component of flow velocity perpendicular to the gravitational vector, m·s^{-1}
$\overrightarrow{v_N}$	velocity vector of phase N, m·s^{-1}

V_r	liquid volume of bioreactor, m^3
V_{sp}	liquid volume of spiroid tube, m^3
X	biomass concentration, dry weight per unit volume, $g \cdot L^{-1}$
Y_M	effects from the fluctuating dilatation in the compressible turbulence on the overall dissipation rate, $Y_M = 2\rho\varepsilon M_t^2$, $J \cdot (s^{-1} \cdot m^{-3})$ or $kg \cdot (m^{-1} \cdot s^{-3})$

Greek Letters

α_N	volume fraction of phase N, percent
δ_N	constant, 0 for the disperse phase and 1 for the continuous phase
ε	dissipation rate, $m^2 \cdot s^{-3}$
η	constant, $\eta = S\frac{k}{\varepsilon}$
μ	molecular dynamic viscosity, Pa·s
μ_t	turbulent or eddy viscosity, Pa·s
ν	kinematic viscosity, $m^2 \cdot s^{-1}$
ρ_N	density of phase N, $kg \cdot m^{-3}$
σ_k	turbulent Prandtl number for k, $\sigma_k = 1.0$
σ_ε	turbulent Prandtl number for ε, $\sigma_\varepsilon = 1.2$
τ_{ki}	shear stress, Pa
τ	mean residence time, hr

Subscripts

i, j, k	three directions (x, y, z axis) separately

Chapter 1 - Introduction

There have always an interest focusing on increasing cell survival rate, and extending cell lines to large scale production, since the secretions of cells, such as enzymes, antibodies, hormones, and other biological products, including even the cells themselves, are considered to have high commercial and medical potential. Various type of bioreactor have been developed and modified in order to satisfy the high requirements of productivity and viability for different types of cells. Advantages and disadvantages have already been discussed in many publications (Bareither and Pollard, 2011; King and Miller, 2007; Pörtner et al., 2005). Despite of different designs, the goals always lay on providing optimal living conditions for cell growth and relative products generation.

Mass transfer are normally one of the severe issues in the large scale and leads to poor cell growth (Chu and Robinson, 2001; Gill et al., 2008; Kallos et al., 2003; Marks, 2003; Schmidt, 2005; Shuler et al., 1990). Oxygen transfer mechanism are essential in cell production process. Appropriate amount of oxygen transported to the system aids cell productivity and viability, since oxygen plays an important role in cell metabolism. However, when operating the bioreactor in certain conditions in order to get high mixing result, shear stress should be a central issues and taken into serious account. Cell walls or the plasma membrane may not be strong enough to bear the shear forces from rapidly flowing the outside fluids, and so high shear forces will reduce the amount of living cells. A bioreactor capable of an optimum mixing environment, providing appropriate shear forces and high oxygen transfer, sufficiently high nutrient usage or low required input nutrient, and easy to scale up, is likely to be of significant economic potential in both industry and biomedical research.

The objective of this research is to investigate the use of an automated, horizontally-rotating bioreactor consisting of a rotating outer cylindrical shell and a counter-rotating core. Each component is equipped with adjustable rotational velocities to control the mixing and shear. This bioreactor can be operated either in batch or continuous mode. Excellent oxygen transport phenomena as measured by oxygen monitor were accomplished by the use of rotational cylinders and spirals attached to the bioreactor. Cell growth were measured. This research effort was in part based on simulation and in part, on empirical effort.

In the simulation computational fluid dynamic (CFD) simulations and mathematical simulations were performed for the small scale of the bioreactor in order to determine the range of flow patterns likely to occur. Oxygen transfer coefficients in the spiral and the bioreactor were calculated and measured based on gas-liquid mechanics. Simulations were conducted for multiphase fluids with various operating conditions in order to simulate the actual reaction environment in the bioreactor. A suitable range of rotational velocity and optimized bioreactor size was obtained from the simulation results.

During the experimental phase the simulation outcomes were tested. A bioreactor with spiroid attached to the outer cylinder was built and then operated at selected operating conditions. The bioreactor was scaled up in operation by nine fold, from 1.109×10^{-4} m^3 to 0.944×10^{-3} m^3 to enable evaluation of its potential for high throughput cell production. The performance of this bioreactor was evaluated with regard to oxygen transfer and cell growth. The experimental results were used to provide feedback to the simulation and to help improve the system. We feel that our experimental results can be used to further modify the bioreactor and bioreactors in general so as to enable the ability of large scale in industry.

Reference

Bareither, R., Pollard, D., 2011. A review of advanced small-scale parallel bioreactor technology for accelerated process development: Current state and future need. Biotechnol. Prog. 27, 2–14.

Chu, L., Robinson, D.K., 2001. Industrial choices for protein production by large-scale cell culture. Curr. Opin. Biotechnol. 12, 180–187.

Gill, N.K., Appleton, M., Baganz, F., Lye, G.J., 2008. Quantification of power consumption and oxygen transfer characteristics of a stirred miniature bioreactor for predictive fermentation scale-up. Biotechnol. Bioeng. 100, 1144–1155.

Kallos, M.S., Sen, A., Behie, L.A., 2003. Large-scale expansion of mammalian neural stem cells: A review. Med. Biol. Eng. Comput. 41, 271–282.

King, J.A., Miller, W.M., 2007. Bioreactor development for stem cell expansion and controlled differentiation. Curr. Opin. Chem. Biol. 11, 394–398.

Marks, D.M., 2003. Equipment design considerations for large scale cell culture. Cytotechnology 42, 21–33.

Pörtner, R., Nagel-Heyer, S., Goepfert, C., Adamietz, P., Meenen, N.M., 2005. Bioreactor design for tissue engineering. J. Biosci. Bioeng. 100, 235–245.

Schmidt, F.R., 2005. Optimization and scale up of industrial fermentation processes. Appl. Microbiol. Biotechnol. 68, 425–435.

Shuler, M.L., Cho, T., Wickham, T., Ogonah, O., Kool, M., Hammer, D.A., Granados, R.R., Wood, H.A., 1990. Bioreactor Development for Production of Viral Pesticides or Heterologous Proteins in Insect Cell Cultures. Ann. N. Y. Acad. Sci. 589, 399–422.

Chapter 2 – Literature Review

2.1. Introduction

The scientific and economic potentials of the market related to cell production are always so great that they attract both research and industrial areas to put continuous efforts in order to innovate and improve the technologies involved in cell culture. In general, the appropriate selection and the novel reformation of bioreactors are the most commonly used methods to increase production.

Bioreactors can be simply defined as devices that simulate or provide the most favorable conditions for specific cell lines. Various bioreactors (e. g. bubble columns, agitated reactors, roller bottles, newly developed membrane bioreactors) have been applied in engineering and industrial production. Biological and biochemical experiments conducted in specific devices are controlled under a range of operating conditions in order to seek an optimal method for various fields. Bioreactor can be used to produce pharmaceuticals (e. g. antibodies, hormones, viral vaccines), solve environmental issues (e. g. wastewater treatment), process food, provide energy source (e. g. conversion of corns to alcohol) and supply cells and tissues lines (Martin et al., 2004).

Before using or designing bioreactor systems that are suitable for cell growth, an understanding of several properties in the cell culture is essential. To assist in the selection and improving process, cell properties (e. g. structure), physicochemical conditions, fundamental mechanisms of cell culture, and potential cell damage associated with fluid mechanical effects are commonly considered (Papoutsakis, 1991).

The selection and reformation of bioreactors will always be closely related to the effectiveness, quality of products, and the production cost especially in large-scale commercial

application. For instance, a fed-batch process is one of the most attractive processes for large scale production of monoclonal antibodies (MAbs) because of its simple operation, reliability and flexibility for implementation. By extending the cell culture longevity, maintaining high specific antibody secretion rates via appropriate nutrient supplementation, minimizing the waste production (such as inhibitory growth byproducts) and controlling environmental conditions (such as pH), high yield could be achieved in fed-batch reactors (Bibila and Robinson, 1995). Nevertheless, when comparing fed-batch reactor with perfusion operation modes, the cell densities and volumetric productivities achieved in perfusion culture are much higher than that in fed-batch system, though perfusion operation could have increased possibility of equipment failure, difficult facility design and product contamination.

Once the specific bioreactors are selected, operating conditions will then be a main concern. Generally, pH, pressure, temperature, medium selection, continuous nutrient supply, nutrient concentration, oxygen transfer phenomenon, hydrodynamic shear stress effects, overdose products, and wastes removal are common essential factors that should be taken into account when in the process of optimization. The following review will emphasize some of the key factors above.

2.2. Hydrodynamic Shear Stress Effects on Cell Cultures

Hydrodynamic forces, often referred to as shear, are known to have influences on cell shape and membrane structure, which in turn affect the physiology (e. g. metabolism of cells, protein synthesis, even DNA and RNA mechanism) (Abu-Reesh and Kargi, 1989; Ben-Ze'ev et al., 1980; Dewey et al., 1981; Farmer et al., 1978; Folkman and Moscona, 1978; Stathopoulos and Hellums, 1985). The existence of shear stress cannot be avoided in most bioreactors.

Generally, the damage of shear stress resulting from turbulent flow is more severe than that from laminar flow (Chisti, 2001). The sensitivity of cells to shear stress may vary with the stage of growth, the cultivation culture, and operation conditions (Petersen et al., 1988).

Mixing is essential for bioreactors to increase oxygen transfer and maintain a relatively uniform environment for cell growth. However, even appropriate mixing can result in shear stress levels that could cause cell damage. Hence, a balance between maximizing the oxygen transport rate and minimizing the detrimental effect on cells still remains a main challenge in order to get high cell density and large-scale application in industry. Thorough explanations of the mechanisms of cells damage (especially in animal cells due to the lack of a cell wall, making them more sensitive and vulnerable) associated with fluid mechanical forces will help establish new ideas on bioreactor design and scale-up.

Cell can be grown in immobilized cultures or homogeneous suspensions. Each culture has its own advantages in increasing cell growth rate. Though the immobilized system increases the surface area per unit reactor volume for cell attachment and provides reduced fluid stresses, the suspension culture is more suitable to be applied in large-scale production due to the relatively easier operation process control and lower cost.

Using micro carriers is considered to be one of the promising technologies and is normally observed in immobilized cell cultures where cells are anchorage-dependent. Micro carriers are typically micrometer beads, and can maintain suspension in the fluids. The bulk fluid, typically in turbulent flow, contributes most to the effect on cells in bioreactors with micro carriers (Cherry and Papoutsakis, 1990; Croughan et al., 1987). In micro carrier bioreactors, interactions can be summarized into bead-to-fluid, bead-to-bead, and bead-to-bioreactor. The interaction of bead-to-fluid usually is very closely associated with bead-to-bead interaction.

Experimental data and theoretical models strongly suggest that bead-to-fluid (with small turbulent eddies) interaction could be counted as a damaging source to cells, and that the bead-to-bead interaction was mainly responsible for cell damage in micro carrier bioreactors in the condition of intense-agitation, while the negative effect from bead-to-bioreactor interaction could be negligible (Cherry and Papoutsakis, 1986; Cherry and Papoutsakis, 1988; Cherry and Papoutsakis, 1989; Cherry and Papoutsakis, 1990; Croughan et al., 1987; Komasawa et al., 1974).

In suspension culture, shear stress from gas bubbles is problematic for cells. The shear stress effects on cells resulting from the bulk fluid are normally treated as small, except the case of very high agitation rates, which can be above 700 RPM for hybridoma cells without a vortex and bubble entrainment (Kunas and Papoutsakis, 1990). It has also been demonstrated that rising bubbles generate insignificant shear stress (Tramper et al., 1987). Intensive shear stress generated by the bursting gas bubbles at the air-liquid interface (or known as the air-liquid interfacial effect) causes the dominant detriment to animal cells (Handa et al., 1987; Oh et al., 1992; Wu, 1995; Wudtke and Schiigerl, 1987). For sparged and agitated bioreactors with suspended animal cells important considerations include appropriate location of the gas sparger and selection of the impeller (which suspends the cells and gently mixes the fluid). It is important to keep the average energy dissipation rate for impeller below 1.0×10^3 W m^{-3} (Chisti, 2000).

A bursting gas bubble could be divided into the part above the interface (bubble film cap) and the part below the interface (bubble cavity), with the latter one occupying the higher portion in total surface area, and thus bubble cavity is the main region that kills cells (Wu, 1995). In addition, the size of gas bubbles should also be taken into account when other parameters

remained constant. Normally, larger bubbles would have a less damaging influence on cells than smaller ones. Though smaller bubbles are more rigid, smaller bubbles have a greater specific killing volume ($v_d = \frac{6V_d}{\pi d_b^3} = k_2 a_b$,where $a_b$is specific interfacial area of the bubble and k_2 is a constant with the dimension of length.), thus causing higher death rates of cells (Wu and Goosen, 1995). To protect cells, medium additives, which may be divided into two categories based on the nutritional functions (i. e. bioactive materials and neutral polymers), could be applied either to reduce the contact between bubbles and cells or to strengthen cell membranes, thus decreasing cell death and allowing higher growth of cells (Chattopadhyay et al., 1995; Cherry and Papoutsakis, 1990; Goldblum et al.,; Handa-Corrigan et al., 1989; Handa et al., 1987; Jordan et al., 1994; Murhammer and Goochee, 1990; Ramírez and Mutharasan, 1990; Zhang et al., 1992). Other than bubble rupture, cells could also be killed by foam entrapment due to film drainage and rupture (Papoutsakis, 1991; Wu, 1995).

2.3. Interphase Mass Transfer

Oxygen is one of the most important factors for aerobic bioprocesses. Aerobic bioprocesses normally takes place in the aqueous phase where the oxygen solubility could be low due to ionic salts and nutrients (Suresh et al., 2009). Hence, the growth of almost any microorganisms is limited to the amount of oxygen transferred (or, oxygen transfer rate, OTR). An increase of amount of dissolved oxygen will result in the increase of secondary metabolites of cells, while the limited oxygen will lead to the decrease of metabolic rate (Vardar and Lilly, 1982).

Oxygen transfer rate may be influenced by various parameters including the physical properties of gas and liquid, operational conditions, choice of bioreactor and presence of biomass

(Garcia-Ochoa and Gomez, 2009). Generally, interphase mass transfer could be summarized as three steps: the transfer of oxygen from the bulk air to the interface of air and water, across the interface, and from the interface to the bulk water. To simplify the gas-liquid mass transfer, a two-film model (see Figure 2-1) or a two-resistance theory proposed by Whitman could be used appropriately (Whitman, 1923). According to the theory, oxygen transfer rate between phases is controlled by the diffusion rate, and lead to the equilibrium at the interphase all the time. The two resistances are the diffusion from the bulk gas phase to the interface and the diffusion from the interface to the bulk liquid phase as shown in Figure 2-1.

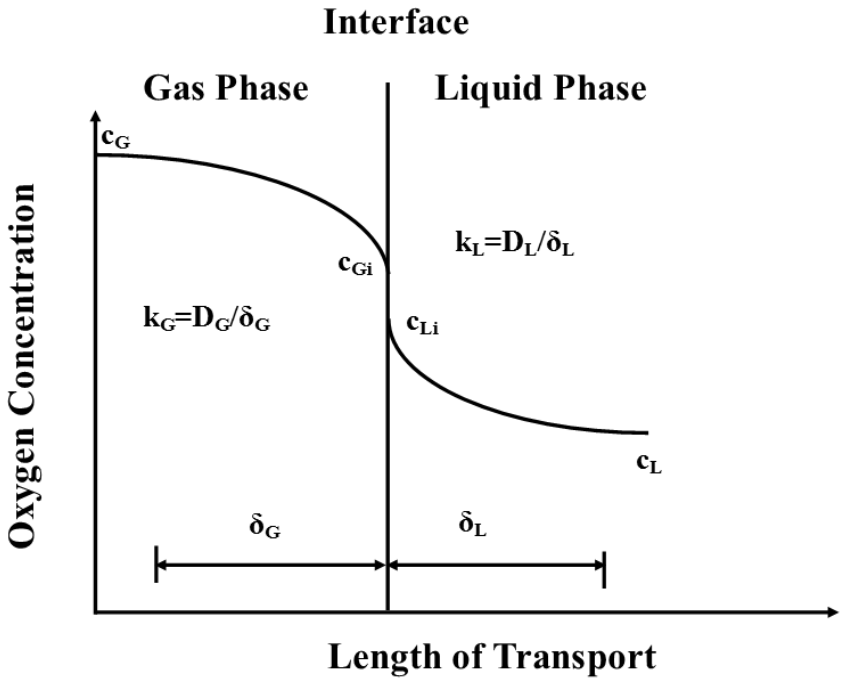

Figure 2.1. Schematic representation of gas-liquid mass transfer (Garcia-Ochoa and Gomez, 2009).

In Figure 2.1, the bulk gas phase concentration of oxygen is c_G, which is normally represented by p_G, the bulk gas oxygen partial pressure. Similarly, the interface gas phase concentration c_{Gi} is represented by p_i (the index i refers to interface), which is in equilibrium

with the interface liquid concentration c_{Li}. The oxygen concentration in the bulk liquid phase is c_L, and the interface liquid phase concentration is c_{Li}. The two interface (gas/liquid) concentrations are in equilibrium and could be related by Henry's Law ($p_i = H * c_{Li}$, where H is the Henry's constant with units of m^3 Pa mol^{-1}). Henry's law states the amount of gas dissolved in the liquid is proportional to the equilibrium partial gas pressure at constant temperature (Henry, 1803). The gas and liquid film thicknesses are denoted by δ_G and δ_L, respectively. D is the diffusion coefficient (the index G and L refer to gas and liquid) (Whitman, 1923).

The molar flux of species is known to be product of driving force (concentration difference) by the mass transfer coefficient. Also, the transport of oxygen flux through gas phase and water phase should be equal at steady-state. Thus, it may be written as (Whitman, 1923):

$$J_{O_2} = k_G(p_G - p_i) = k_L(c_{Li} - c_L) \quad (2\text{-}1)$$

where, J_{O_2} is the molar flux of oxygen (mol m^{-2} s^{-1}); k_G (mol m^{-2} s^{-1} Pa^{-1}) and k_L (m s^{-1}) are the local or individual mass transfer coefficients (the index G and L refer to gas and liquid respectively); p_G (Pa), p_i (Pa), c_{Li} (mol m^{-3}) and c_L (mol m^{-3}) were described as before.

Due to the difficulty of measuring the partial pressure and concentration interface, the molar flux could be rewritten by using the overall mass transfer coefficients, which account for the entire diffusional resistance in both sides of interface (Garcia-Ochoa and Gomez, 2009; Whitman, 1923):

$$J_{O_2} = K_G(p_G - p^*) = K_L(c^* - c_L) \quad (2\text{-}2)$$

where, K_G (mol m^{-2} s^{-1} Pa^{-1}) and K_L (m s^{-1}) are overall mass transfer coefficients; p^* (Pa) is the theoretical partial oxygen pressure in equilibrium with the bulk liquid phase (or, $p^*$is in equilibrium with c_L), and p^* does not have any physical existence in the system; c^* (mol m^{-3}) is

the oxygen saturation concentration in equilibrium with the bulk gas phase (or, $c^*$is in equilibrium with p_G); p_G (Pa) and c_L (mol m^{-3}) were described as before.

The overall mass transfer coefficients may be related to the local mass transfer coefficients by introducing Henry's constant. Applying Henry's Law, the theoretical partial oxygen pressure p^* is in equilibrium with the bulk liquid phase oxygen concentration by:

$$p^* = Hc_L \tag{2-3}$$

Similarly, the bulk gas oxygen partial pressure p_G is in equilibrium with the oxygen saturation concentration c^* by:

$$p_G = Hc^* \tag{2-4}$$

Also, the interphase partial pressure p_i is in equilibrium with the interface liquid concentration c_{Li} by:

$$p_i = Hc_{Li} \tag{2-5}$$

Rewriting Equation 2-2 using the latter part as:

$$\frac{1}{K_L} = \frac{(c^* - c_L)}{J_{O_2}} \tag{2-6}$$

Rearranging Equation 2-6 as:

$$\frac{1}{K_L} = \frac{(c^* - c_{Li})}{J_{O_2}} + \frac{(c_{Li} - c_L)}{J_{O_2}} \tag{2-7}$$

Substituting Equation 2-1, 2-4 and 2-5 into Equation 2-7 yields:

$$\frac{1}{K_L} = \frac{(p_G - p^*)}{HJ_{O_2}} + \frac{1}{k_L} = \frac{1}{Hk_G} + \frac{1}{k_L} \tag{2-8}$$

To relate K_G with k_G and k_L, a similar equation could be derived:

$$\frac{1}{K_G} = \frac{1}{k_G} + \frac{H}{k_L} \tag{2-9}$$

For the case when the gas is very soluble in the liquid, Henry's constant is very small. From Equation 2-9, as the second term of the right part could be neglected, the overall mass transfer coefficient K_G is equal to the local mass transfer coefficient k_G. Since the major resistance to mass transfer resides within the gas phase, this system is gas-phase controlled.

If the gas is relatively insoluble in the liquid, or Henry's constant is very large, the overall mass transfer coefficient K_L is equal to the local mass transfer coefficient k_L as from Equation 2-8. In the other words, the principal resistance to mass transfer lies in the liquid side, and the system is called to be liquid-phase controlled.

Taking into account that oxygen is rather insoluble in water, the system should be liquid phase controlled, and K_L is equal to k_L. The oxygen transfer rate per unit volume (OTR) N_{O_2} (mol m^{-2} s^{-1}) from gas to liquid could be achieved by multiplying the molar flux of oxygen J with gas-liquid interface area per liquid volume, a (m^{-1}):

$$OTR = N_{O_2} = k_L a(c^* - c_L) \qquad (2\text{-}10)$$

Equation 2-10 is commonly seen in various papers related to measurement of oxygen transfer.

The mass balance for the dissolved oxygen in the system could be thus established as:

$$\frac{dc}{dt} = OTR - OUR \qquad (2\text{-}11)$$

where, $\frac{dc}{dt}$ is the accumulation term of the oxygen rate and OUR represents the oxygen uptake rate which can be expressed as the product of the specific oxygen uptake rate per unit mass of microorganisms r and the biomass concentration C_x.

In the absence of microorganisms or with non-respiring cells, in other words, for the case that the OUR is zero, Equation 2-11 could be rewritten as:

$$\frac{dc}{dt} = k_L a(c^* - c_L) \quad (2\text{-}12)$$

As it is difficult to measure k_L and a separately, the product $k_L a$, the volumetric mass transfer coefficient, is utilized to analyze oxygen transport in the system. The values of $k_L a$ could be affected by many factors, such as measurement methods, presence of biomass, selection of bioreactors and viscosity of the medium. Various methods could be used to determine the mass transfer coefficient, such as sulfite oxidation method (Harris and Roper, 1964; Hermann and Walther, 2001; Linek and Vacek, 1981; Ruchti et al., 1985; Waal and Okeson, 1966; Westerterp et al., 1963), the gassing-out method (Gayik, 2001; Puthli et al., 2005; Suijdam et al., 1978; Tribe et al., 1995; Veglio et al., 1998; Yoshihito et al., 1997), the dynamic method (Amanullah et al., 1998; Bandyopadhyay et al., 1967; Ducros et al., 2009; Kilian et al., 1983; Payne et al., 1990), the respiration activity monitoring system (RAMOS) method (Anderlei et al., 2004; Anderlei and Büchs, 2001; Jeude and Dittrich, 2006; Losen et al., 2004; Peter et al., 2004; Scheidle et al., 2007; Seletzky et al., 2007; Stockmann et al., 2003), glucose oxidase method (Duetz and Witholt, 2004), catechol 2,3-dioxygenase (C23O) (Ortiz-Ochoa et al., 2005). Different methods can result in slightly different values.

The sulfite oxidation and the gassing-out methods are used most commonly to determine the volumetric mass transfer coefficient ($k_L a$). Sulfite oxidation method can be used to carry out mass transfer measurement in small scale bioreactors and miniature bioreactors with up to 1-mL volume (e. g. microtiter plates) (Hermann and Walther, 2001). The drawbacks of using sulfite oxidation is due to the high salt concentration and the high surface tension that leads to the underestimation of the oxygen transfer rate (Duetz, 2007). The application of the gassing-out method is limited to the slow response time of the electrode to reflect the true changes of oxygen

rate (Tribe et al., 1995). Additionally, the gassing-out method is also difficult to carry out the measurement in microtiter plates (Suresh et al., 2009).

The measurement of oxygen concentration can be carried out by using zirconia, electrochemical, laser cells and optical sensors. A zirconia sensor could provide an output voltage corresponding to the proportion of oxygen in the fluid by using a solid-state electrochemical fuel cell (Suresh et al., 2009). A Clark-type oxygen sensor is commonly used in the electrochemical systems in large scale cases. The output current states the partial pressure of oxygen (Fraden, 1996). However, the conventional oxygen electrodes were not applicable in small scale bioreactors. In recent years, optical sensors based on luminescence methods gained particular interests in miniature bioreactors despite their high cost and the need for controlling and analyzing data using software and computer. An optical sensor uses oxygen sensitive dyes to measure oxygen amount and was not affected by flow rate, agitation speed and magnetic field. (Bacon and Demas, 1987; Bambot et al., 1994; John et al., 2003; Klimant and Wolfbeis, 1995).

2.4. Oxygen Transfer in Various Bioreactors

Many innovative methods have been used to improve the amount of dissolved oxygen, including the use of various bioreactors (e. g. stirred reactor, bubble column, shaking flasks (Maier et al., 2001; Maier et al., 2004), gas-lift bioreactors), introducing oxygen enriched air to the system, using hyperbaric air to aerate the bioreactor (Belo et al., 2003), or adding an organic phase (often called oxygen vectors) to the system (Ede et al., 1995).

Fleischaker and Sinskey (1981) proposed a possible method of using membrane oxygenation to provide oxygen for large-scale cell production under micro carrier cultures. The membrane oxygenation was accomplished by passing air through a silicone rubber tube (length,

4m; ID, 0.058 inches; OD, 0.077 inches) (Fleischaker and Sinskey, 1981). Experimental figures for vessels without a silicone rubber tube at different volumes indicated that the mass transfer coefficient for a specific volume had an approximate equation ($k_L a = 0.414 \frac{N}{V^{2.05}}$, where N is the agitator speed and V is the volume). They also concluded from the more gradual slope of curve for the vessel (14 L) with a tube that the oxygen transfer rate across the tube was less sensitive than that across the vessel liquid surface and substantial (0.6 mmol O_2 per atm-meter of tubing-h). Additionally, their data suggested that 5-liter was the limit for the growth of FS-4 cells in micro carrier culture without additional aeration, however, 10 liters of FS-4 cell cultures with a density of more than 10^6 cells per ml could be achieved and aerated by using one meter of tubing. Moreover, this method could be absolutely capable of aerating FS-4 cell cultures with a limit of less than 1,000 liters, which was quite promising in industrial application.

Mammalian cells are normally cultivated by using traditional flasks or dishes that provide 2-D growth environment for cells. However, cells grown in this environment tend to dedifferentiate and lose the special features of the original tissues that they were derived from. 3-D cell-to-cell and cell-to-extracellular matrix interactions are proved to be important for the differentiation and future therapeutic applications. Rotating bioreactors with low rotational rates (such as roller bottles) can be used to mimic the natural 3-D cell growth environment. Roller bottles are widely used in cell fermentation despite their difficulties in scale- up. Low rotational rates will minimize the damaging mechanical effects of turbulence and shear stress and improve the mixing of media and mass transfer, all leading to higher cell density. The operation of rotating vessels is conducive to the formation of 3-D cell structure through aggregating cells to the microcarriers or the extracellular matrix. To increase the cell growth surface area and reduce

the cost of obtaining new roller bottles, the use of a foamed, textured or woven liner or sleeve could also be inserted to the roller bottle (Mussi and Gray, 1984)

Mak et al. (1990) used a roller bottle (internal diameter, 7 cm; height, 11.5 cm) to obtain a higher production of *Monascus* (a fungus) pigments compared to the production from batch submerged and agar surface cultures. Fungal colonies which grew on the rotating vessel wall as expected were found to be maximized at the optimum speed of 2 rotations per hour (Mak et al., 1990). The pigment productivity (pigment per gram of dry cell mass) using a roller bottle was nearly fourfold higher than that using stationary bottle, and the pigment yield (per gram of glucose or total absorbance units produced per gram of glucose consumed) was about tenfold higher than that obtained from batch submerged and agar surface cultures. As cells attached on the wall rotated with the rotating wall, the mycelium regularly exposed to air or medium as the bioreactor was not fully filled, which led to retarded conidiation and thus raising the productivity of *Monascus* pigments.

It was found that cells with three dimensional patterns were difficult to cultivate *in vitro*. Schwarz used a rotating-wall vessel (RWV) to successfully grow BHK-21 cells to high density (1.1×10^7 cells per ml in batch mode (Schwarz et al., 1992). Various publications have investigated the damage from turbulence or shear stress to cells. The environment of spaceflight possessed this feature of suspending micro carrier beads without turbulence, but operating experiments free of gravitational forces were not common. The RWV also simulated a similar environment for cells. Furthermore, Schwarz used a novel way of oxygenation, i. e. silicon membrane oxygenation, which Fleischaker and Sinsky (1981) applied before. The membrane was wrapped around the center shaft of the vessel, where oxygen diffused through the membrane into the system without introducing any bubbles. This operating environment of a RWV for

BHK-21 cells was proved to be quiescent, low-shear and low-turbulence. The gentle mixing process was contributed to the motion of the micro carriers caused by the rotation of the vessel. Scanning electron micrographs also showed three-dimensional aggregates of cells on dozens of micro carriers. The RWV has a high possibility in cultivating the wide variety of cell types and neoplastic tissues due to the similarity between rotating environment in RWV and zero gravity conditions in spaceflight.

Oh et al. (1994) developed a depth filter perfusion system (DFPS) which had a volume of about 300 or 400 mL for hybridoma cells. The surface area to volume ratio can reach 450 to 600 cm^2 per cm^3. The circulated radial flowing medium (about 10 to 20 mL per min at first, then nearly 30 mL per min) would increase medium usage efficiency, provide enough oxygen to cells (the oxygen uptake rate of this cell line was about 5 µg per 10^6 cells per hour), and lead to stable high percentage entrapment of cells (more than 90 percent of the cells) in the pore space. Twenty µm and 30 µm filters were used for comparison. The experimental data indicated that the smaller pore size filter (with a limitation of cell size about 13 µm to prevent the filter from clogging) could have higher entrapment efficiency than that in the larger (Oh et al., 1994). Within 10 days, the density of hybridoma cells was about 3×10^7 cells per mL using their system with the 20 µm filter. The productivity of monoclonal antibodies was 744 mg per liter per day, 25 to 35 times higher than that from the continuous suspension culture. Also, the well-distributed particles on the depth filters and low possibility of filter clogging made the long-term operation possible.

Dronawat et al. (1997) analyzed the effect of different geometry of impellers on gas-liquid mass transfer coefficients. Three combinations of impellers were used: two Rushton turbines, the Rushton and hydrofoil combination, and the Rushton and propeller combination.

Cellulose fibers were used to simulate the rheological behavior of *Aspergillus niger* (Dronawat et al., 1997). The mass transfer coefficients were obtained through measuring electrode dynamics at different gassing rates, agitation speeds and cellulose fiber concentrations. Mass transfer coefficients were found to decrease with increasing concentration of cellulose fibers as expected. Also, increasing agitation rate would help increase mass transfer coefficients. The conclusions were that two Rushton turbines gave the best performance at the low agitation rate, while the Rushton and hydrofoil combination standout among the other two for the case of high agitation rate. Moreover, the Rushton and propeller combination consumed the least power. Tests were conducted both in a 20 L stirred-tank fermenter and in 65 L tank, which would help to state the scale-up effect.

Airlift bioreactors with multistage columns have been used in many bioengineering experiments and processes. The hydrostatic pressure inside the gas-lift bioreactor enables the system to circulate the fluids. Unlike stirred tank, energy dissipation and shear are more dispersed in airlift bioreactors, thus the cultured cells may therefore not encounter contrasting environments (Merchuk, 1990). The excellent performance of a gas-lift bioreactor has already been widely investigated. As was concluded by Chisti (1998), the lower shear environment, higher oxygen transfer, lower power inputs, lower possibility of failure, and the lower cost were the most competitive advantages of airlift columns compared to stirred tanks and aerated bioreactors. Mass transfer could also be affected by the viscosity of fluids. Density difference was regarded as the main force for the motion between gas and liquid phase (Bendjaballah et al., 1999; Calderbank and Moo-Young, 1995; Choi and Lee, 2007; Kawase et al., 1994; Young et al., 1991). Normally, the volumetric mass transfer coefficient ($k_L a$) is treated as one of the standards for oxygen transfer performance. Kilonzo and Margaritis' study have indicated that

k_L would decrease rapidly as viscosity increased. In addition, since the bubble size increases as viscosity increases, interfacial area would decrease due to the rapidly rising of large bubbles (Kilonzo and Margaritis, 2004). In the other words, the volumetric mass transfer coefficient $k_L a$ would decrease rapidly as viscosity increases (Suh et al., 1992; Zhao et al., 1994). The time required for small bubbles to reach equilibrium in viscous fluids was found to be much shorter than that for large bubbles, due to the larger interfacial area per unit of gas volume that small bubbles have. Most of the small bubbles with the properties of very small rise velocities are circulated to the down flow section, which affect the molar gas flow rate and thus the oxygen mass transfer.

Berson et al. (2002) introduced a modified continuous roller bottle (length, 61 cm; diameter, 9.1 cm; full capacity, 4 L) with more comprehensive work than his previous publication (Berson et al., 1998). His reactor enhanced mixing and mass transfer by adding a recirculation loop, wall baffles, and center baffles. The surface area to volume ratio was 0.206 cm^2 per cm^3. The cell densities for four different mammalian cell lines (human carcinoma HeLa, hamster ovary CHO, myeloma NS/1, myeloma SP2/0) cultivated using his enhanced bioreactor were shown to be 2.13 to 2.95 times greater than the densities supported by the original design (Berson et al., 2002). In the newer design, cells maintained high viabilities up to 25 days, which could be a consequence of continuous medium feeding. Mathematical models were developed to calculate the axial liquid flow and oxygen transfer for the bioreactor chamber and the sample loop, respectively. Berson concluded that increased rotational velocity and baffle number contributed to the increase of axial dispersion coefficient in the newer design. The oxygen transfer rate obtained from the recirculation loop was shown to have 381 to 723 percent higher than that from the unbaffled growth chamber, which was attributed to the more rigorous interface

contact in the recirculation loop. The increased oxygen transfer using the newer reactor indicated high potential in further scale-up as the reactor allowed more liquid to be operated.

Burris and his group (2002) predicted oxygen transfer and water flow rate in airlift aerators. The aerator used in the experiment was large (with a capacity of approximate 49 x 10^6 m^3) and was installed by a local municipal water system in its reservoirs (Burris et al., 2002). Data were collected over various air flow rates to generate water flow rates, gas-phase holdup, and dissolved oxygen (DO) profiles. A discrete-bubble model was applied and proved to be in close agreement with the DO profiles and the observed gas-holdup both in the riser and downcomer. The Sauter-mean diameter (use diameter of a sphere that has same volume/surface area ratio) of the bubbles, which ranged from 2.7 to 3.9 mm, was measured in lab scale using a large cylindrical tank. The predicted bubble size was 2.3 to 3.1 mm. The variation in bubble size could be due to the difference in hydrodynamic conditions between the field and the laboratory tests. Additionally, at intermediate water velocity (around 0.9 m s^{-1}), the calculated frictional loss coefficient for the air-water separator (Kt) was was close to the 5.5 predicted from literature based on similar external airlift aerators. This agreement suggested the water flow rate in the airlift bioreactor could be obtained by using an energy-balance approach.

Chisti and Jauregui-Haza (2002) developed a mechanically agitated airlift bioreactor which combined the feature of airlift bioreactors and conventional stirred fermenters. The reactor could achieve more fluid circulation than airlift reactors and reduce the possibility of impeller flooding as in stirred fermenters through aerating the gas in the annular riser zone (Chisti and Jauregui-Haza, 2002). Several properties were characterized in this relatively large reactor (approximately 1.5 m^3, with diameter of 0.755 m and height of 3.21 m). While keeping aeration velocity and agitation rate as constant, the experimental figures showed that the gas hold

up declined with increasing concentration of the cellulose fiber solids, which led to the decrease of gas-liquid interfacial area, and thus the decline of overall volumetric mass transfer coefficient ($k_L a_L$) measured with dynamic method. On the other hand, mixing time was independent of the slurry with a concentration of 0 to 4 percent. Though the mixing performance and the oxygen transfer were enhanced by the agitation, the oxygen transfer efficiency was reduced when using agitation due to the increased power demand for mechanical agitation. Surface aeration in this case contributed less than 12 percent to the total oxygen transfer, but may contribute more in shallow reactors for animal cell culture.

Hristov et al. (2004) described the performance of a new geometry Narcissus (NS) impeller by using a three-dimensional model with large quantity of networks-of-zones (36,000 zones). The NS impellers were used to improve the performance of gas-liquid mixing, mass transfer and bioreaction in the system (Hristov et al., 2004). The new zones in the model were modified by readapting the zone volume from the existing computer algorithm for a Rushton turbine which kept the original conservation and balance equations unchanged. The new design of this NS impeller helped created the complex upwards and downwards flows which contributed to the improvement of the locally dissolved oxygen. However, whether this higher level of locally dissolved oxygen led to higher observed biomass production rates still remained uncertain. Gas hold-up, bubble phase oxygen, liquid-phase dissolved oxygen, nitrate nutrient and bioreaction rates were computerized in CFD modeling to visualize the complex fluid patterns in this triple impeller bioreactor. Also, the power consumption was reduced by 30% by using a Narcissus (NS) impeller instead of a conventional Rushton turbine.

2.5. Scale-Up for Bioreactors

Bioreactor processes usually can be divided into four scales of operation: flask level (low working capacity and low cost), laboratory level (preliminary procedures), pilot level (optimal operating conditions) and production level (large scale and financial return) (Lonsane et al., 1992). The scale-up process is commonly referred to the process of reproducing the successful results from the laboratory or bench scale equipment to production scale equipment. To achieve effective scale up, some characteristics can be maintained constant, such as reactor geometry, maximum shear, power input per unit volume of liquid, mixing time and volumetric oxygen transfer coefficient (k_La) (in the aerated system) (Ju and Chase, 1992). The conventional strategies for scale-up are normally based on controlling the impeller speed (N), volumetric gas flow rate (Q) and ratio of impeller diameter to the bioreactor diameter (D_i/D_B). The volumetric oxygen transfer coefficient could also be introduced into the system to represent one of the previous parameters. Ju and Chase (1992) proposed an improved method to replace the volumetric oxygen transfer coefficient by the oxygen transfer rate (or gas-phase oxygen partial pressure via Henry's law) in the aerated system, which still involved of parameter power input per unit liquid volume.

The filter system has already been used to grow much higher cell densities since 1969 when Himmelfarb et al. (1969) increased the density of mouse leukemia L1210 to 10^8 cells per milliliter using a spin filter device to replace (previous methods). Tolbert et al. (1981) developed a rotating filter perfusion system which cultivated high density mammalian cells. A four-liter vessel was first built. Subsequently, a second vessel was scaled up to 40 liters. Agitation was accomplished by rotating the filter (1 μm) which was magnetically driven. Fresh media were fed to the system at a rate of 10 to 20 ml per hour per 10^9 cells, while the waste was withdrawn *via*

the filter. Hence, liquid level was approximately constant (Tolbert et al., 1981). pH was controlled by CO_2 and $NaHCO_3$ (0.5 M) to the system automatically to maintain high pH environment for the walker 256 rat tumor cell line. A mixture of carbon dioxide (5 to 10 percent) and air was provided, as well as pure oxygen at a small flow rate. The maximum concentration could reach nearly 4×10^7 cells per mL for a four-liter vessel, while maintaining the viabilities above 95 percent. On the other hand, for a 40-liter vessel, cell suspension was harvested daily after a cell density of 9×10^6 cells per mL was cultivated and maintained. The total yield of 8.7×10^{11} cells was obtained from this system using 360 liters of medium. The conclusions indicated that cells concentration in this system was ten- to thirty-fold higher than the traditional Bellco spinners, and the medium usage efficiency was two- to three-fold greater than non-perfused systems.

Applegate (1992) compared the performance of a single-pass ceramic matrix bioreactor and an immobilized recycle bioreactor. The single-pass ceramic matrix bioreactor was showed to have higher product yields (80 percent higher of antibody concentration within a residence time of 200 minutes which was much less than the recycle one), simpler operation modes, and better axenic conditions. Hydrodynamic and interfacial forces caused by a conventional oxygen supply method could be damaging to cells. Also, recycled medium may impact cell viability and cell protein production adversely due to modest oxygenation. This single-pass bioreactor used a unique oxygenation method which allowed the oxygen to be supplied along the entire reactor. Gaseous oxygen passed through the silicone tube, across the open channel, and then was consumed by entrapped cells in the porous wall. Shear forces were minimized since the cells were entrapped into the porous wall. Plug flow operation in this single-pass bioreactor gave many other advantages over conventional bioreactors, such as high protein production and cell

viability at the beginning of the reactor (Applegate and Stephanopoulos, 1992). The scale-up criteria for this single-pass bioreactor was straightforward due to its proper design and based on maintaining a minimum dissolved oxygen concentration, which satisfies cell growth and occurs at the midsection of the porous wall according to the concentric cylinder approximation for oxygen concentration distribution. Either the oxygen concentration in the inlet gas flow or the total amount of the gas flow could be increased to increase the maximum bioreactor length. Moreover, ceramic monoliths, which was used in this bioreactor to retain cells, were considered to have better performance in controlling the maximum diffusional lengths and oxygen demand in volumetric base among other materials.

In the suspension animal culture, stirred bioreactors are one of the most competitive designs. Chisti (1993) scaled up a stirred bioreactor from 0.02 to 0.3 m^3, while maintaining a high concentration for hybridoma cells. A series of three bioreactors (0.02, 0.075 and 0.3 m^3) were established. The appropriate aeration was controlled by the four-hole sparger which was half way between the propeller and the bottom of the tank, because, though the porous-metal sparger gave a higher mass transfer coefficient, it generated small bubbles which formed highly densely packed foam (Chisti, 1993). The experimental results revealed that a cell density of nearly 2 x 10^{12} cells per m^3 and high viability (about 75 percent) were obtained after 45 to 50 hours at a constant impeller speed of 1.67 m s^{-1} in a 0.3 m^3 bioreactor. Mechanical impeller operation and foam control seemed to have negligible effects on cells. Hybridoma cells were shown to have a larger ability to withstand shear stress than expected. High impeller tip speed (>1m s^{-1}), Reynolds numbers (>10^5), and the size of energy-dissipating terminal eddies (>10 fold that of the hybridoma cells) did not cause significant damage to cells in this bioreactor up to 0.3 m^3.

Bioreactors with a rotating filter (or called spin-filter based bioreactor) are commonly applied in continuous perfusion system. Yabannavar et al. (1994) successfully scaled up a spin-filter perfusion bioreactor for mammalian cell retention from 12 L (with high cell densities up to 10^7 mL^{-1}) to 175 L both in working volume. Filter screens with 25 μm pore size was chosen to avoid the clogging. The rotational speed of the filter was proved to have large effect on cell retention and screen clog; high speed led to cell rupture and low speed caused screen clog. In the other words, the ratio of permeation drag (which is related to the fluid exchange across the screen) to lift drag should be kept below a certain value to avoid the screen clog. The spin-filter speed was 28 RPM for a 170 L working volume bioreactor or ABEC bioreactor, while the original was 50 RPM for 12 working volume bioreactor or MBR bioreactor. The experimental data for fluid exchange (exchange flow per working volume) was notably similar between two different sizes of reactors when the working conditions were set to be equivalent. Cell counts were similar, also. The similarity of cell retention results confirmed the equivalent performance of the two bioreactors with different size.

In Tolbert's work, as described before, he actually experienced screen fouling after two weeks. Deo et al. (1996) studied a series of parameters (spin-filter rotation speed, perfusion rate, cell density) that can cause screen fouling and finally scaled up the model from 7 L to 500 L successfully. The screen fouling phenomenon was examined by using scanning electron microscopy. They concluded that a raise in the spin-filer area per reactor volume would lead to a proportional increase in perfusion capacity without screen fouling under the condition of fixed rotational velocity and cell concentration (or $\frac{Reactor\ Volumes}{Day} \propto \frac{A}{V}\frac{v_\theta^2}{C}$) (Deo et al., 1996). Hence, the design for a scale-up bioreactor was established based on that conclusion. It was desirable to increase the ratio of the spin-filter diameter to height in order to increase perfusion capacity

which led to the better performance in long term use for large scale reactor according to the proposed equation. Also, the perfusion capacity, which could be increased by raising rotational spin-filter velocity, contributed to the cell concentration. As shown in their research, about 1.0 kg of antibodies (with concentration of 75 mg per liter) could be produced in one 500-liter reactor within one month, which would require 5000 – 10000 L bioreactor if using batch or fed-batch systems.

Shukla et al. (2001) used the volumetric mass transfer coefficient (k_La) as a standard to scale up the biotransformation process (yeast isolate VS1 used to biotransform benzaldehyde to L-phenyl acetyl carbinol or L-PAC) in a shaking flask (100 ml) to a stirred tank (5 L) which used dual impeller. The fractional hold-up and k_La were measured to be highest in the air-water system, followed by growth medium, and then biotransformation medium. Also, corresponding correlations for gas hold-up and k_La were developed under the conditions of different medium, and were consistent with other literatures except for the case of biotransformation medium. The correlations were used to optimize the impeller speed and air flow rates. Moreover, more cell mass (78% more) and higher yield of L-PAC (desired product) were obtained in the bioreactor than the shaking flask for 2 hours of reaction, which may be due to better mixing performance in the bioreactor than that in the shaking flask.

Xing et al. (2009) scaled up a bioreactor with multiple marine impellers for CHO cell culture process to 5,000 L from the bench scale 5- and 20-L bioreactor, using parameters of oxygen transfer coefficient, mixing time and carbon dioxide removal rate. This large bioreactor was observed to have the maximum viable CHO cell capacity of 7×10^6 cells mL^{-1}. Empirical equations showed that in comparison to the bench scale reactor, the 5,000 L bioreactor had a lower oxygen transfer coefficient (which could be improved by increasing bottom air sparging

instead of increasing power input), longer mixing time (the potential significant existence of pH and DO gradients in large scale may lead to serious implications for the cell cultivation), and lower carbon dioxide removal rate (a result due to higher pCO_2 level in cell culture). However, more efforts were needed to optimize the bulk mixing and carbon dioxide removal, since the liquid volume increased dramatically in the bioreactor with fed-batch mode.

2.6. Calculations for Reynolds Number

In fluid systems, the Reynolds number (Re) is widely calculated to help identify the flow patterns in different situations. The idea was first proposed by George Gabriel Stokes for introducing similar properties to his basic equations of viscous flow in 1850 (Stokes, 1850). The Reynolds number was named after Osborne Reynolds who set forth the law in 1883 (Reynolds, 1883; Rott, 1990). The definition of the Reynolds number is the ratio of inertial forces to viscous forces, defining laminar or turbulent flow. Laminar flow occurs when the Reynolds number is small, or viscous forces are the primary forces in the system, thus generating parallel-layer flow. Similarly, a high Reynolds number where the inertial forces dominate will result in turbulent flow.

The general Reynolds numbers is as follows:

$$Re = \frac{inertial\ forces}{viscous\ forces} = \frac{\rho u \frac{du}{dx}}{\mu \frac{d^2u}{dx^2}} = \frac{\rho uu/L}{\mu u/L^2} = \frac{\rho uL}{\mu} = \frac{uL}{\upsilon} \qquad (2\text{-}13)$$

where ρ is the density of the fluids (kg m^{-3}); u is the velocity (m s^{-1}); L is the characteristic length (m); μ is the dynamic viscosity of the fluids (Pa-s or kg m^{-1} s^{-1}); υ is the kinematic viscosity of the fluids ($\upsilon = \frac{\mu}{\rho}$, m^2 s^{-1}).

For fluids between concentric cylinders with inner cylinder rotation with no axial pressure gradient, the expression for the Reynolds number can be (Bilgen and Boulos, 1973; Lathrop et al., 1992):

$$R_{e_{\phi m}} = \frac{\rho \Omega_i r_i (r_o - r_i)}{\mu} \qquad (2\text{-}14)$$

where $R_{e_{\phi m}}$ is the rotational Reynolds number based annulus gap; ρ is the density of the fluids (kg m^{-3}); Ω_i is the angular velocity of inner cylinder ($\Omega_i = \frac{2\pi * (rotational\ rate, RPM)}{60}$, radians per s); r_i is the radius of inner cylinder (m); r_o is the radius of outer cylinder (m); μ is the dynamic viscosity of the fluids (Pa-s or kg m^{-1} s^{-1}).

Similarly, if we rewrite the equation above for the Reynolds number in concentric cylinders with outer cylinder rotation with no axial pressure gradient, we obtain:

$$R_{e_{\phi m}} = \frac{\rho \Omega_o r_o (r_o - r_i)}{\mu} \qquad (2\text{-}15)$$

where Ω_o is the angular velocity of outer cylinder.

When the rotational Reynolds number is less than 64, the system flow is laminar; when the rotational Reynolds number is larger than 500, the system flow is turbulent; for the case of the Reynolds number between 64 and 500, the system flow is transient. Under certain conditions of two cylinders rotating in the same direction, the fluids could be either stable everywhere or unstable everywhere. In addition, when two cylinders rotate in opposite directions, the phenomenon will be observed that the region close to the inner cylinder tends to be unstable, while the region close to the outer cylinder is normally stable (Childs, 2012). Toroidal vortices were formed in these cases and could be explained by Taylor vortex flow theory (Taylor, 1923). Experiments also supported this existence of vortices. Kaye and Elgar (1958) revealed that four

modes of flow existed in an annulus with an inner rotating cylinder: laminar flow; laminar flow plus Taylor vortexes; turbulent flow; turbulent flow plus Taylor vortexes.

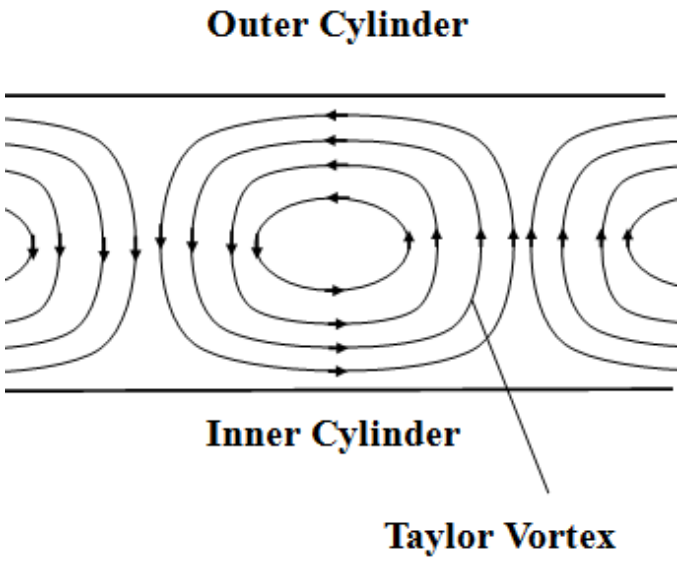

Figure 2.2. Taylor vortices cells (the inner cylinder had higher rotational speed than outer cylinder) (Childs, 2012)

When the case of the axial flow through the annulus exists, axial Reynold numbers will be also be calculated (Becker and Kaye, 1962; Chandrasekhar, 1959):

$$R_{e_z} = \frac{\rho u_z (r_o - r_i)}{\mu} \qquad (2\text{-}16)$$

where R_{e_z} is the axial Reynolds number; u_z is the velocity of the axial flow; r_i is the radius of inner cylinder (m); r_o is the radius of outer cylinder (m); μ is the dynamic viscosity of the fluids (Pa-s or kg m^{-1} s^{-}).

2.7. Computational Fluid Dynamics (CFD)

In recent years, computational fluid dynamic (CFD) tools are used widely to predict the fluid pattern and study the hydrodynamics of the bioreactors. Mudde (2001) used two- and three

dimensional (2D and 3D) simulations to predict the liquid circulation rate and gas fraction of an airlift reactor under steady state at low gas flow rates. The two-fluid flow with a modified k-ε turbulence model was used. The 2D (using developed code) and 3D simulations (using FLUENT 4.5) were found to be in good agreement with the mechanical energy balance (1D) (Mudde and Van Den Akker, 2001). The three-dimensional CFD results were considered to be more realistic than two-dimensional ones as a result of the deviations when compared to the LDA data.

Dhanasekharan (2005) proposed a generalized method to model oxygen transfer in airlift bioreactors. The standard k-ε model was used to simulate the turbulence (Dhanasekharan et al., 2005). The results (gas holdup and volumetric mass transfer coefficients) obtained from the three-dimensional CFD simulation (by using FLUENT 6) for two-phase flow (air and water) using a full multi-fluid Eulerian model were compared with the experimental data of Kawase and Hashimoto (1996). The overall predictions were in the same order and were in good agreement with experiment.

In Fayolle's work (2007), an experimentally validated numerical tool based on computational fluid dynamics (FLUENT 6.2) was used. The Euler-Euler model derived from the Navier-Stokes equations was selected to simulate the bubbly flow. The local axial velocity and gas hold-up were well reproduced by the CFD model both at the operating conditions of aeration and no aeration. The measurement error for mean axial liquid velocity was found to be around ten percent, and five percent for volumetric oxygen transfer coefficient (Fayolle et al., 2007). Simulation results were consistent with the fact that a larger bubble size will induce a smaller oxygen transfer coefficient.

Santhosh (2010) investigated the effect of rotational Reynolds number (Re_Ω) and axial Reynolds number (Re_a) on heat transfer and fluid flow in an annulus (radius ratio of 0.5) with an inner rotating cylinder and outer stationary wall. Two dimensional axial symmetric steady and incompressible flow (air) was simulated by CFD (FLUENT 6.3). The standard k-ε model was coupled with the incompressible Navier-Stokes equations. The effect of rotational Reynolds number on axial velocity occurred only when the axial Reynolds number was small, while the axial Reynolds number did not affect swirl velocity significantly (Sukumaran et al., 2010). The computational work was validated with experimental work.

Perez et al. (2013) simulated the turbulent flow of a rotating cylinder electrode with different geometry of counter electrodes (four-plate, six-plate and concentric cylinder). The Reynolds averaged Navier-Stokes (RANS) equation along with turbulent viscosity and the standard k-ε turbulence model was solved by using boundary conditions of universal logarithmic wall function (Pérez and Nava, 2013). The arrangement of four-plate and six-plate reactors was showed to develop turbulent Taylor vortex flow via 3-D simulations. Moreover, the hydrodynamics of the concentric situation was found to be superior to other two cases because of the quasi stagnant zones caused by plates near to plates and on the wall free of plates.

2.8. Cell Culture

Most cells (except for certain cells in blood) derived from tissues are anchorage-dependent, and so thereby require a surface upon which to grow. During attachment to the surface, cells divide and expand to cover the surface. The cell division stops when the entire surface is covered by the monolayer of cells or called contact inhibition. Then the detachment was conducted to degrade the protein that attaches cells to the surface by enzyme. The released

cells were transferred to the vessels for further cultivation or experimental purpose. For suspended cells, expansions are conducted by simply diluting cells with fresh medium step by step until reaching the require cell culture volume for experiments. Normally, the capacity of cell division could be 40-60 times of the original cell until the Hayflick limit is reached, after which cells become senescent (Hayflick, 1965; Shay and Wright, 2000).

Theoretical equation for the exponential growth in the batch could be described as:

$$\frac{1}{X}\frac{dX}{dt} = \mu \qquad (2\text{-}17)$$

where X is the biomass concentration (dry weight per unit volume, $g \cdot L^{-1}$) at time t (hr); μ is the specific growth rate (hr^{-1}). The exponential equation was only applied when the substrates are in excess state (Herbert et al., 1956).

In addition, if the feed media are sterile the changes of cell concentration in a continuous system (or a chemostat) could be described as follows (Herbert et al., 1956; Jannasch et al., 1969):

$$\frac{dX}{dt} = \mu X - DX \qquad (2\text{-}18)$$

where D is the dilution rate (hr^{-1}), and can be defined as:

$$D = \frac{F}{V} = \frac{1}{\tau} \qquad (2\text{-}19)$$

where F is the flow rate ($L \cdot hr^{-1}$); V is the liquid volume of reactor (L); τ is the mean residence time (hr).

When the specific growth rate is less than the dilution rate, the cells cannot maintain the concentration and will be washed out; if the growth rate is equal to dilution rate, the system reached steady state, i.e. cells maintains a constant concentration. Thus, through manipulating the dilution rate, the growth rate could be controlled.

References

Abu-Reesh I, Kargi F. 1989. Biological Responses of Hybridoma Cells to Defined Hydrodynamic Shear Stress. *J. Biotechnol.* **9**:167–178.

Amanullah A, Tuttiett B, Nienow AW. 1998. Agitator Speed and Dissolved Oxygen Effects in Xanthan Fermentations. *Biotechnol. Bioeng.* **57**:198–210.

Anderlei T, Büchs J. 2001. Device for Sterile Online Measurement of the Oxygen Transfer Rate in Shaking Flasks. *Biochem. Eng. J.* **7**:157–162.

Anderlei T, Zang W, Papaspyrou M, Büchs J. 2004. Online Respiration Activity Measurement (OTR, CTR, RQ) in Shake Flasks. *Biochem. Eng. J.* **17**:187–194.

Applegate M a, Stephanopoulos G. 1992. Development of a Single-Pass Ceramic Matrix Bioreactor for Large-Scale Mammalian Cell Culture. *Biotechnol. Bioeng.* **40**:1056–1068.

Bacon J, Demas J. 1987. Determination of Oxygen Concentrations by Luminescence Quenching of a Polymer-Immobilized Transition-Metal Complex. *Anal. Chem.* **2785**:2780–2785.

Bambot SB, Holavanahali R, Lakowicz JR, Carter GM, Rao G. 1994. Phase Fluorometric Sterilizable Optical Oxygen Sensor. *Biotechnol. Bioeng.* **43**:1139–1145.

Bandyopadhyay B, Humphrey AE, Taguchi H. 1967. Dynamic Measurement of the Volumetric Oxygen Transfer Coefficient in Fermentation Systems. *Biotechnol. Bioeng.* **9**:533–544.

Becker K, Kaye J. 1962. Measurements of Diabatic Flow in an Annulus with an Inner Rotating Cylinder. *J. Heat Transfer* **84**:97–104.

Belo I, Pinheiro R, Mota M. 2003. Fed-Batch Cultivation of Saccharomyces Cerevisiae in a Hyperbaric Bioreactor. *Biotechnol. Prog.* **19**:665–671.

Ben-Ze'ev A, Farmer SR, Penman S. 1980. Protein Synthesis Requires Cell-Surface Contact While Nuclear Events Respond to Cell Shape in Anchorage-Dependent Fibroblasts. *Cell* **21**:365–372.

Bendjaballah N, Dhaouadi H, Poncin S, Midoux N, Hornut J-M, Wild G. 1999. Hydrodynamics and Flow Regimes in External Loop Airlift Reactors. *Chem. Eng. Sci.* **54**:5211–5221.

Berson RE, Mane T V, Svihla CK, Hanley TR. 1998. Improved Oxygen Delivery in a Continuous-Roller-Bottle Reactor. *Appl. Biochem. Biotechnol.* **70–72**:615–627.

Berson RE, Pieczynski WJ, Svihla CK, Hanley TR. 2002. Enhanced Mixing and Mass Transfer in a Recirculation Loop Results in High Cell Densities in A Roller Bottle Reactor. *Biotechnol. Prog.* **18**:72–77.

Bibila T a, Robinson DK. 1995. In Pursuit of the Optimal Fed-Batch Process for Monoclonal Antibody Production. *Biotechnol. Prog.* **11**:1–13.

Bilgen E, Boulos R. 1973. Functional Dependence of Torque Coefficient of Coaxial Cylinders on Gap Width and Reynolds Numbers. *J. Fluid Engeering* **95**:122–126.

Burris VL, McGinnis DF, Little JC. 2002. Predicting Oxygen Transfer and Water Flow Rate in Airlift Aerators. *Water Res.* **36**:4605–4615.

Calderbank PH, Moo-Young MB. 1995. The Continuous Phase Heat and Mass Transfer Properties of Dispersions. *Chem. Eng. Sci.* **50**:3921–3934.

Chandrasekhar S. 1959. The Hydrodynamic Stability of Inviscid Flow between Coaxial Cylinders. *Proc. Natl. Acad. Sci.*:137–141.

Chattopadhyay D, Rathman JF, Chalmers JJ. 1995. The Protective Effect of Specific Medium Additives with Respect to Bubble Rupture. *Biotechnol. Bioeng.* **45**:473–480.

Cherry RS, Papoutsakis ET. 1986. Hydrodynamic Effects on Cells in Agitated Tissue Culture Reactors. *Bioprocess Eng.* **1**:29–41.

Cherry RS, Papoutsakis ET. 1989. Growth and Death Rates of Bovine Embryonic Kidney Cells in Turbulent Microcarrier Bioreactors. *Bioprocess Eng.* **4**:81–89.

Cherry RS, Papoutsakis ET. 1990. Understanding and Controlling Fluid-Mechanical Injury of Animal Cells in Bioreactors. *Anim. Cell Biotechnol.* **4**:71–121.

Cherry RS, Papoutsakis ET. 1988. Physical Mechanisms of Cell Damage in Microcarrier Cell Culture Bioreactors. *Biotechnol. Bioeng.* **32**:1001–1014.

Childs PRN. 2012. Rotating Cylinders, Annuli, and Spheres. In: . *Rotating Flow*. Elsevier Science, p. 416.

Chisti Y. 1993. Animal cell culture in stirred bioreactors: observations on scale-up. *Process Biochem.* **28**:511–517.

Chisti Y. 1998. Pneumatically Agitated Bioreactors in Industrial and Environmental Bioprocessing: Hydrodynamics, Hydraulics, and Transport Phenomena. *Appl. Mech. Rev.* **51**:33. http://appliedmechanicsreviews.asmedigitalcollection.asme.org/article.aspx?articleid=1396214.

Chisti Y. 2000. Animal-Cell Damage in Sparged Bioreactors. *Trends Biotechnol.* **18**:420–432.

Chisti Y. 2001. Hydrodynamic Damage to Animal Cells. *Crit. Rev. Biotechnol.* **21**:67–110.

Chisti Y, Jauregui-Haza UJ. 2002. Oxygen Transfer and Mixing in Mechanically Agitated Airlift Bioreactors. *Biochem. Eng. J.* **10**:143–153.

Choi KH, Lee WK. 2007. Circulation Liquid Velocity, Gas Holdup and Volumetric Oxygen

Transfer Coefficient in External-Loop Airlift Reactors. *J. Chem. Technol. Biotechnol.* **56**:51–58.

Croughan MS, Hamel J-F, Wang DIC. 1987. Hydrodynamic Effects on Animal Cells Grown in Microcarrier Cultures. *Biotechnol. Bioeng.* **29**:130–141.

Deo YM, Mahadevan MD, Fuchs R. 1996. Practical considerations in operation and scale-up of spin-filter based bioreactors for monoclonal antibody production. *Biotechnol. Prog.* **12**:57–64.

Dewey CF, Bussolari SR, Gimbrone M a, Davies PF. 1981. The Dynamic Response of Vascular Endothelial Cells to Fluid Shear Stress. *J. Biomech. Eng.* **103**:177–185.

Dhanasekharan KM, Sanyal J, Jain A, Haidari A. 2005. A Generalized Approach to Model Oxygen Transfer in Bioreactors Using Population Balances and Computational Fluid Dynamics. *Chem. Eng. Sci.* **60**:213–218.

Dronawat SN, Svihla CK, Hanley TR. 1997. Effect of Impeller Geometry on Gas-Liquid Mass Transfer Coefficients in Filamentous Suspensions. *Appl. Biochem. Biotechnol.* **63–65**:363–373.

Ducros E, Ferrari M, Pellegrino M, Raspanti C, Bogni C. 2009. Effect of Aeration and Agitation on the Protease Production by Staphylococcus Aureus Mutant RC128 in a Stirred Tank Bioreactor. *Bioprocess Biosyst. Eng.* **32**:143–148.

Duetz WA. 2007. Microtiter Plates as Mini-Bioreactors: Miniaturization of Fermentation Methods. *Trends Microbiol.* **15**:469–475.

Duetz WA, Witholt B. 2004. Oxygen Transfer by Orbital Shaking of Square Vessels and Deepwell Microtiter Plates of Various Dimensions. *Biochem. Eng. J.* **17**:181–185.

Ede CJC, Houten R Van, Beenacakers AACM. 1995. Enhance of Gas to Water Mass Transfer Rates by a Dispersed Organic Phase. *Chem. Enoineering Sci.* **50**:2911–2922.

Farmer SR, Ben-Ze'av A, Benecke BJ, Penman S. 1978. Altered Translatability of Messenger RNA from Suspended Anchorage-Dependent Fibroblasts: Reversal Upon Cell Attachment to A Surface. *Cell* **15**:627–637.

Fayolle Y, Cockx A, Gillot S, Roustan M, Héduit A. 2007. Oxygen Transfer Prediction in Aeration Tanks Using CFD. *Chem. Eng. Sci.* **62**:7163–7171.

Fleischaker RJ, Sinskey A. 1981. Oxygen Demand and Supply in Cell Culture. *Eur. J. Appl. Microbiol. Biotechnol.* **12**:193–197.

Folkman J, Moscona A. 1978. Role of Cell Shape in Growth Control. *Nature* **273**:345–349.

Fraden J. 1996. Handbook of Modern Sensors: Physics, Designs, and Applications Third. New York: Springer-Verlag.

Garcia-Ochoa F, Gomez E. 2009. Bioreactor scale-up and oxygen transfer rate in microbial processes: An overview. *Biotechnol. Adv.* **27**:153–176.

Gayik S. 2001. The Studies on the Oxygen Mass Rransfer Coefficient in a Bioreactor. *Process Biochem.* **36**:729–741.

Goldblum S, Bae YK, Hink WF, Chalmers J. Protective Effect of Methylcellulose and Other Polymers on Insect Cells Subjected to Laminar Shear Stress. *Biotechnol. Prog.* **6**:383–390.

Handa-Corrigan a., Emery AN, Spier RE. 1989. Effect of Gas-Liquid Interfaces on the Growth of Suspended Mammalian Cells: Mechanisms of Cell Damage by Bubbles. *Enzyme Microb. Technol.* **11**:230–235.

Handa A, Emery AN, Spier RE. 1987. On the Evaluation of Gas-Liquid Interfacial Effects on

Hybridoma Viability in Bubble Column Bioreactors. *Dev. Biol. Stand.* **66**:241–253.

Harris I, Roper G. 1964. The Absorption of Oxygen by Sodium Sulphite on a Sieve Plate. *Can. J. Chem. Eng.* **42**:34–37.

Hayflick L. 1965. The Limited in Vitro Lifetime of Human Diploid Cell Strains. *Exp. Cell Res.* **37**:614–636.

Henry W. 1803. Experiments on the quantity of gases absorbed by water, at different temperatures, and under different pressures. *Philos. Trans. R. Soc. Londonosophical Trans.* **93**:29–274.

Herbert D, Elsworth R, Telling RC. 1956. The continuous culture of bacteria; a theoretical and experimental study. *J. Gen. Microbiol.* **14**:601–622.

Hermann R, Walther N. 2001. Optical Method for the Determination of the Oxygen-Transfer Capacity of Small Bioreactors Based on Sulfite Oxidation. *Biotechnol. Bioeng.* **74**:354–363.

Himmelfarb P, Thayer PS, Martin HE. 1969. Spin Filter Culture: the Propagation of Mammalian Cells in Suspension. *Science (80-.).* **164**:555–557.

Hristov H V, Mann R, Lossev V, Vlaev SD. 2004. A Simplified CFD for Three-Dimensional Analysis of Fluid Mixing, Mass transfer and Bioreaction in a Fermenter Qquipped with Triple Novel Geometry Impellers. *Food Bioprod. Process.* **82**:21–34.

Jannasch HW, Sp. P, Marinorubra S. 1969. Estimations of bacterial growth rates in natural waters. *J. Bacteriol. 1 ; 156-160* **99**:156–160.

Jeude M, Dittrich B. 2006. Fed-Batch Mode in Shake Flasks by Slow-Release Technique. *Biotechnol. Bioeng.* **95**:433–445.

John GT, Klimant I, Wittmann C, Heinzle E. 2003. Integrated Optical Sensing of Dissolved

Oxygen in Microtiter Plates: a Novel Tool for Microbial Cultivation. *Biotechnol. Bioeng.* **81**:829–836.

Jordan M, Eppenberger HM, Sucker H, Widmer F, Einsele A. 1994. Interactions Between Animal Cells and Gas Bubbles: the Influence of Serum and Pluronic F68 on the Physical Properties of the Bubble surface. *Biotechnol. Bioeng.* **43**:446–454.

Ju LK, Chase GG. 1992. Improved scale-up strategies of bioreactors. *Bioprocess Eng.* **8**:49–53.

Kawase Y, Hashimoto N. 1996. Gas Hold-Up and Oxygen Transfer in Three-Phase External-Loop Airlift Bioreactors: Non-Newtonian Fermentation Broths. *J. Chem. Technol. Biotechnol.* **65**:325–334.

Kawase Y, Omori N, Tsujimura M. 1994. Liquid-Phase Mixing in External-Loop Airlift Bioreactors. *J. Chem. Technol. Biotechnol.* **61**:49–55.

Kaye J, Elgar EC. 1958. Modes of adiabatic and diabatic fluid flow in an annulus with an inner rotating cylinder. *Trans. ASME* **80**:753–765.

Kilian SG, Prior BA, Pretorius IS, Preez JC du, Venter JJ, Hans J. Potgieter. 1983. Nutritional, Temperature, pH, and Oxygen Requirements of Candida Wickerhamii. *Eur. J.* … **17**:334–338.

Kilonzo PM, Margaritis A. 2004. The effects of non-Newtonian fermentation broth viscosity and small bubble segregation on oxygen mass transfer in gas-lift bioreactors: a critical review. *Biochem. Eng. J.* **17**:27–40.

Klimant I, Wolfbeis OS. 1995. Oxygen-Sensitive Luminescent Materials Based on Silicone-Soluble Ruthenium Diimine Complexes. *Anal. Chem.* **67**:3160–3166.

Komasawa I, Kuboi R, Otake T. 1974. Fluid and Particle Motion in Turbulent Dispersion—I.

Chem. Eng. Sci. **29**:641–650.

Kunas KT, Papoutsakis ET. 1990. Damage Mechanisms of Suspended Animal Cells in Agitated Bioreactors with and without Bubble Entrainment. *Biotechnol. Bioeng.* **36**:476–483.

Lathrop DP, Fineberg J, Swinney HL. 1992. Turbulent Flow between Concentric Rotating Cylinders at Large Reynolds Number. *Phys. Rev. Lett.* **68**:1515–1519.

Linek V, Vacek V. 1981. Chemical Engineering Use of Catalyzed Sulfite Oxidation Kinetics for the Determination of Mass Transfer Characteristics of Gas-Liquid Contactors. *Chem. Eng. Sci.* **36**:1747–1768.

Lonsane BK, Saucedo-Castaneda G, Raimbault M, Roussos S, Viniegra-Gonzalez G, Ghildyal NP, Ramakrishna M, Krishnaiah MM. 1992. Scale-up strategies for solid state fermentation systems. *Process Biochem.* **27**:259–273.

Losen M, Frölich B, Pohl M, Büchs J. 2004. Effect of Oxygen Limitation and Medium Composition on Escherichia coli Fermentation in Shake-Flask Cultures. *Biotechnol. Prog.* **20**:1062–1068.

Maier U, Losen M, Büchs J. 2001. Characterisation of the Gas-Liquid Mass Transfer in Shaking Bioreactors. *Biochem. Eng. J.* **7**:99–106.

Maier U, Losen M, Büchs J. 2004. Advances in Understanding and Modeling the Gas–Liquid Mass Transfer in Shake Flasks. *Biochem. Eng. J.* **17**:155–167.

Mak NK, Fong WF, Wong-Leung YL. 1990. Improved Fermentative Production of Monascus Pigments in Roller Bottle Culture. *Enzyme Microb. Technol.* **12**:965–968.

Martin I, Wendt D, Heberer M. 2004. The Role of Bioreactors in Tissue Engineering. *Trends Biotechnol.* **22**:80–86.

Merchuk JC. 1990. Why use air-lift bioreactors? *Trends Biotechnol.* **8**:66–71.

Mudde RF, Van Den Akker HE a. 2001. 2D and 3D Simulations of an Internal Airlift Loop Reactor on the Basis of a Two-Fluid Model. *Chem. Eng. Sci.* **56**:6351–6358.

Murhammer DW, Goochee CF. 1990. Structural Features of Nonionic Polyglycol Polymer Molecules Responsible for the Protective Effect in Sparged Animal Cell Bioreactors. *Biotechnol. Prog.* **6**:142–148.

Oh DJ, Choi SK, Chang HN. 1994. High-Density Continuous Cultures of Hybridoma Cells in a Depth Filter Perfusion System. *Biotechnol. Bioeng.* **44**:895–901.

Oh SK, Nienow a W, Al-Rubeai M, Emery a N. 1992. Further Studies of the Culture of Mouse Hybridomas in an Agitated Bioreactor with and without Continuous Sparging. *J. Biotechnol.* **22**:245–70.

Ortiz-Ochoa K, Doig SD, Ward JM, Baganz F. 2005. A Novel Method for the Measurement of Oxygen Mass Transfer Rates in Small-Scale Vessels. *Biochem. Eng. J.* **25**:63–68.

Papoutsakis ET. 1991. Fluid-mechanical damage of animal cells in bioreactors. *Trends Biotechnol.* **9**:427–437.

Payne G, Davison S, Tate J. 1990. Experimental Constraints to Studying the Effects of Dissolved Oxygen and Dissolved Carbon Dioxide on Plant Cell Growth. *Dev. Ind. Microbiol.* **31**:293–301.

Pérez T, Nava JL. 2013. Simulation of Turbulent Flow of a Rotating Cylinder Electrode. Influence of Using Plates and Concentric Cylinder as Counter Electrodes. *Int. J. Electrochem. Sci.* **8**:4690–4699.

Peter CP, Lotter S, Maier U, Büchs J. 2004. Impact of out-of-Phase Conditions on Screening

Results in Shaking Flask Experiments. *Biochem. Eng. J.* **17**:205–215.

Petersen JF, Mcintire L V., Papoutsakis ET. 1988. Shear Sensitivity of Cultured Hybridoma Cells (CRL-8018) Depends on Mode of Growth, Culture Age and Metabolite Concentration. *J. Biotechnol.* **7**:229–246.

Puthli MS, Rathod VK, Pandit AB. 2005. Gas–Liquid Mass Transfer Studies with Triple Impeller System on a Laboratory Scale Bioreactor. *Biochem. Eng. J.* **23**:25–30.

Ramírez OT, Mutharasan R. 1990. The Role of the Plasma Membrane Fluidity on the Shear Sensitivity of Hybridomas Grown under Hydrodynamic Stress. *Biotechnol. Bioeng.* **36**:911–920.

Reynolds O. 1883. An Experimental Investigation of the Circumstances Which Determine Whether the Motion of Water Shall Be Direct or Sinuous, and of the Law of Resistance in Parallel Channels. *Philos. Trans. R. Soc. London* **174**:935–982.

Rott N. 1990. Note On the History Of the Reynolds Number. *Annu. Rev. Fluid Mech.* **22**:1–11.

Ruchti G, Dunn IJ, Bourne JR, Stockar U Von. 1985. Practical Guidelines for the Determination of Oxygen Transfer Coefficients (K L a) with the Sulfite Oxidation Method. *Chem. Eng. J.* **30**:29–38.

Scheidle M, Klinger J, Büchs J. 2007. Combination of On-line pH and Oxygen Transfer Rate Measurement in Shake Flasks by Fiber Optical Technique and Respiration Activity MOnitoring System (RAMOS). *Sensors* **7**:3472–3480.

Schwarz RP, Goodwin TJ, Wolf D a. 1992. Cell Culture for Three-Dimensional Modeling in Rotating-Wall Vessels: an Application of Simulated Microgravity. *J. Tissue Cult. Methods* **14**:51–57.

Seletzky JM, Noack U, Hahn S, Knoll A, Amoabediny G, Büchs J. 2007. An Experimental Comparison of Respiration Measuring Techniques in Fermenters and Shake Flasks: Exhaust Gas Analyzer vs. RAMOS device vs. Respirometer. *J. Ind. Microbiol. Biotechnol.* **34**:123–130.

Shay JW, Wright WE. 2000. Hayflick, His Limit, and Cellular Ageing. *Nat. Rev. Mol. Cell Biol.* **1**:72–76.

Shukla VB, Parasu Veera U, Kulkarni PR, Pandit AB. 2001. Scale-up of biotransformation process in stirred tank reactor using dual impeller bioreactor. *Biochem. Eng. J.* **8**:19–29.

Stathopoulos N a, Hellums JD. 1985. Shear Stress Effects on Human Embryonic Kidney Cells in Vitro. *Biotechnol. Bioeng.* **27**:1021–1026.

Stockmann C, Losen M, Dahlems U, Knocke C, Gellissen G, Buchs J. 2003. Effect of Oxygen Supply on Passaging, Stabilising and Screening of Recombinant Production Strains in Test Tube Cultures. *FEMS Yeast Res.* **4**:195–205.

Stokes GG. 1850. On the Effect of the Internal Friction of Fluids on the Motion of Pendulums. *Trans. Cambridge Philos. Soc.* **9**:1–86.

Suh IS, Schumpe A, Deckwer WD. 1992. Xanthan Production in Bubble Column and Air-Lift Reactors. *Biotechnol. Bioeng.* **39**:85–94.

Suijdam JC VAN, Kossen NWF, Joha AC. 1978. Model for Oxygen Transfer in a Shake Flask. *Biotechnol. Bioeng.* **20**:1695–1709.

Sukumaran AK, Reji R V., Santhosh KS. 2010. Fluid Flow Simulations within Rotating Annulus. In: . *Proc. 37th Nat. 4th Conf. Fluid Mech. Fluid Power*.

Suresh S, Srivastava V, Mishra I. 2009. Techniques for Oxygen Transfer Measurement in

Bioreactors: a Review. *J. Chem. Technol. Biotechnol.* **84**:1091–1103.

Taylor GI. 1923. Stability of a Viscous Liquid Contained between Two Rotating Cylinders. *Philos. Trans. R. Soc. London* **223**:289–343.

Tolbert WR, Feder J, Kimes RC. 1981. Large-Scale Rotating Filter Perfusion System for High-Density Growth of Mammalian Suspension Cultures. *In Vitro* **17**:885–890.

Tramper J, Joustra D, Vlak J. 1987. Bioreactor Design for Growth of Shear Sensitive Insect Cells. *Plant Anim. Cell Cult. Process Possibilities*:125–136.

Tribe LA, Briens CL, Margaritis A. 1995. Determination of the Volumetric Mass Transfer Coefficient (kLa) using the Dynamic "Gas out–Gas in" Method: Analysis of Errors Caused by Dissolved Oxygen Probes. *Biotechnol. Bioeng.* **46**:388–392.

Vardar F, Lilly M. 1982. Effect of Cycling Dissolved Oxygen Concentrations on Product Formation in Penicillin Fermentations. *Eur. J. Appl. Microbiol. Biotechnol.* **14**:203–211.

Veglio F, Beolchini F, Ubaldini S. 1998. Empirical Models for Oxygen Mass Transfer: a Comparison between Shake Flask and Lab-Scale Fermentor and Application to Manganiferous Ore Bioleaching. *Process Biochem.* **33**:367–376.

Waal KJA De, Okeson JC. 1966. Studies of the Slurry Reactor. *Chem. Eng. Sci.* **21**:573–582.

Westerterp KR, Dierendonck LL Van, Kraa JA De. 1963. Interfacial Areas in Agitated Gas-Liquid Contactors. *Chem. Eng. Sci.* **18**:157–176.

Whitman WG. 1923. The two-film theory of gas absorption. *Chem. Metall. Eng.* **29**:146–148.

Wu J. 1995. Mechanisms of Animal Cell Damage Associated with Gas Bubbles and Cell Protection by Medium Additives. *J. Biotechnol.* **43**:81–94.

Wu J, Goosen MF a. 1995. Evaluation of the Killing Volume of Gas Bubbles in Sparged Animal Cell Culture Bioreactors. *Enzyme Microb. Technol.* **17**:241–247.

Wudtke M, Schiigerl K. 1987. Investigation of the Influence of Physical Environment on the Cultivation of Animal Cells. In: Spier, RE, Griffiths, JB, editors. *Modem Approaches to Anim. Cell Technol.*, pp. 297–315.

Xing Z, Kenty BM, Li ZJ, Lee SS. 2009. Scale-up analysis for a CHO cell culture process in large-scale bioreactors. *Biotechnol. Bioeng.* **103**:733–746.

Yabannavar VM, Singh V, Connelly N V. 1994. Scaleup of spinfilter perfusion bioreactor for mammalian cell retention. *Biotechnol. Bioeng.* **43**:159–164.

Yoshihito K, Hiraoka S, Tada Y, Sato K, Ohishi T. 1997. Measurment of Mass Transfer Rate from Free Surface in Shaking Vessel Type Bioreactor. *J. Chem. Eng. Japan* **30**:362–365.

Young M, Carbonell R, Ollis D. 1991. Airlift Bioreactors: Analysis of Local Two-Phase Hydrodynamics. *AIChE J.* **37**:403–428.

Zhang Z, Al-Rubeai M, Thomas CR. 1992. Effect of Pluronic F-68 on the Mechanical Properties of Mammalian Cells. *Enzyme Microb. Technol.* **14**:980–983.

Zhao M, Niranjan K, Davidson JF. 1994. Mass Transfer to Viscous Liquids in Bubble Columns and Air-Lift Reactors: Influence of Baffles. *Chem. Eng. Sci.* **49**:2359–2369.

Chapter 3 - Enhanced Oxygen Delivery to a Multiphase Continuous Bioreactor

Abstract

This research investigates a novel continuous bioreactor with significant improvement in gas-liquid transport phenomena. This bioreactor is an automated, horizontally-rotating bioreactor consisting of an outer cylindrical shell and a core with adjustable rotating velocities operated in continuous mode. The under-filled bioreactor provides a multiphase environment for the cell line beneficial for improving the gas-liquid transport phenomena. A spiroid tube is embedded in the inner surface of the outer wall of the bioreactor to increase gas-liquid contact area and thus improve oxygen transfer. Computational fluid dynamics simulations were performed to determine the optimum operating conditions for oxygen transfer. The oxygen transfer rates were determined experimentally, and the related volumetric mass transfer coefficients (k_La) were predicted by mathematical models at a variety of operating conditions. The results indicate that a reactor with an embedded spiroid reached saturation approximately two times faster than without the spiroid.

Keywords: Multiphase Computational Fluid Dynamics, Continuous Bioreactor, Oxygen Transport Phenomena, Roller Bottle, Spiroid

3.1. Introduction

Bioreactors have the potential to be applied in large-scale industrial processes to increase productivity. Bioreactors can be simply defined as devices that simulate or provide the most favorable conditions for specific cell lines. Various bioreactors (e. g. bubble columns, agitated reactors, roller bottles, membrane bioreactors) have been applied in the engineering and industrial production. Biological and biochemical experiments conducted in specific devices are controlled under a range of operating conditions in order to seek an optimal method to produce pharmaceuticals (e. g. antibodies, hormones, viral vaccines), solve environmental issues (e. g. wastewater treatment), process food, provide energy source (e. g. conversion of corns to alcohol) and supply cells and tissues lines (Martin et al., 2004).

In many biological cell cultivations, shear stress and oxygen transport of the bioreactor are normally considered to be two of the most limiting factors for the production results. Shear forces are known to have influences on cell shape and membrane structure, which in turn affect the physiology (e. g. metabolism of cells, protein synthesis, DNA and RNA mechanisms) (Abu-Reesh and Kargi, 1989; Ben-Ze'ev et al., 1980; Dewey et al., 1981; Farmer et al., 1978; Folkman and Moscona, 1978; Stathopoulos and Hellums, 1985). The sensitivity of cells to shear stress may vary with the stage of growth, the cultivation culture, and operation conditions (Petersen et al., 1988). To inhibit the activation of human cervical carcinoma HeLaS3 and mouse abdominal fibroblast L929 in the environment of turbulent flow through stainless steel capillaries, Augenstein et al. (1971) concluded that an average wall shear stress of (0.1-2.0) x 10^3 N m^{-2} should be achieved. Leukocytes could be sheared away from the vascular endothelium by shear stress at a range of 26.5 and 106 N m^{-2} in the rabbit omentum (Schmid-Schoenbein et al., 1975). McQueen et al. (1987) observed that a threshold average wall shear stress of 180 N m^{-2} would

lyse suspended mouse myeloma cells in the resulting turbulent capillary flow. The biochemical response of human T cells to the lectin phytohemagglutinin-P (PHA-P) would be affected when the shear stress was 10 to 20 N m^{-2} over 10 minutes (Chittur et al., 1988). For erythrocytes in tube flow (three mm tube and whole blood), hemolysis would occur in the entrance with the shear stress of 4000 N m^{-2} (Blackshear and Blackshear, 1987), which was in agreement with the conclusion from Bernstein et al. (1967) that the critical shear stress for the lysis of erythrocytes in turbulent jet was measured as 6000 N m^{-2} for brief exposures (around 10^{-5} s). For hybridoma cells sheared in a coaxial cylinder Searle viscometer, a shear stress level of over 5 Pa in the turbulent regime would damage cells over 0.75 hour exposure (Abu-Reesh and Kargi, 1989). A rapid decrease in cytosolic pH of rat aortic endothelial cells cultured in glass capillary tubes resulted from laminar shear stress (1.34 N m^{-2} of shear stress led to the maximal effect 0.09 pH unit) (Ziegelstein et al., 1992). The existence of shear stress cannot be avoided in most bioreactors. Generally, the damage of shear stress resulting from turbulent flow is more severe than that from laminar flow (Chisti, 2001). Thus, a bioreactor with low shear stress is desired in cell cultivation.

Oxygen transfer is one of the most important factors for aerobic bioprocesses. Aerobic bioprocesses normally take place in the aqueous phase where the oxygen solubility could be low due to ionic salts and nutrients (Suresh et al., 2009). However, the consumption rate of oxygen for cells is generally high. Hence, the growth of almost any microorganisms is limited to the amount of oxygen transferred. An increase of amount of dissolved oxygen will result in the increase of secondary metabolites of cells, while the limited oxygen will lead to the decrease of metabolic rate (Vardar and Lilly, 1982). Oxygen transfer rate may be influenced by various parameters including the physical properties of gas and liquid, operational conditions, choice of

bioreactor and presence of biomass (Garcia-Ochoa and Gomez, 2009). Many innovative methods have been used to improve the amount of dissolved oxygen, including the use of various bioreactors (e. g. stirred reactor, bubble column, shaking flasks (Maier et al., 2004, 2001), gas-lift bioreactors), using silicone membrane oxygenation to provide oxygen for large scale cell production (Fleischaker and Sinskey, 1981), adding an organic phase (often called oxygen vectors) to the system (Ede et al., 1995), adding a sample loop spiroid, wall baffles and center baffles to a continuous roller bottle reactor (Berson et al., 1998), introducing oxygen enriched air to the system, using hyperbaric air to aerate the bioreactor (Belo et al., 2003). The results from these modifications were promising, however, a simpler and more effective method to improve oxygen transfer was proposed in this study involving only adding a spiroid. This study demonstrated the ability of one novel rotating bioreactor with a spiroid to transfer oxygen to the liquid phase in the absence of living cells two times faster than did the same reactor without a spiroid. Were cells to be cultivated in this bioreactor, since the oxygen would be continuously consumed by the cells, the oxygen in the system would remain unsaturated; therefore, with the spiroid oxygen can be continuously aerated into the liquid phase increasing the efficiency of aeration.

Computational fluid dynamic (CFD) tools are used widely to predict the fluid pattern and study the hydrodynamics of the bioreactors. Cockx et al. (2001) applied the CFD code ASTRID in two-phase aeration reactors which predicted the dissolved gas concentration and optimized gas-liquid interfacial mass transfer process. Mudde and Van Den Akker (2001) used two- and three dimensional simulations to predict the liquid circulation rate and gas fraction of an airlift reactor under steady state at low gas flow rates by applying a modified k-ε turbulence model. Dhanasekharan et al. (2005) proposed a generalized method to model oxygen transfer in airlift

bioreactors with the standard turbulence k-ε model, which was in good agreement with the experimental data from Kawase and Hashimoto (1996). In Fayolle's work, an experimentally validated numerical tool based on computational fluid dynamics was used to precisely predict the aeration situation in different tanks (Fayolle et al., 2007).

This research investigated the use of an automated, horizontally-rotating bioreactor consisting of a rotating outer cylindrical shell and a counter-rotating core operated at various conditions. The inlet flow made the bioreactor a continuous system and provides additional medium with little effect to the system. The revolving cylinders with appropriate velocities (4 rpm, 6 rpm, 8 rpm) improve the mixing performance without causing cell damage due to the low shear stress. Furthermore, a spiroid tubing (8 turns) was attached to the wall of the outer cylinder to improve oxygen transfer. Experiments were conducted to compare the rates of oxygen transfer between the system with and without the spiroid.

3.2. Materials and Methods

3.2.1. Experimental Apparatus

Roller bottles are commonly used in cell cultivation. However, the operation of roller bottles is limited to batch operation. A continuous bioreactor is more attractive because the medium and oxygen can be added to the system continuously, thereby increasing the production of cells and cellular products.

Figure 3.1 illustrates the structure for this bioreactor with a spiroid. This bioreactor consists of an outer shell and an inner core, each with adjustable rotational velocities to provide a variable shear-rate environment and control the mixing performance in this reactor. The spiroid attached to the outer cylinder is designed to improve the oxygen transport through increasing the

gas-liquid contact areas. Spiroid ports are located at the reactor exit and entrance. Two motors allow independent rotation of the outer and inner cylinder of the bioreactor, either in concurrent or countercurrent rotation.

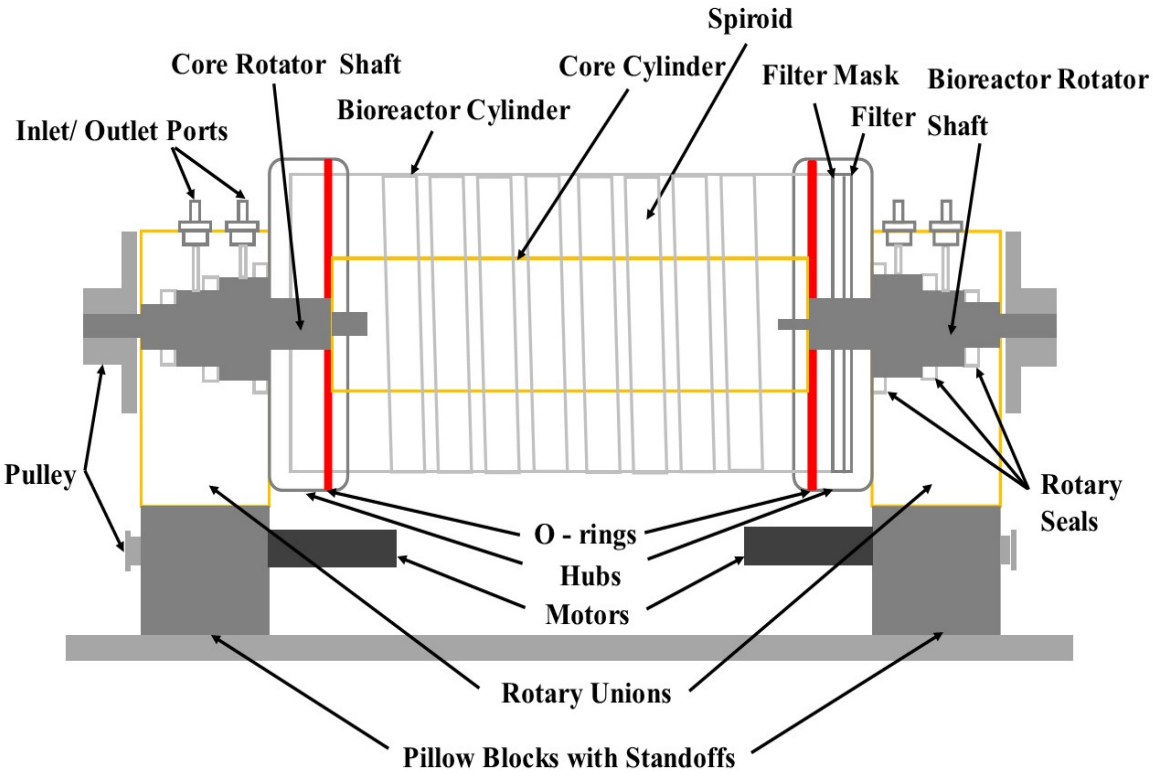

Figure 3.3. Bioreactor Design. For dimensions see Table 3.1

Table 3.1. Bioreactor Dimensions

Parameter	Value (m)
Core Length	0.0858
Core Shaft + Hub Part Length	0.00696
Shell Length	0.100
Shell Shaft Length	0.00782
Spiroid Tubing Length	1.09
Core Diameter	0.0254
Shafts' Diameter	0.0117
Shell Inner Diameter (I.D.)	0.0444
Spiroid Tubing Inner Diameter (I.D.)	0.00476

The specific dimensions of the bioreactor are found in Table 3.1. The original bioreactor has a volume of 1.109 x 10^{-4} m^3 and the surface area of 0.0252 m^2. The bioreactor with spiroid loop was prototyped using a 3D printer. To reduce loss of reactor volume, the spiroid was embedded in the inside wall of the shell. The bioreactor with the spiroid has a similar volume of 1.088 x 10^{-4} m^3 and a surface area of 0.0460 m^2, almost twice the original surface area). When the rotation starts, liquid is transported by the spiroid tube from the exit end to the entrance end of the bioreactor. Since the bioreactor is partially filled with liquid, the spiroid transports segments of liquid and gas, increasing the gas-liquid contact areas and oxygen mass transfer. This reactor can be operated in the batch mode, if necessary.

Figure 3.2 (a) and (b) shows the process flow diagram of the system before operation and in operation, respectively. The experimental work for measuring oxygen concentration and mass transfer coefficient were conducted using water. Nitrogen was bubbled through the water for two hours to eliminate any dissolved oxygen. In addition, oxygen was continuously aerated through the reactor for a long period of time to ensure the reactor was full of oxygen before conducting experiments. The pre-treated water was then pumped to the reactor in high flow rate (to reduce the oxygen and water contact time before the rotation) until 2/3 of the reactor was filled. Then, the tubing of the system was reconnected to be a closed system so that the fluids could flow through the oxygen probe. The optimal operating conditions were determined by using CFD simulations. The corresponsive oxygen concentration measurement was achieved by using a micro oxygen probe (Model DO-166FTL-XS, Lazar Research Laboratories, Los Angeles, CA, USA) to take data automatically and periodically. The collected data were plotted and analyzed to calculate the volumetric mass transfer coefficients through solving theoretical equations.

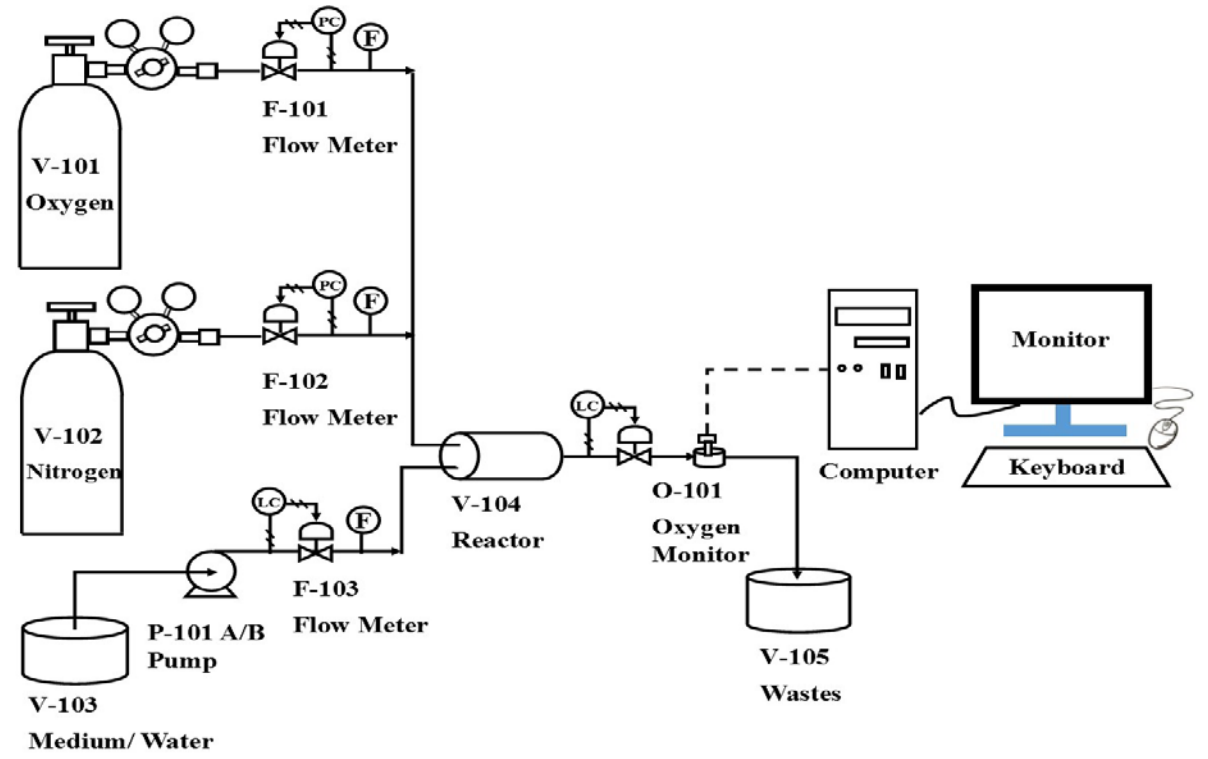

(a)

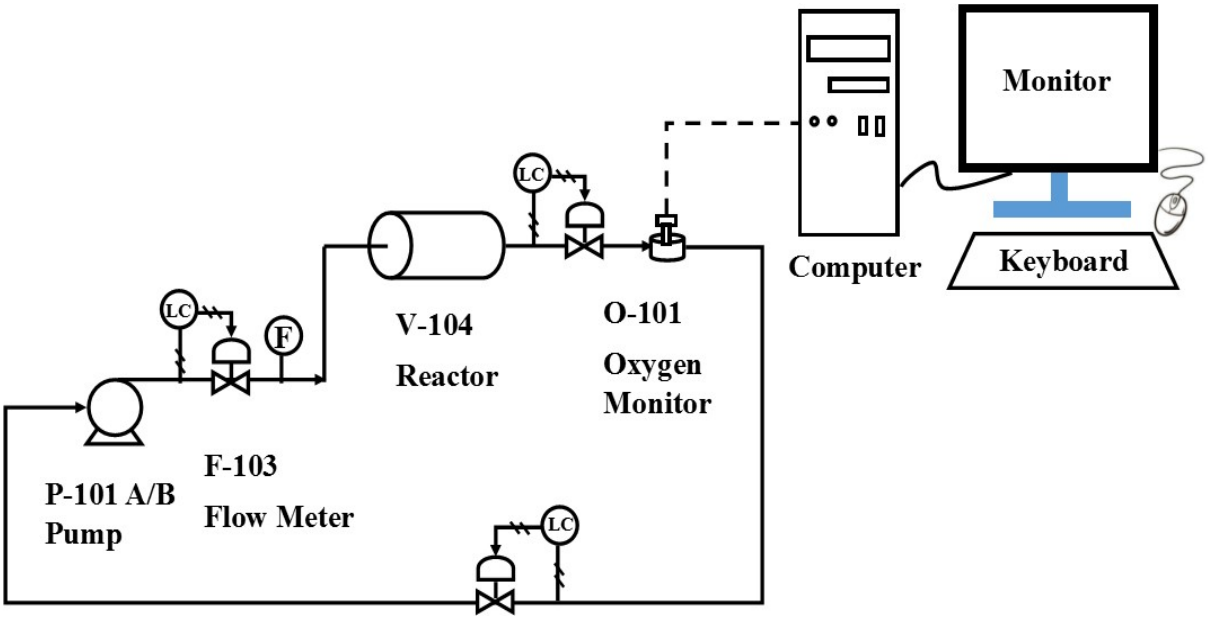

(b)

Figure 3.4. Process Flow Diagram. (a) Process Flow Diagram for the System before Operation; (b) Process Flow Diagram for the System in Operation

3.2.2. Preliminary Simulations for Experimental Operating Conditions

As mentioned, CFD simulations were used to analyze the possible behavior of the fluids and mixing performance in this novel bioreactor under the multiphase situation. Simulations were conducted to predict mixing performance under various operating conditions (4 rpm, 6 rpm and 8 rpm with concurrent and countercurrent rotations) that would occur in the experiments in order to find out the most optimized one. Results obtained from simulations were important auxiliary materials for further experiments. Moreover, the optimized operating conditions will be used in the future scaling-up.

ANSYS workbench version 16.0 (Ansys, Inc., Canonsburg, PA, US) was used in this research to carry out the simulations. Some appropriate assumptions should also be made in the computational dynamic fluid simulations, such as homogenous, Newtonian fluids, incompressible fluids, isothermal process and gravity existence. Two equation turbulence models (derived from Reynolds Averaged Navier-Stokes or RANS equations) are one of the most widely used and economic models to solve practical fluid engineering problems. In this study, the realizable k-ε turbulence model in combination with the Enhanced Wall Treatment (EWT) (which has the most consistent wall shear stress and is least sensible to y+ values) was applied in this research. k is the turbulence kinetic energy per unit mass (J kg^{-1} or m^2 s^{-2}), and ε is the dissipation rate per unit mass (J kg^{-1} s^{-1} or m^2 s^{-3}). The realizable k-ε model satisfies uniquely the realizable constraints on the normal Reynolds stresses and the unequal Schwartz shear stresses for the turbulent flow among any other k-epsilon turbulence models (Argyropoulos and Markatos, 2014).

For a two-phase (air and water, or dispersed and continuous phase) system, the equation of continuity for phase N (gas or liquid phase) with volume fraction of α_N could be written as follows:

$$\frac{\partial \alpha_N \rho_N}{\partial t} + \nabla \cdot (\alpha_N \rho_N \overrightarrow{v_N}) = I_N \quad (3\text{-}20)$$

where α_N is the volume fraction of phase N; ρ_N is the density of phase N (kg m^{-3}); $\overrightarrow{v_N}$ is the velocity vector (m s^{-1}) of phase N; t is the time (s); I_N is the mass interaction term (kg m^{-3} s^{-1}) or the rate of transfer of mass to the phase N from the other phase, which results from a phase change or chemical reaction. In this case, the mass interaction term will be neglected.

The equations of momentum could also be written in the i direction with substituting equation of continuity for simplification (Brennen, 2005):

$$\alpha_N \rho_N \left(\frac{\partial v_{Nk}}{\partial t} + v_{Ni} \frac{\partial v_{Nk}}{\partial x_i}\right) = \alpha_N \rho_N g_k - v_{Nk} I_N + F_{Nk} - \delta_N \left(\frac{\partial p}{\partial x_k} - \frac{\partial \tau_{ki}}{\partial x_i}\right) \quad (3\text{-}21)$$

where the subscripts i, j and k represent three directions (x, y, z axis) separately; g is the gravitational acceleration (m s^{-2}); F_{Nk} is the force per unit volume (N m^{-3}) exerted on the inclusion and follows $\sum_N F_{Nk} = 0$; δ_N is 0 for the disperse phase and 1 for the continuous phase; p is the pressure (Pa); τ_{ki} is the shear stress (Pa).

The transport equations for the realizable k-ε turbulence model (Shih et al., 1995) involving k (turbulence kinetic energy) and ε (the dissipation rate) could also be written as:

$$\frac{\partial (\rho k)}{\partial t} + \frac{\partial (\rho k v_j)}{\partial x_j} = \frac{\partial}{\partial x_j}\left[\left(\mu + \frac{\mu_t}{\sigma_k}\right)\frac{\partial k}{\partial x_j}\right] + G_k + G_b - \rho\varepsilon - Y_M + S_k \quad (3\text{-}22)$$

$$\frac{\partial(\rho\varepsilon)}{\partial t}+\frac{\partial(\rho\varepsilon v_j)}{\partial x_j}=\frac{\partial}{\partial x_j}\left[\left(\mu+\frac{\mu_t}{\sigma_\varepsilon}\right)\frac{\partial\varepsilon}{\partial x_j}\right]+\rho C_1 S_\varepsilon-\rho C_2\frac{\varepsilon^2}{k+\sqrt{\nu\varepsilon}}+C_{1\varepsilon}\frac{\varepsilon}{k}C_{3\varepsilon}G_b+S_\varepsilon \quad (3\text{-}23)$$

where $C_1=max\left[0.43,\frac{\eta}{\eta+5}\right]$; $\eta=S\frac{k}{\varepsilon}$; S is the modulus of the mean strain rate tensor, $S=\sqrt{2S_{ij}S_{ij}}$ (s^{-1}); S_{ij} is the mean strain rate, $S_{ij}=\frac{1}{2}\left(\frac{\partial v_j}{\partial x_i}+\frac{\partial v_i}{\partial x_j}\right)$ (s^{-1}); $C_{1\varepsilon}=1.44$; $C_2=1.9$; $C_{3\varepsilon}=tanh\left|\frac{v_{//}}{v_\perp}\right|$; $v_{//}$ is the component of the flow velocity parallel to the gravitational vector (m s^{-1}); $v_\perp$ is the component of the flow velocity perpendicular to the gravitational vector (m s^{-1}); σ_k is the turbulent Prandtl number for k, $\sigma_k=1.0$; σ_ε is the turbulent Prandtl number for ε, $\sigma_\varepsilon=1.2$.

Moreover, μ_t is the turbulent or eddy viscosity (Pa-s); G_k is the generation term because of the mean velocity gradients (J s^{-1} m^{-3} or kg m^{-1} s^{-3}); G_b is the generation term due to the buoyancy, (J s^{-1} m^{-3} or kg m^{-1} s^{-3}); Y_M is the effects from the fluctuating dilatation in the compressible turbulence on the overall dissipation rate (J s^{-1} m^{-3} or kg m^{-1} s^{-3}); ν is the kinematic viscosity (m^2 s^{-1}); S_k (J s^{-1} m^{-3} or kg m^{-1} s^{-3}) and S_ε (J s^{-2} m^{-3} or kg m^{-1} s^{-4}) are user-defined source terms.

In general, fluids flow through the reactor from right to left in the simulation process. The thin and small tubes attached to the geometry were used to simulate the inlets and outlets. Also, in the simulations the maximum skewness of the mesh or grid was about 0.86, which was acceptable for the following computational simulations. Two thirds of the bioreactor was filled with liquid (water), and the rest (the head space) was filled with air. Multiphase model was considered by using the Euler-Euler method. Appropriate boundary conditions were set carefully for each phase. Since the flow pattern of the water phase was what should be analyzed,

water was set as the primary phase, and air is the secondary phase. Furthermore, the pressure in the head space of the bioreactor was assumed to be atmospheric.

3.2.3 - Mathematical Modeling for Measuring Gas-Liquid Mass Transfer Coefficients

3.2.3.1 - Modeling without a Spiroid Loop

Generally, interphase mass transfer could be summarized as three steps: the transfer of oxygen from the bulk air to the interface of air and water, across the interface, and from the interface to the bulk water. To simplify the gas-liquid mass transfer, a two-film model or a two-resistance theory proposed by Whitman could be used appropriately (Whitman, 1923). According to the theory, oxygen transfer rate between phases is controlled by the diffusion rate, which is instantaneous thus leading to the equilibrium at the interphase all the time.

In the oxygen data measurement, the closed circulation loop was designed to record oxygen concentrations automatically at regular time intervals. Moreover, the recirculation flow rate from spiroid was much higher than the inlet and outlet flows, and the circulation loop can be viewed as a small outside volume of the reactor.

To determine the gas-liquid mass transfer coefficients in the original reactor without a spiroid loop, for direct comparison with the reactor with a spiroid loop, a mass balance equation could be written for this batch reactor as follows:

$$\frac{dc_L}{dt} = k_L a(c_L^* - c_L) \quad (3\text{-}24)$$

where c_L (mol lit^{-1}) is the dissolved oxygen concentration in water measured using a micro oxygen electrode where liquid can flow through; t (s) is time be measured by a stopwatch; k_L is the mass transfer coefficient (m s^{-1}); a is the gas/liquid interface area per liquid volume (m^{-1});

$k_L a$ (s^{-1}) are usually measured together as volumetric mass transfer coefficient, can be obtained using dynamic technique, as the slope of $ln\frac{(c_L^*-c_L)}{(c_L^*-c_{L0})}$ as a function of time; c_L^* (mol lit^{-1}) is the saturated oxygen concentration in water. Theoretical saturation oxygen concentration can be calculated by using Henry's Law and is associated with the operating temperature. But in this modeling, the saturation oxygen concentration was measured as the final oxygen concentration.

Equation (3-5) can also be expressed using exponentials as follows:

$$c_L = c_L^* - (c_L^* - c_{L0})\exp(-k_L a t) \quad (3\text{-}25)$$

where c_{L0} (mol lit^{-1}) is the initial dissolved oxygen concentration in the system.

3.2.3.2 - Modeling with the Spiroid Loop

The system with spiroid loop is more complicated due to the recirculation process. To simplify the calculation, the system with spiroid loop was divided into two parts, the spiroid loop and the chamber. Part of the liquid in the chamber flows through the spiroid tubing and exits the spiroid tubing back to the chamber, as shown in Figure 3.3. The mass transfer coefficients for the spiroid loop and the chamber are calculated separately to investigate the influence of the spiroid loop to the oxygen transfer.

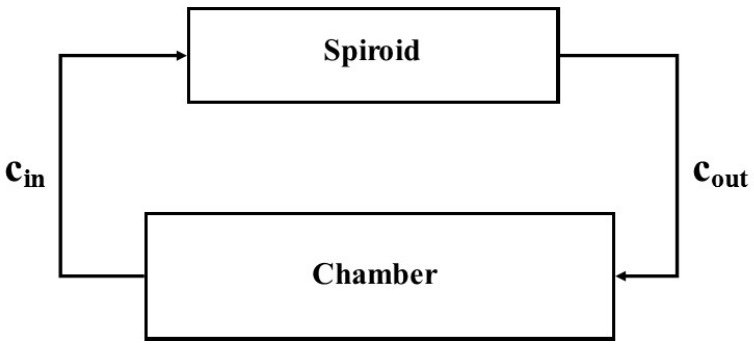

Figure 3.5. Circulation Process

To simplify the calculation for the gas-liquid mass transfer coefficient in the spiroid loop, the spiroid loop can be treated as a long tube with both inlet and outlet flows as shown in Figure 3.3. The dissolved oxygen concentration increased when moving through the spiroid loop.

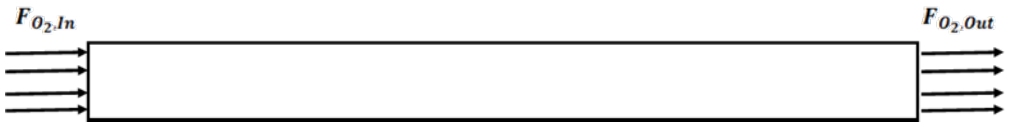

Figure 3.4. Simplified Spiroid Loop

A mass balance on the spiroid loop yields：

$$F_{O_2,In} - F_{O_2,out} + k_L a_{sp}(c_L^* - c_{out})V_{sp} = V_{sp}\frac{dc_{out}}{dt} \quad (3\text{-}26)$$

After simplifications:

$$\frac{v}{V_{sp}}(c_{in} - c_{out}) + k_L a_{sp}(c_L^* - c_{out}) = \frac{dc_{out}}{dt} \quad (3\text{-}27)$$

Similarly, a mass balance equation for the chamber could be written in the form to be consistent with the inlet and outlet of the spiroid as:

$$F_{O_2,out} - F_{O_2,In} + k_L a_c(c_L^* - c_{in})(V_r - V_{sp}) = (V_r - V_{sp})\frac{dc_{in}}{dt} \quad (3\text{-}28)$$

After simplifications:

$$\frac{v}{(V_r - V_{sp})}(c_{out} - c_{in}) + k_L a_c(c_L^* - c_{in}) = \frac{dc_{in}}{dt} \quad (3\text{-}29)$$

where $F_{O_2,in}$ and $F_{O_2,out}$ (mol s^{-1}) is the molar flow rate of dissolved oxygen entering and exiting the spiroid from and to the reactor; $k_L a_{sp}$ (s^{-1}) and $k_L a_c$ (s^{-1}) are the volumetric mass transfer

coefficient for the spiroid loop and the chamber respectively; c_{in} (mol L^{-1}) is the concentration of the dissolved oxygen in the inlet flow to spiroid, or the dissolved oxygen concentration in the chamber; c_{out} (mol L^{-1}) is the concentration of the dissolved oxygen in the outlet flow from spiroid, or the inlet concentration to the chamber; c_L^* is defined as the same as before (mol L^{-1}); v (m^3 s^{-1}) is the volumetric flow rate flowing into and exiting from spiroid loop, which could be approximately calculated based on the radius of the spiroid tube and the linear tangential velocity inside the rotational reactor at the place where the spiroid loop was attached; the linear tangential velocity is related to the rotational speed and the place where spiroid loop was attached; V_r(m^3) is the liquid volume of the bioreactor; V_{sp} (m^3) is the liquid volume of spiroid tube which involves the liquid fraction of 2/3 and the length of the spiroid tube.

Two boundary conditions are needed to solve the two differential equations. The dynamic lag in the spiroid was neglected because no obvious data changes were observed in experiment with current time scale. The boundary conditions for the spiroid loop and the chamber can be summarized as:

$$c_{in}(t=0) = c_{L0} \qquad (3\text{-}30)$$

$$c_{out}(t=0) = c_{L0} \qquad (3\text{-}31)$$

The two adjustable parameters were the volumetric mass transfer coefficients. The differential equations could be solved and fitted to the experimental data to get the volumetric mass transfer coefficients for the spiroid loop ($k_L a_{sp}$) and the chamber ($k_L a_c$), respectively.

3.3 - Results and Discussion

To investigate the effects of rotational rate and rotation direction, velocity vector simulations were performed. Normally, the fluids near a moving plane have about the same

velocity as the plane. From velocity vector (m s^{-1}) of the fluids in Figure 3.5 (a) to (c), the maximum velocity occurred at the wall of the outer cylinder and had the same value as the outer cylinder (indicated by the red color), while the minimum velocity occurred at the wall of the core cylinder and had the value of 0 (represented in blue). Also, the velocity of fluids near the core areas was nonzero from Figure 3.5 (d) and (e) due to the rotational core and core shaft at given values, which was marked in yellow. At low rotational speed, the rotating inner cylinder had little effect on the system as seen in Figure 3.5 (c), (d) and (e).

The fluid flow patterns were consistent and an increasing trend with no major differences between velocity vectors under various operating conditions (both rotational rates and rotational directions). The minor difference of velocity profiles and velocity vectors under different operating conditions was due to the low rotational velocities of the system and small difference between rotational velocities, which resulted in an almost stationary and low shear system. Thus, the operating experimental conditions selected were rotating outer cylinder at 4 rpm, 6 rpm, 8 rpm, and counter rotating cylinders only at 8 rpm (since rotational directions seemed to have minor effect on the mixing performance based on simulations).

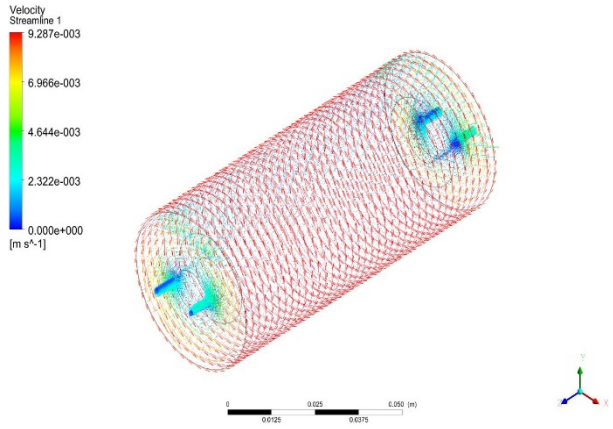

(a) Outer Cylinder Rotational at 4 rpm

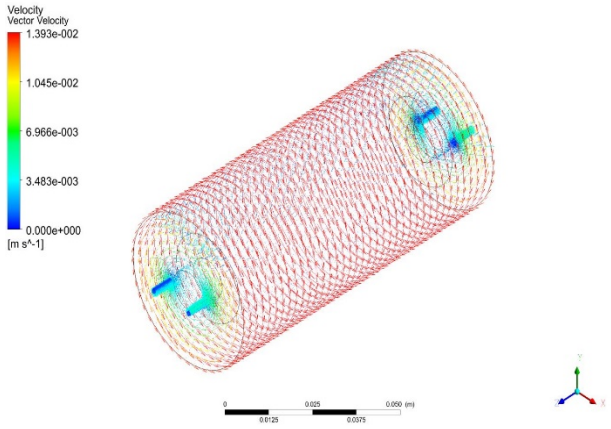

(b) Outer Cylinder Rotational at 6 rpm

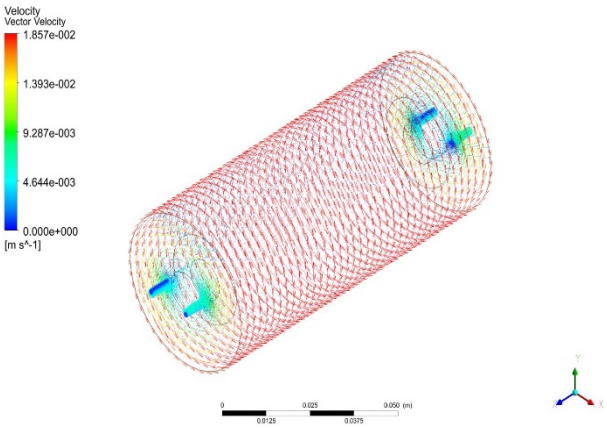

(c) Outer Cylinder Rotation at 8 rpm

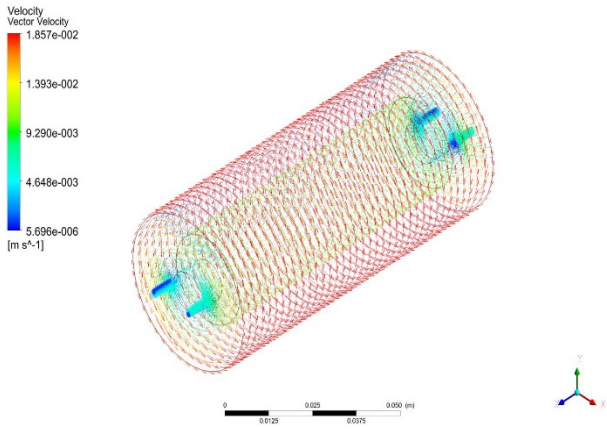

(d) Concurrent Inner and Outer Cylinder Rotation at 8 rpm

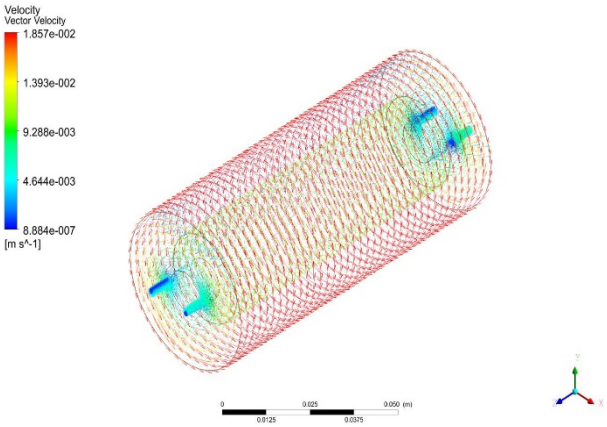

(e) Countercurrent Inner and Outer Cylinder Rotation at 8 rpm

Figure 3.6. Velocity Vectors at Various Conditions (Multiple Phases - 2/3 fluid volume)

As could be concluded from Figure 3.6, the magnitudes for average wall shear stress are small (in the order of 10^{-2}) and positively proportional to the rotational velocity. The maximum average shear stress at 8 rpm in this system was far less than the average shear stress that would inhibit the behavior of most cell lines. The rotation of the inner cylinder did increase the average wall shear stress of the system by a small amount. Considering the effects from rotational directions, the average wall shear stress did not differ much on the rotational direction of the inner cylinders, or seemed to be independent of the rotational directions at low rotational

velocities (less than 8 rpm). Thus, the outer cylinder rotation had a larger effect on the wall shear stress and velocity distribution than that of the inner cylinder.

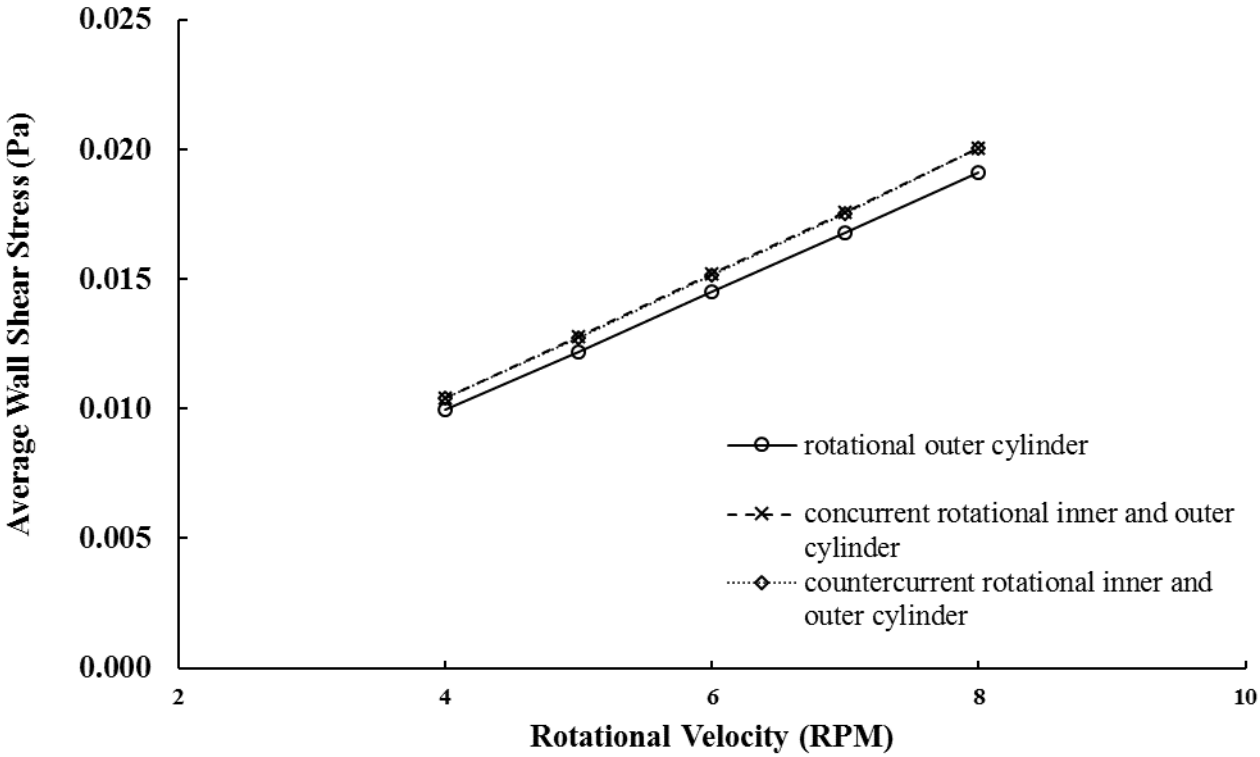

Figure 3.7. Average Shear Stress versus Rotational Velocity

Based on the CFD results, the outer cylinder was rotated at 4 rpm, 6 rpm, 8rpm, and the inner cylinder was rotated countercurrently at 8 rpm with and without the spiroid. The study of the bioreactor without spiroid was to be a comparison or a control experiment for the one with spiroid. The main purpose of this comparison was to illustrate the advantage of using spiroid, which will help improve oxygen transfer.

A minimum of five experiments were conducted under the same operating conditions. Figure 3.7 illustrates the results with standard deviations shown as an error bar. The regression lines for the oxygen data which could be obtained by using the equations discussed before were also plotted. The regression lines showed a good fit to the experimental data. As described

previously, the water used was pretreated with nitrogen, which gave near-zero initial concentrations. As the dissolved oxygen curves flatten, the concentration of oxygen in the liquid phase approached its saturation state.

As indicated in Figure 3.7, the time for oxygen to reach the equilibrium state decreased with increasing rotational speed with and without spiroid. For experiments at 4 rpm, the oxygen saturation time was about 40 minutes without the spiroid and about 20 minutes with the spiroid. The oxygen saturation time was reduced by about a maximum factor of 2, or the oxygen reached its saturation state two times more quickly with a spiroid attached.

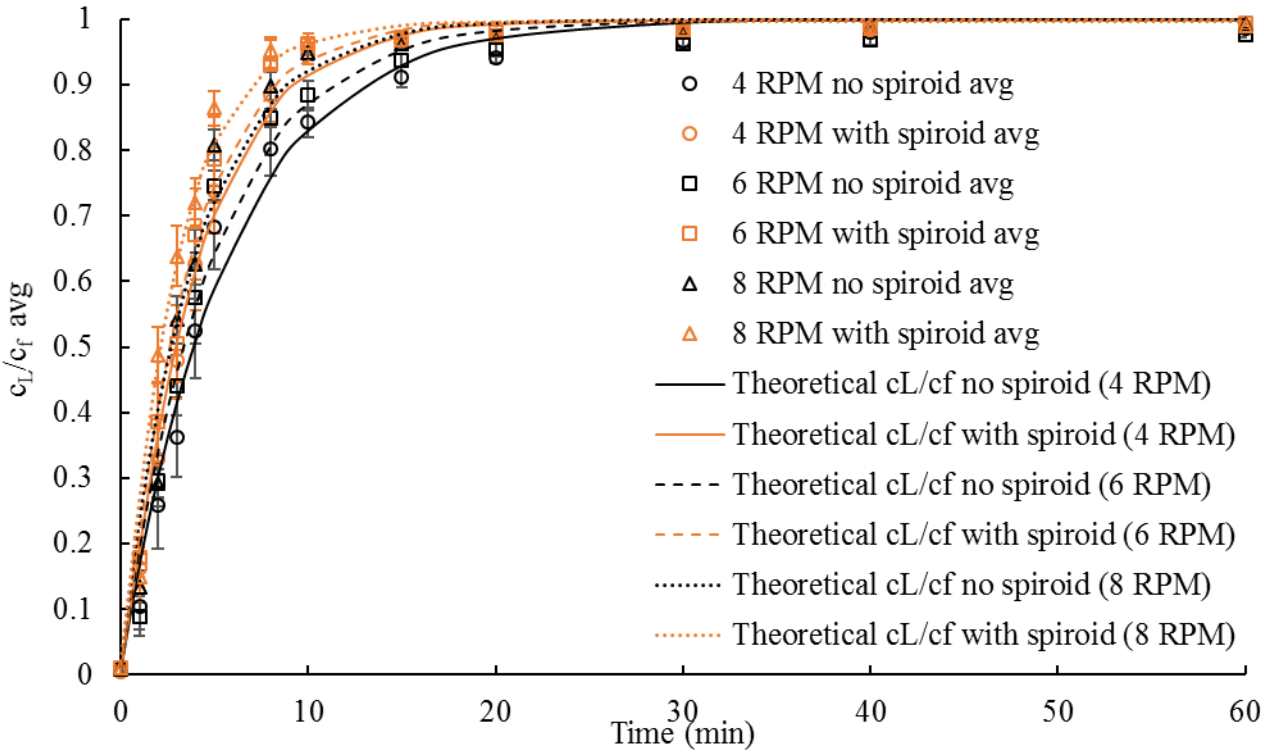

Figure 3.8. Dissolved Oxygen Concentrations Under Various Operating Conditions

As predicted by CFD simulations, the rotation direction of the inner and outer cylinders has little influence on the system at low rotational rates. Experiments of countercurrent rotation of the inner and outer cylinders at 8 rpm for the bioreactor with and without spiroid tube were

also conducted and shown in Figure 3.8. Little difference exists between the oxygen data of countercurrent rotation and the rotating only outer cylinders for both bioreactors with and without the spiroid. The effect of spiroid tube was about a factor of 1.5 in oxygen saturation time at 8 rpm.

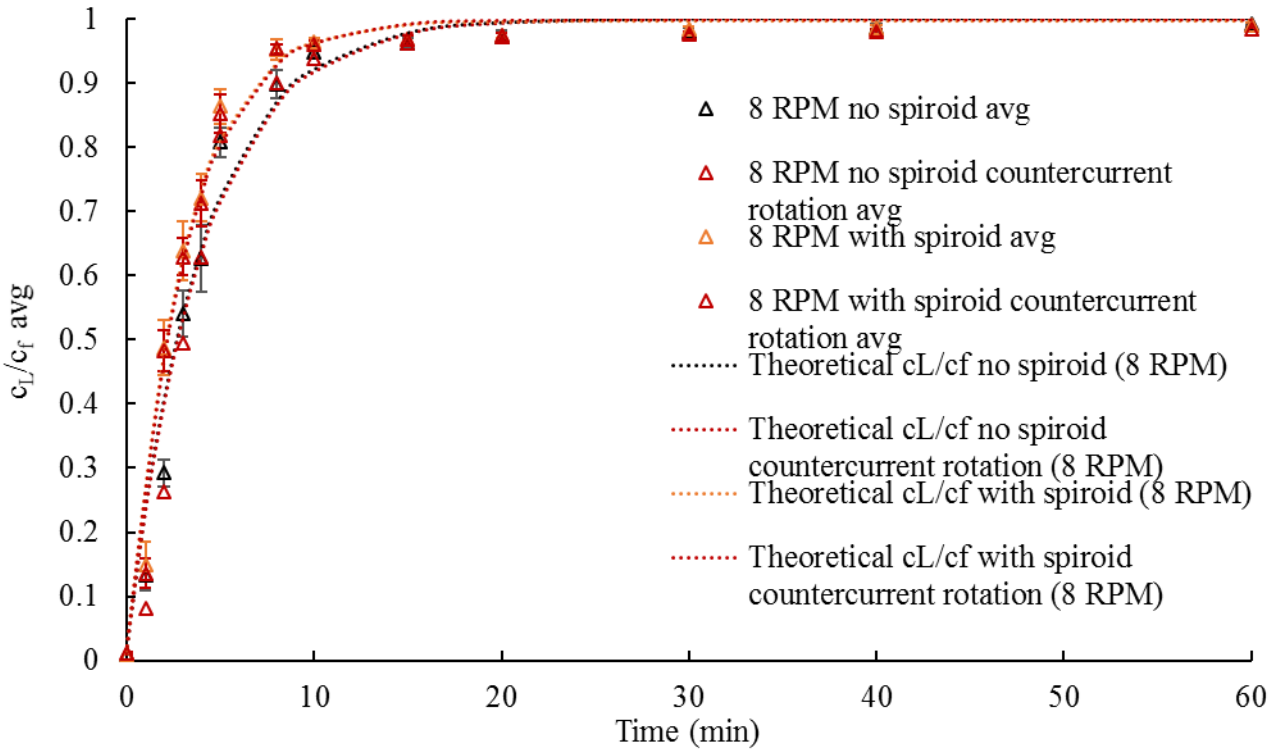

Figure 3.9. Effects of Countercurrent Rotation With and Without the Spiroid

Table 3.2 gave a summary of the calculated volumetric mass transfer coefficients (k_La) based on experimental data. From Table 3.2, though the volumetric mass transfer coefficients in the spiroid are high (about 9 times of the k_La in the bioreactor without spiroid at maximum), adding the spiroid only increased the k_La in the system by a factor of 2. Therefore, increasing the volume ratio (such as increase turns, radius of the spiroid) would further increase the oxygen transfer. Figure 3.9 shows the comparison of k_La in bioreactor with and without the spiroid and in the spiroid. The volumetric mass transfer coefficients for all cases showed a positive and

approximate linear relationship to the rotational rate. The k_La in the spiroid had the greatest increase as a function of rotational speed.

Table 3.2. Summary of the Volumetric Mass Transfer Coefficients (k_La)

Liquid Fraction	Outer Cylinder (RPM)	Inner Cylinder (RPM)	k_La (s^{-1}) without spiroid	k_La (s^{-1}) with spiroid	k_La (s^{-1}) in spiroid
2/3	4	0	0.002945	0.00423	0.0217
	6	0	0.003404	0.004607	0.02825
	8	0	0.004206	0.004838	0.03709
	8	-8	0.004124	0.004779	0.03699

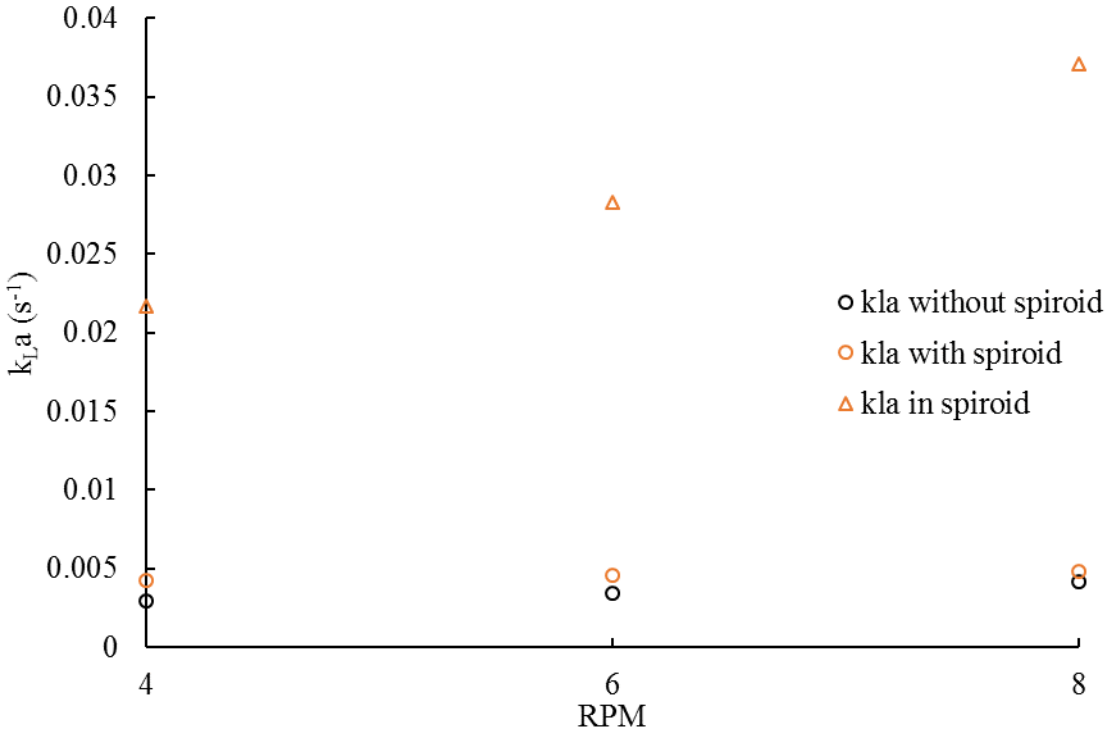

Figure 3.10. Comparison of k_La in the Bioreactor With and Without the Spiroid

3.4. Conclusions

Computational fluid dynamic (CFD) modeling was used to predict the complex flow structures in a novel bioreactor. The average shear stress caused by the bioreactor was small, providing a suitable environment for the production of cell lines. Experiments were conducted to measure oxygen concentration in the bioreactor with and without spiroid tube at 4 rpm (outer cylinder rotation), 6 rpm (outer cylinder rotation) and 8 rpm (outer cylinder rotation and countercurrent rotation). Mathematical models were also applied to calculate the volumetric mass transfer coefficients (k_La) for different operating conditions. The k_La in spiroid tube was shown to be about nine times that in the original bioreactor at maximum. By introducing the spiroid to the bioreactor, the time for oxygen to reach the saturated state was halved. The bioreactor was shown to improve the oxygen transfer performance. However, due to the small capacity of current bioreactor, scale-up is necessary in the future to develop it for cell cultivation. Also, additional modifications of the spiroid tube could increase oxygen transfer. The size of common roller bottles varies from about 10 ml to 3 L, and depends on the required cell productivity in each targeted process. The bioreactor could be envisioned to immediate scale up to 1L, which was about 9 times the original (about 110 ml), and subsequently scaling further depending on empirical improvements in subsequent steps of scale-up.

Acknowledgement

This chapter has been published in Chem. Eng. Sci. 170 (2017) 597–605

Nomenclature

c_{L0}	initial dissolved oxygen concentration in liquid phase, mol·L^{-1}
c_L	dissolved oxygen concentration in liquid phase (water), mol·L^{-1}
c_L^*	saturated oxygen concentration in liquid phase at certain temperature, mol·L^{-1}
c_f	final dissolved oxygen concentration in the bioreactor, mol·L^{-1}
c_{in}	dissolved oxygen concentration entering spiroid loop, mol·L^{-1}
c_{out}	dissolved oxygen concentration exiting from spiroid, mol·L^{-1}
C_1	constant, $C_1 = max\left[0.43, \frac{\eta}{\eta+5}\right]$
$C_{1\varepsilon}$	constant, 1.44
C_2	constant, 1.9
$C_{3\varepsilon}$	constant, $C_{3\varepsilon} = tanh\left\|\frac{v_{//}}{v_\perp}\right\|$
F_{Nk}	force per unit volume which exerts on the inclusion, N·m^{-3}
$F_{O_2,In}$	molar flow rate into the spiroid tube, mol·s^{-1}
$F_{O_2,out}$	molar flow rate out of the spiroid tube, mol·s^{-1}
g	gravitational acceleration, m·s^{-2}
g_i	ith direction component of the gravitational vector, m·s^{-2}
G_b	generation term due to the buoyancy, $G_b = \beta g_i \frac{\mu_t \partial T}{Pr_t \partial x_i}$ or $G_b = -g_i \frac{\mu_t \partial \rho}{\rho Pr_t \partial x_i}$ (for idea gases), J·(s^{-1}·m^{-3}) or kg·(m^{-1}·s^{-3})
G_k	generation term due to the mean velocity gradients, $G_k = -\rho\overline{v_i' v_j'}\frac{\partial v_j}{\partial x_i}$

	or $G_k = \mu_t S^2$ (Boussinesq hypothesis), J·(s^{-1}·m^{-3}) or kg·(m^{-1}·s^{-3})
I_N	mass interaction term, kg· (m^{-3}·s^{-1})
k	turbulence kinetic energy per unit mass, J· kg^{-1} or m^2·s^{-2}
$k_L a$	volumetric gas-liquid mass transfer coefficient, s^{-1}
$k_L a_C$	volumetric gas-liquid mass transfer coefficient in bioreactor chamber, s^{-1}
$k_L a_{sp}$	volumetric gas-liquid mass transfer coefficient in spiroid loop, s^{-1}
RPM	rotational velocity of the reactor, round per minute
S_{ij}	mean strain rate, $S_{ij} = \frac{1}{2}\left(\frac{\partial v_j}{\partial x_i} + \frac{\partial v_i}{\partial x_j}\right)$, s^{-1}
S_k	user-defined source term, J· (s^{-1}·m^{-3}) or kg· (m^{-1}·s^{-3})
S_ε	user-defined source term, J· (s^{-1}·m^{-3}) or kg· (m^{-1}·s^{-3})
t	time, s
v	volumetric flow rate through spiroid loop, L·s^{-1}
$v_{//}$	component of flow velocity parallel to the gravitational vector, m·s^{-1}
$v_\perp$	component of flow velocity perpendicular to the gravitational vector, m·s^{-1}
$\overrightarrow{v_N}$	velocity vector of phase N, m·s^{-1}
V_r	liquid volume of bioreactor, m^3
V_{sp}	liquid volume of spiroid tube, m^3
Y_M	effects from the fluctuating dilatation in the compressible turbulence on the overall dissipation rate, $Y_M = 2\rho\varepsilon M_t^2$, J· ($s^{-1}$·$m^{-3}$) or kg· ($m^{-1}$· s^{-3})

Greek Letters

α_N	volume fraction of phase N, percent
δ_N	constant, 0 for the disperse phase and 1 for the continuous phase
ε	dissipation rate, $m^2 \cdot s^{-3}$
η	constant, $\eta = S\frac{k}{\varepsilon}$
μ	molecular dynamic viscosity, Pa·s
μ_t	turbulent or eddy viscosity, Pa·s
ν	kinematic viscosity, $m^2 \cdot s^{-1}$
ρ_N	density of phase N, $kg \cdot m^{-3}$
σ_k	turbulent Prandtl number for k, $\sigma_k = 1.0$
σ_ε	turbulent Prandtl number for ε, $\sigma_\varepsilon = 1.2$
τ_{ki}	shear stress, Pa

Subscripts

i, j, k	three directions (x, y, z axis) separately

References

Abu-Reesh, I., Kargi, F., 1989. Biological Responses of Hybridoma Cells to Defined Hydrodynamic Shear Stress. J. Biotechnol. 9, 167–178.

Argyropoulos, C.D., Markatos, N.C., 2014. Recent Advances on the Numerical Modelling of Turbulent Flows. Appl. Math. Model. 39, 693–732.

Augenstein, D.C., Sinskey, A.J., Wang, D.I.C., 1971. Effect of Shear on the Death of Two Strains of Mammalian Tissue Cells. Biotechnol. Bioeng. 13, 409–418.

Belo, I., Pinheiro, R., Mota, M., 2003. Fed-Batch Cultivation of Saccharomyces Cerevisiae in a Hyperbaric Bioreactor. Biotechnol. Prog. 19, 665–671.

Ben-Ze'ev, A., Farmer, S.R., Penman, S., 1980. Protein Synthesis Requires Cell-Surface Contact While Nuclear Events Respond to Cell Shape in Anchorage-Dependent Fibroblasts. Cell 21, 365–372.

Bernstein, E.F., Blackshear, P.L., Keller, K.H., 1967. Factors Influencing Erythrocyte Destruction in Artificial Organs. Am. J. Surg. 114, 126–138.

Berson, R.E., Mane, T. V, Svihla, C.K., Hanley, T.R., 1998. Improved Oxygen Delivery in a Continuous-Roller-Bottle Reactor. Appl. Biochem. Biotechnol. 70–72, 615–627.

Blackshear, P.L., Blackshear, G.L., 1987. Mechanical Hemolysis, in: Handbook of Bioengineering. p. 15.1-15.19.

Brennen, C.E., 2005. Fundamentals of Multiphase Flows, Cambridge University Press.

Chisti, Y., 2001. Hydrodynamic Damage to Animal Cells. Crit. Rev. Biotechnol. 21, 67–110.

Chittur, K.K., McIntire, L. V., Rich, R.R., 1988. Shear Stress Effects on Human T Cell Function. Biotechnol. Prog. 4, 89–96.

Cockx, A., Do-Quang, Z., Audic, J.., Liné, A., Roustan, M., 2001. Global and Local Mass

Transfer Coefficients in Waste Water Treatment Process by Computational Fluid Dynamics. Chem. Eng. Process. Process Intensif. 40, 187–194.

Dewey, C.F., Bussolari, S.R., Gimbrone, M. a, Davies, P.F., 1981. The Dynamic Response of Vascular Endothelial Cells to Fluid Shear Stress. J. Biomech. Eng. 103, 177–185.

Dhanasekharan, K.M., Sanyal, J., Jain, A., Haidari, A., 2005. A Generalized Approach to Model Oxygen Transfer in Bioreactors Using Population Balances and Computational Fluid Dynamics. Chem. Eng. Sci. 60, 213–218.

Ede, C.J.C., Houten, R. Van, Beenacakers, A.A.C.M., 1995. Enhance of Gas to Water Mass Transfer Rates by a Dispersed Organic Phase. Chem. Enoineering Sci. 50, 2911–2922.

Farmer, S.R., Ben-Ze'av, A., Benecke, B.J., Penman, S., 1978. Altered Translatability of Messenger RNA from Suspended Anchorage-Dependent Fibroblasts: Reversal Upon Cell Attachment to A Surface. Cell 15, 627–637.

Fayolle, Y., Cockx, A., Gillot, S., Roustan, M., Héduit, A., 2007. Oxygen Transfer Prediction in Aeration Tanks Using CFD. Chem. Eng. Sci. 62, 7163–7171.

Fleischaker, R.J., Sinskey, A., 1981. Oxygen Demand and Supply in Cell Culture. Eur. J. Appl. Microbiol. Biotechnol. 12, 193–197.

Folkman, J., Moscona, A., 1978. Role of Cell Shape in Growth Control. Nature 273, 345–349.

Garcia-Ochoa, F., Gomez, E., 2009. Bioreactor scale-up and oxygen transfer rate in microbial processes: An overview. Biotechnol. Adv. 27, 153–176.

Kawase, Y., Hashimoto, N., 1996. Gas Hold-Up and Oxygen Transfer in Three-Phase External-Loop Airlift Bioreactors: Non-Newtonian Fermentation Broths. J. Chem. Technol. Biotechnol. 65, 325–334.

Maier, U., Losen, M., Büchs, J., 2004. Advances in Understanding and Modeling the Gas–Liquid

Mass Transfer in Shake Flasks. Biochem. Eng. J. 17, 155–167.

Maier, U., Losen, M., Büchs, J., 2001. Characterisation of the Gas-Liquid Mass Transfer in Shaking Bioreactors. Biochem. Eng. J. 7, 99–106.

Martin, I., Wendt, D., Heberer, M., 2004. The Role of Bioreactors in Tissue Engineering. Trends Biotechnol. 22, 80–86.

McQueen, A., Meilhoc, E., Bailey, J.E., 1987. Flow Effects on the Viability and Lysis of Suspended Mammalian Cells. Biotechnol. Lett. 9, 831–836.

Mudde, R.F., Van Den Akker, H.E. a, 2001. 2D and 3D Simulations of an Internal Airlift Loop Reactor on the Basis of a Two-Fluid Model. Chem. Eng. Sci. 56, 6351–6358.

Petersen, J.F., Mcintire, L. V., Papoutsakis, E.T., 1988. Shear Sensitivity of Cultured Hybridoma Cells (CRL-8018) Depends on Mode of Growth, Culture Age and Metabolite Concentration. J. Biotechnol. 7, 229–246.

Schmid-schoenbein, G.W., Fung, Y., Zweifach, B.W., 1975. Vascular Endothelium-Leukocyte Interaction: Sticking Shear Force in Venules. Circ. Res. 36, 173–184.

Shih, T.H., Liou, W.W., Shabbir, A., Yang, Z., Zhu, J., 1995. A New K-epsilon Eddy Viscosity Model for High Reynolds Number Turbulent Flows: Model Development and Validation. Comput. Fluids 24, 227–238.

Stathopoulos, N. a, Hellums, J.D., 1985. Shear Stress Effects on Human Embryonic Kidney Cells in Vitro. Biotechnol. Bioeng. 27, 1021–1026.

Suresh, S., Srivastava, V., Mishra, I., 2009. Techniques for Oxygen Transfer Measurement in Bioreactors: a Review. J. Chem. Technol. Biotechnol. 84, 1091–1103.

Vardar, F., Lilly, M., 1982. Effect of Cycling Dissolved Oxygen Concentrations on Product Formation in Penicillin Fermentations. Eur. J. Appl. Microbiol. Biotechnol. 14, 203–211.

Whitman, W.G., 1923. The two-film theory of gas absorption. Chem. Metall. Eng. 29, 146–148.

Ziegelstein, R.C., Cheng, L., Capogrossi, M.C., 1992. Flow-Dependent Cytosolic Acidification of Vascular Endothelial Cells. Science (80-.). 258, 656–659.

Chapter 4 – Design and Simulation of a Continuous Bioreactor

Abstract

This research investigates a novel continuous bioreactor with significant improvement in gas-liquid and medium mixing. This bioreactor has dramatic advantages in cell cultivation because of the high cell survival rate, enhanced growth rate, and overall high productivity. The bioreactor consists of an outer shell cylinder and inner core cylinder, each with adjustable rotational velocities to control the mixing in the reactor. Inlet flows are controlled to provide additional medium and oxygen to the reactor volume.

Computational fluid dynamics (CFD) simulations were performed to determine the range of flow patterns possible in this bioreactor. The steady state operation was assumed to reduce the time for convergence. Simulations are conducted for multiphase fluids under various operating conditions (different rotational rates and different rotational directions) to simulate the actual reaction environment and to investigate the mixing performance of the bioreactor. From simulations, shear stress caused by the bioreactor was small (the order of magnitude was 10^{-1}), providing a more suitable environment for cell production. In addition, the rotation and rotation direction of inner cylinder has smaller impact than rotating outer cylinder to the bioreactor at low rotational velocity, based on the small increase and overlapping lines in profiles of velocity, shear stress, turbulence kinetic energy (k) and eddy dissipation rate (ε) when rotation inner cylinder was enabled.

Key Words: computational fluid dynamics, continuous bioreactor, oxygen transfer

4.1. Introduction

Bioreactors have large potential to be applied in the large scale of industry process to result in high productivity. Various bioreactors have already been researched by scientists. In many biological cell cultivations, the oxygen transport and mixing performance of the bioreactor are normally considered to be two of the most limiting factors for the production results.

In recent years, computational fluid dynamic (CFD) tools are used widely to predict the fluid pattern and study the hydrodynamics of the bioreactors. Mudde (2001) used two- and three dimensional (2D and 3D) simulations to predict the liquid circulation rate and gas fraction of an airlift reactor under steady state at low gas flow rates. The two-fluid flow with a modified k-ε turbulence model was used. The 2D (using developed code) and 3D simulations (using FLUENT 4.5) were found to be in good agreement with the mechanical energy balance (1D) (Mudde and Van Den Akker, 2001). The three-dimensional CFD results were considered to be more realistic than two-dimensional ones as a result of the deviations when compared to the LDA data.

Dhanasekharan (2005) proposed a generalized method to model oxygen transfer in airlift bioreactors. The standard k-ε model was used to simulate the turbulence (Dhanasekharan et al., 2005). The results (gas holdup and volumetric mass transfer coefficients) obtained from the three-dimensional CFD simulation (by using FLUENT 6) for two-phase flow (air and water) using a full multi-fluid Eulerian model were compared with the experimental data of Kawase and Hashimoto (1996). The overall predictions were in the same order and were in good agreement with experiment.

In Fayolle's work (2007), an experimentally validated numerical tool based on computational fluid dynamics (accomplished FLUENT 6.2) was used. The Euler-Euler model

derived from the Navier-Stokes equations was selected to simulate the bubbly flow. The local axial velocity and gas hold-up were well reproduced by the CFD model both at the operating conditions of aeration and no aeration. The measurement error for mean axial liquid velocity was found to be around ten percent, and five percent for volumetric oxygen transfer coefficient (Fayolle et al., 2007). Simulation results were consistent with the fact that a larger bubble size will induce a smaller oxygen transfer coefficient.

Santhosh (2010) investigated the effect of rotational Reynolds number (Re_Ω) and axial Reynolds number (Re_a) on heat transfer and fluid flow in an annulus (radius ratio of 0.5) with an inner rotating cylinder and outer stationary wall. Two dimensional axial symmetric steady and incompressible flow (air) was simulated by CFD (FLUENT 6.3). The standard k-ε model was coupled with the incompressible Navier-Stokes equations. The effect of rotational Reynolds number on axial velocity occurred only when the axial Reynolds number was small, while the axial Reynolds number did not affect swirl velocity significantly (Sukumaran et al., 2010). The computational work was validated with experimental work.

Perez et al. (2013) simulated the turbulent flow of a rotating cylinder electrode with different geometry of counter electrodes (four-plate, six-plate and concentric cylinder). The Reynolds averaged Navier-Stokes (RANS) equation along with turbulent viscosity and the standard k-ε turbulence model was solved by using boundary conditions of universal logarithmic wall function (Pérez and Nava, 2013). The arrangement of four-plate and six-plate was showed to develop turbulent Taylor vortex flow via 3-D simulations. Moreover, the hydrodynamics of the concentric situation was found to be superior to other two cases because of the quasi stagnant zones caused by plates near to plates and on the wall free of plates.

This research investigated the use of an automated, horizontally-rotating bioreactor consisting of a rotating outer cylindrical shell and a counter-rotating core operated at various conditions. The bioreactor has a small volume of 1.109×10^{-4} m^3. The small flow rate (velocity at 6.926×10^{-4} m s^{-1} or total flow rate of 1.2180×10^{-7} m^3 min^{-1}) of the inlet made the bioreactor a continuous system and provides additional medium with little effect to the system. The revolving cylinders with appropriate velocities improve the mixing performance without causing cell damage on account of the low shear stress predicted from CFD simulations. Furthermore, a spiroid tubing (8 turns) was attached to the wall of outer cylinder at desired position and was proved to improve the oxygen transfer phenomena.

In addition, CFD simulations were used to analyze the possible behavior of the fluids and mixing performance in this novel bioreactor under the multiphase situation. Simulations were conducted under various operating conditions (4 rpm, 6 rpm, 8 rpm) that would occur in the experiments in order to find out the most optimized one. Results obtained from simulations were important auxiliary materials for further experiments. Moreover, the optimized operating conditions will be used in the scaling-up session.

4.2. Summary of the Invention

Roller bottles are commonly used in the cell cultivation. However, the performance of roller bottles is limited to their batch operation. A continuous bioreactor is more attractive because the medium or the air can be added to the system continuously to increase the growth rate of cells and cell products. This novel reactor is the combination of these two kinds of reactors.

Figure 4.1 illustrates the bioreactor. Figure 4.1(b) illustrates the structure for this bioreactor. Figure 4.1 (c) and (d) are images of outer cylinder with spiroid tubing, produced using PLA via a 3D printer. This reactor consists of an outer cylinder, or is called as shell, and an inner cylinder, or is named as core, each with adjustable rotational velocities to provide a variable shear-rate environment and control the mixing performance in this reactor. The spiroid tubing with appropriate dimension was attached to the outer cylinder is designed to improve the oxygen transport through increasing the gas-liquid contact areas. Two motors allow independent rotation of the outer and inner cylinder of the bioreactor, either in concurrent or in countercurrent rotation. Two ports are located on the hubs at each side, allowing the two inlets and two outlets. This reactor can be operated either in the batch mode or the continuous mode. In addition, it may be fed, perfused, and sampled automatically with or without operator intervention. Moreover, leaking was not the problem for this reactor. The reactor has been operated without the leaking issues for more than one month.

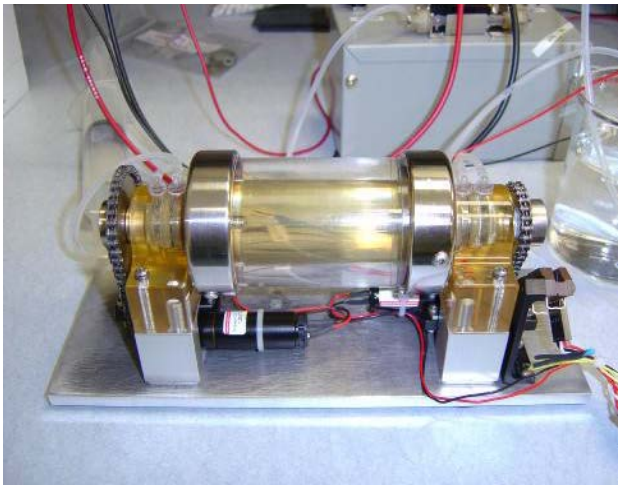

(a) Image of Novel Bioreactor

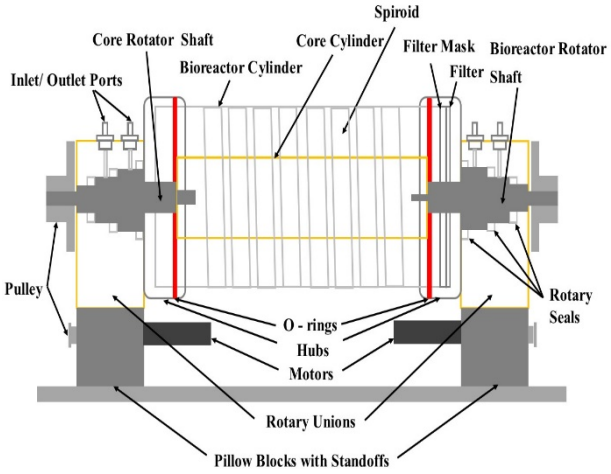

(b) Design of Novel Bioreactor with spiroid

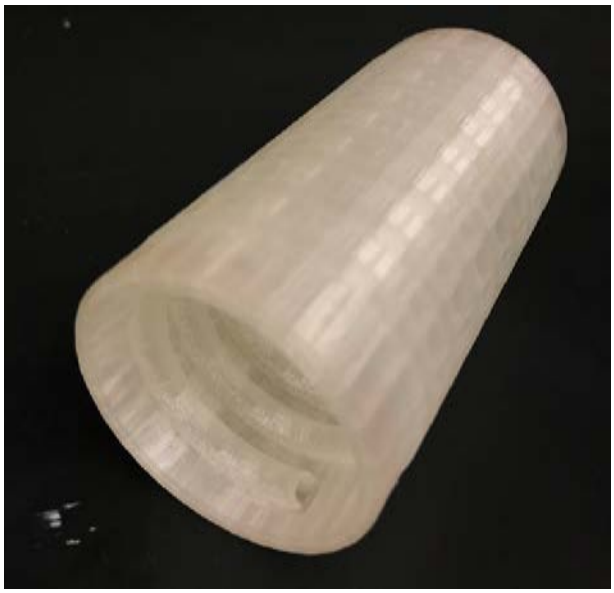

(c) Geometry of the Shell with Spiroid Tubing (d) Geometry of the Core

Figure 4.11. The Novel Bioreactor Sketch

4.3. Computational Dynamic Fluid Simulations

ANSYS workbench 16.0 was used in this research to carry out the simulations. The basic steps for a computational simulation are as follows:

- Construct the geometry (ANSYS Design Modeler was used in this research);
- Generate the simulation mesh using ANSYS Meshing;
- Perform simulations;
- Analyze the results using ANSYS CFD-post

Some appropriate assumptions should also be made in the computational dynamic fluid simulations:

- Steady State
- Homogenous

- Newtonian Fluids (in this case, water was used)
- Incompressible Fluids
- Isothermal Process
- Pressure Based Model
- Gravity Existence

4.3.1. Geometry

The geometry of this reactor was created in the ANSYS Design Modeler 16.0 (Ansys, Inc., Canonsburg, PA, US). The sizing information for the bioreactor and the spiroid tubing was shown in Table 4.1. Geometry was constructed in ANSYS Design Modeler 16.0, which is shown in Figure 4.2 (a). It was more convenient to see through the system in Figure 4.3 (b). Figure 4.3 (c) and (d) show geometries of the spiroid tubing attached to the wall of shell and were constructed through ANSYS Design Modeler 16.0.

Table 4.3. Dimensions of Bioreactor

Parameter	Value (m)
Core Length	0.08580
Core Shaft Length	0.003200
Hub Part Length	0.003759
Inlet/Outlet Tubes' Length	0.006833
Shell Length	0.1006
Shell Shaft Length	0.007823
Spiroid Tubing Length	1.102
Core Diameter	0.02545
Inlet/Outlet Ports Diameter	0.001366
Shafts' Diameter	0.01168
Shell Inner Diameter (I.D.)	0.04445
Shell Outer Diameter (O.D.)	0.05080
Spiroid Tubing Inner Diameter (I.D.)	0.004763
Spiroid Tubing Outer Diameter (O.D.)	0.006350

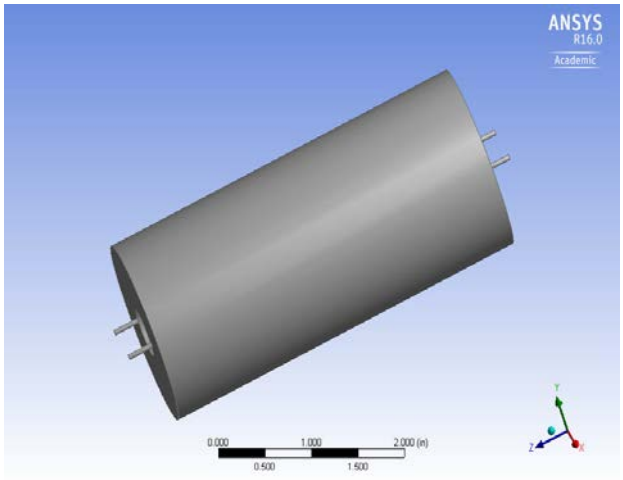

(a) Geometry in ANSYS Design Modeler 16.0

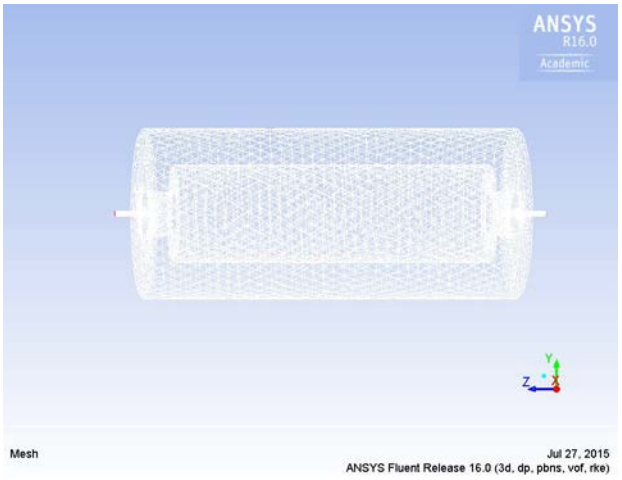

(b) Geometry in ANSYS FLUENT 16.0

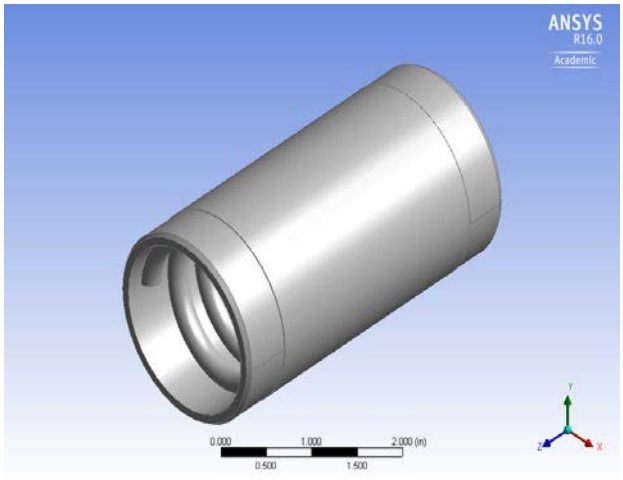

(c) Geometry of the Shell with Spiroid Tubing

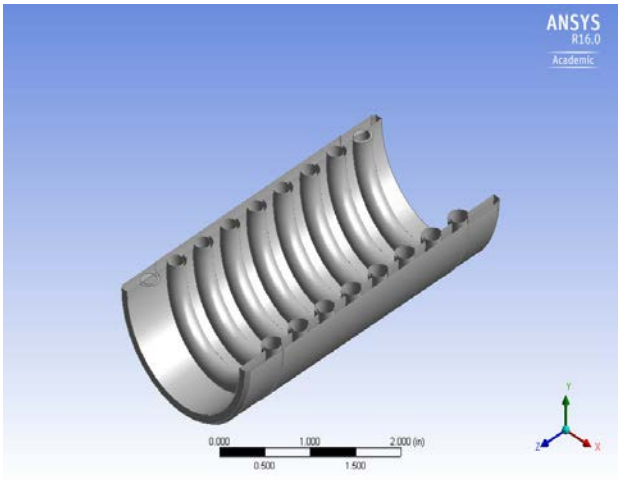

(d) Geometry of the Shell with Spiroid Tubing (Inside View)

Figure 4.12. The Novel Bioreactor Geometry (ANSYS Workbench 16.0)

In general, fluids flow through the reactor from right to left in the simulation process. The thin and small tubes attached to the geometry was used to simulate the inlets and outlets. As described previously, two motors rotate the core and shell independently. The right inner cylinder consists of core rotator shaft (next to core) and hub part (next to inlets). The outside part of core rotator shaft was connected to the motor via a gear, and the inside part was

connected to the core. The left inner cylinder was the shell rotator shaft, which would have the same angular velocity as the outer cylinder. The hub was also connected to the shell, with the hub rotated in the same direction and velocity as the shell and shell shaft.

4.3.2. Grid

The mechanical package in the ANSYS workbench16.0 was used to generate a volume mesh before starting computational dynamic calculations in FLUENT. The physics preference was set as CFD. In addition, the mesh was generated by using automatic meshing method with patch conforming algorithm and specific sizing for important areas to generate tetrahedral elements. The proximity and curvature were enabled as the advanced size function to get a better mesh performance. Furthermore, each part of the bioreactor was defined (or created as name selection) in the meshing process for convenient uses in boundary conditions from the dynamic fluids calculations in next step. The grid of this bioreactor was showed in Figure 4.3. Figure 4.3 (a) was the overall mesh for the bioreactor, and (b) illustrated the details of this mesh result.

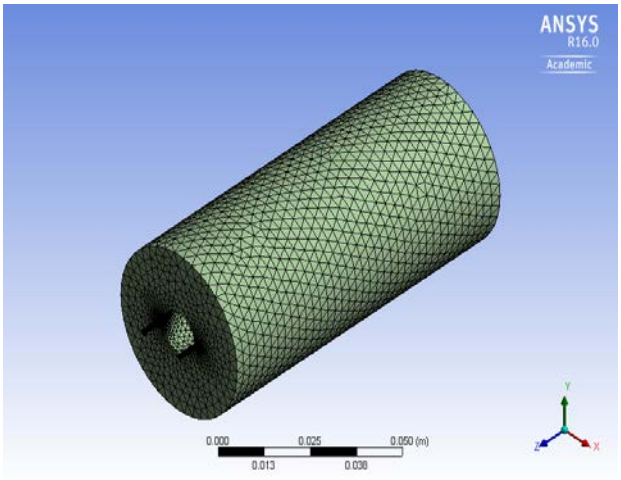

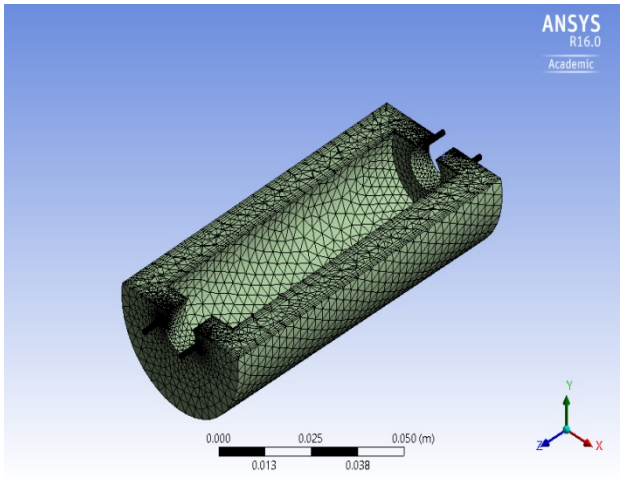

(a) Overall Mesh of the Bioreactor (b) Mesh of the Bioreactor (Inside View)

Figure 4.13. The Meshed Geometry Model in ANSYS Meshing 16.0 (The skewness for mesh metric was 0.86)

The quality of the meshing affects the simulation results; the iteration time and computational requirements will be different for different meshing quality. Mesh should be adjusted depending on different flow rates. It should be generated heavily for the corners of the chambers, the wall areas, and inlet and outlet areas. Normally, good mesh quality has a minimum orthogonal quality larger than 0.1, or maximum skewness smaller than 0.95, both of which could be found in the meshing statics tab in ANSYS mesh. In the simulations of this work, by using different dimension mesh to calculate and then analyzing the differences (or mesh sensitivity analysis), the maximum skewness of the mesh or grid was adjusted to about 0.86, which was acceptable for the following computational simulations.

4.4.3. Modeling

4.4.3.1. Theory

Reynolds number based on annulus gap in concentric cylinders with outer cylinder rotation with no axial pressure gradient could be described as (Bilgen and Boulos, 1973; Lathrop et al., 1992):

$$R_{e_{\phi m}} = \frac{\rho \Omega_o r_o (r_o - r_i)}{\mu} \qquad (2\text{-}32)$$

where ρ is the density of the fluids (kg m^{-3}); Ω_o is the angular velocity of outer cylinder (radians per s); r_o is the radius of outer cylinder (m); r_i is the radius of inner cylinder (m); μ is the dynamic viscosity of the fluids (Pa-s or kg m^{-1} s^{-1}).

Based on Reynolds Number, the fluids in this system at selected operating conditions (4 rpm, 6 rpm, 8 rpm) were in a region of low turbulence. Two equation turbulence models (derived from Reynolds Averaged Navier-Stokes or RANS equations) are one of the most widely used and economic models to solve the practical engineering problems. Two extra transport equations are used in two equation models to describe the turbulent flow in addition to the mean-flow Navier-Stokes equations. The k-ε model and k-ω model are the common models that are based on two equation transport models. The first term k refers to the turbulence kinetic energy, which determine the energy in the turbulent flow; the second variable ε represent the rate of dissipation of kinetic energy, or ω means the specific dissipation, which determines the scale of the turbulence.

The k-ω model predicts flow region well near boundary (wall) by using a low-Reynolds number formulation instead of a wall function based on mesh quality. Thus, it requires fine grid spacing near the wall region. The k-ω turbulence model gives higher performance in predicting boundary layers with adverse pressure gradient and has significant numerical stability (Argyropoulos and Markatos, 2014). However, it has more difficulty in converging and requires higher accurate initial guess at the solution.

Though the k-ε model may not be applicable for large adverse pressure gradient, it is one of the most common used turbulence models. The standard k-ε model is normally used to describe turbulence in the practical industrial flow calculations owing to its advantages of computational economy and reasonable accuracy. Exact equations are used to obtain the turbulence kinetic energy (k). However, since physical reasoning is used to derive its dissipation rate (ε), the standard k-ε model is only valid for fully developed turbulence. The standard k-ε model is not suitable for flows involving separation and strong streamline curvature. In virtue of

its restrictions, other two turbulence model could be introduced. The RNG (renormalization group) k-ε model is very similar to standard k- ε model, but it can describe more turbulent flows in a more comprehensive way. It renormalizes the instantaneous Navier-Stokes equations using a mathematical technique. It is more accurate for the flows than standard k-ε model as it includes an additional term in its ε equation, the effects of swirl in the model, an analytical formula for turbulent Prandtl numbers, and the effects of low-Reynolds number on effective viscosity. The realizable k-ε model is another turbulence model. The turbulent viscosity is derived from a different equation in the realizable k-ε model. In addition, in realizable k-ε model, a modified equation is used to calculate the turbulent dissipation rate ε accounting for the mean-square vorticity fluctuation. The realizable k-ε model satisfies uniquely the realizable constraints on the normal Reynolds stresses and the unequal Schwartz shear stresses for the turbulent flow among any other k-epsilon turbulence models (ANSYS Inc., 2012; Argyropoulos and Markatos, 2014).

In this study, the realizable k-ε turbulence model in combination with the Enhanced Wall Treatment (EWT) (which has the most consistent wall shear stress and is least sensible to y+ values) was applied in this research.

For a two-phase (air and water, or dispersed and continuous phase) system, the equation of continuity for phase N (gas or liquid phase) with volume fraction of α_N could be written as follows:

$$\frac{\partial \alpha_N \rho_N}{\partial t} + \nabla \cdot (\alpha_N \rho_N \overrightarrow{v_N}) = I_N \quad (4\text{-}33)$$

where α_N is the volume fraction of phase N; ρ_N is the density of phase N (kg m^{-3}); $\overrightarrow{v_N}$ is the velocity vector (m s^{-1}) of phase N; t is the time (s); I_N is the mass interaction term (kg m^{-3} s^{-1}) or

the rate of transfer of mass to the phase N from the other phase, which results from a phase change or chemical reaction. In this case, the mass interaction term will be neglected.

The equations of momentum could also be written in i direction for simplification (Brennen, 2005):

$$\frac{\partial(\alpha_N \rho_N v_{Nk})}{\partial t} + \frac{\partial}{\partial x_i}(\rho_N \alpha_N v_{Ni} v_{Nk}) = \alpha_N \rho_N g_k + F_{Nk} - \delta_N \left(\frac{\partial p}{\partial x_k} - \frac{\partial \tau_{ki}}{\partial x_i}\right) \quad (4\text{-}34)$$

where the subscript i, j, k represent three directions (x, y, z axis) separately; g is the gravitational acceleration (m s^{-2}); F_{Nk} is the force per unit volume (N m^{-3}) which exerts on the inclusion and follows $\sum_N F_{Nk} = 0$; δ_N is 0 for the disperse phase and 1 for the continuous phase; p is the pressure (Pa); τ_{ki} is the shear stress (Pa).

The force excreted on the phase N by the other effects F_{Nk} could also be written as follows (Brennen, 2005):

$$F_{Dk} = -F_{Ck} = -\alpha_D \frac{\partial p}{\partial x_k} + F'_{Dk} \quad (4\text{-}35)$$

where the index C and D denote continuous and dispersed phase respectively; F'_{Dk} is the force per unit volume (N m^{-3}) owing to the relative motion between the phases.

The left side of Equation 3-2 could be rearranged and substituted with equation of continuity (Equation 3-1):

$$\alpha_N \rho_N \left(\frac{\partial v_{Nk}}{\partial t} + v_{Ni} \frac{\partial v_{Nk}}{\partial x_i}\right) = \alpha_N \rho_N g_k - v_{Nk} I_N + F_{Nk} - \delta_N \left(\frac{\partial p}{\partial x_k} - \frac{\partial \tau_{ki}}{\partial x_i}\right) \quad (4\text{-}36)$$

The transport equations for the turbulence model involving k (turbulence kinetic energy) and ε (the dissipation rate) could also be written as (ANSYS Inc., 2012):

$$\frac{\partial(\rho k)}{\partial t}+\frac{\partial(\rho k v_j)}{\partial x_j}=\frac{\partial}{\partial x_j}\left[\left(\mu+\frac{\mu_t}{\sigma_k}\right)\frac{\partial k}{\partial x_j}\right]+G_k+G_b-\rho\varepsilon-Y_M+S_k \quad (4\text{-}37)$$

$$\frac{\partial(\rho\varepsilon)}{\partial t}+\frac{\partial(\rho\varepsilon v_j)}{\partial x_j}=\frac{\partial}{\partial x_j}\left[\left(\mu+\frac{\mu_t}{\sigma_\varepsilon}\right)\frac{\partial \varepsilon}{\partial x_j}\right]+\rho C_1 S_\varepsilon-\rho C_2\frac{\varepsilon^2}{k+\sqrt{\nu\varepsilon}}+C_{1\varepsilon}\frac{\varepsilon}{k}C_{3\varepsilon}G_b+S_\varepsilon \quad (4\text{-}38)$$

where $C_1=max\left[0.43,\frac{\eta}{\eta+5}\right]$; $\eta=S\frac{k}{\varepsilon}$; S is the modulus of the mean strain rate tensor, $S=\sqrt{2S_{ij}S_{ij}}$ (s^{-1}); S_{ij} is the mean strain rate, $S_{ij}=\frac{1}{2}\left(\frac{\partial v_j}{\partial x_i}+\frac{\partial v_i}{\partial x_j}\right)$ (s^{-1}); $C_{1\varepsilon}=1.44$; $C_2=1.9$; $C_{3\varepsilon}=tanh\left|\frac{v_{//}}{v_\perp}\right|$; $v_{//}$ is the component of the flow velocity parallel to the gravitational vector (m s^{-1}); $v_\perp$ is the component of the flow velocity perpendicular to the gravitational vector (m s^{-1}); σ_k is the turbulent Prandtl number for k, $\sigma_k=1.0$; σ_ε is the turbulent Prandtl number for ε, $\sigma_\varepsilon=1.2$.

Moreover, k is the turbulence kinetic energy per unit mass (J kg^{-1} or m^2 s^{-2}); μ is the molecular dynamic viscosity (Pa-s); μ_t is the turbulent or eddy viscosity (Pa-s); G_k is the generation term because of the mean velocity gradients (J s^{-1} m^{-3} or kg m^{-1} s^{-3}); G_b is the generation term due to the buoyancy, (J s^{-1} m^{-3} or kg m^{-1} s^{-3}); ε is the dissipation rate per unit mass (J kg^{-1} s^{-1} or m^2 s^{-3}); Y_M is the effects from the fluctuating dilatation in the compressible turbulence on the overall dissipation rate (J s^{-1} m^{-3} or kg m^{-1} s^{-3}); ν is the kinematic viscosity (m^2 s^{-1}); S_k (J s^{-1} m^{-3} or kg m^{-1} s^{-3}) and S_ε (J s^{-2} m^{-3} or kg m^{-1} s^{-4}) are user-defined source terms.

The eddy viscosity μ_t could be obtained through following equations (ANSYS Inc., 2012).

$$\mu_t=\rho C_\mu\frac{k^2}{\varepsilon} \quad (4\text{-}39)$$

where $C_\mu = \frac{1}{A_0 + A_S \frac{kU^*}{\varepsilon}}$; $A_0 = 4.04$; $A_S = \sqrt{6}cos\phi$; $\phi = \frac{1}{3}cos^{-1}(\sqrt{6}W)$; $W = \frac{S_{ij}S_{jk}S_{ki}}{\tilde{S}^3}$; $\tilde{S} = \sqrt{S_{ij}S_{ij}}$ (s^{-1}); $S_{ij} = \frac{1}{2}\left(\frac{\partial v_j}{\partial x_i} + \frac{\partial v_i}{\partial x_j}\right)$ (s^{-1}); $U^* = \sqrt{S_{ij}S_{ij} + \widetilde{\Omega}_{ij}\widetilde{\Omega}_{ij}}$ (s^{-1}); $\widetilde{\Omega}_{ij} = \Omega_{ij} - 2\varepsilon_{ijk}\omega_k$ (s^{-1}); $\Omega_{ij} = \overline{\Omega}_{ij} - \varepsilon_{ijk}\omega_k$ (s^{-1}); $\overline{\Omega}_{ij}$ is the mean rate of rotation tensor based on a moving reference frame, $\overline{\Omega}_{ij} = \frac{1}{2}\left(\frac{\partial v_i}{\partial x_j} - \frac{\partial v_j}{\partial x_i}\right)$ (s^{-1}); ε_{ijk} is the permutation symbol, $\varepsilon_{ijk} = \frac{1}{2}(i-j)(j-k)(k-i)$; ω_k is the angular velocity of the moving reference frame (radians per second).

The generation or production of turbulence kinetic energy G_k could be given by the following equation (ANSYS Inc., 2012):

$$G_k = -\rho\overline{v_i'v_j'}\frac{\partial v_j}{\partial x_i} \quad (4\text{-}40)$$

where $\overline{v_i'}$ and $\overline{v_j'}$ are the mean fluctuating velocity components (m s^{-1}). G_k could also be calculated based on the Boussinesq hypothesis as $G_k = \mu_t S^2$, where $S = \sqrt{2S_{ij}S_{ij}}$ (s^{-1}); $S_{ij} = \frac{1}{2}\left(\frac{\partial v_j}{\partial x_i} + \frac{\partial v_i}{\partial x_j}\right)$ (s^{-1}).

In addition, the generation term resulted from the buoyancy G_b could be defined as follows (ANSYS Inc., 2012):

$$G_b = \beta g_i \frac{\mu_t \partial T}{Pr_t \partial x_i} \quad (4\text{-}41)$$

where β is the thermal expansion, $\beta = -\frac{1}{\rho}\left(\frac{\partial \rho}{\partial T}\right)_p$ (K^{-1}); g_i is the ith direction component of the gravitational vector, (m s^{-2}); μ_t is the turbulent or eddy viscosity (Pa-s); Pr_t is the turbulent Prandtl number, $Pr_t = \frac{\mu c_p}{k_c}$, the default value of Pr_t for realizable k- ε models is 0.85; μ is the molecular dynamic viscosity (Pa-s); c_p is the specific heat (J kg^{-1} K^{-1}); k_c is the thermal

conductivity, (W m^{-1} K^{-1}); T is the temperature (K). For ideal gases, G_b could also be obtained through $G_b = -g_i \frac{\mu_t \partial \rho}{\rho Pr_t \partial x_i}$.

The term involved compressibility effects Y_M could be calculated according to Sarkar and Balakrihnan's propose (Sarkar and Lakshmanan, 1990):

$$Y_M = 2\rho\varepsilon M_t^2 \qquad (4\text{-}42)$$

where M_t is the turbulent Mach number, $M_t = \sqrt{\frac{k}{a^2}}$; a is the speed of sound, $a = \sqrt{\gamma R_m T}$ (m s^{-1}); γ is the ratio of specific heats (adiabatic index), $\gamma = 1.4$ for calorically perfect air; R_m is the gas constant, $R_m = 286$ (m^2 s^{-2} K^{-1}) for ideal gas; T is the temperature (K).

4.4.3.2. Operating Parameters

Pressure-based solver and density-based solver are two numerical methods in ANSYS FLUENT. In general, pressure-based solver is applied for incompressible flows with low speed, while the density-based solver is good for compressible flows with high speed. In pressure-based solver, the pressure field is achieved by solving a pressure correction equation which derived from continuity and momentum equations. In density-based solver, the density field was obtained by solving continuity equations, and the equation of state was used to determine the pressure field. In this research, a pressure-based model with absolute velocity formulation was used, since the velocity of the fluids was small, and fluids were assumed to be incompressible. The gravity option was enabled (9.81 m s^{-2} in negative y direction) for the system. All simulations were assumed to be in steady state.

Two thirds of the bioreactor were filled with liquid (water), and the rest (the head space) was filled with air. Multiphase model was used to simulate the fluid patterns in the bioreactor.

Multiphase flows could be categorized into four: gas-liquid (used in this research) or liquid-liquid; gas-solid; three-phase flows. Euler-Lagrange and Euler-Euler were two approaches in the multiphase modeling. The Euler-Lagrange method is applicable when particle-particle interactions and the dispersed second phase can be neglected, such as spray dryers, coal and liquid fuel combustion. In the Euler-Euler method, the conservation equations are solved for each phase in similar structure, and the different phases were assumed as interpenetrating each other. The Euler-Euler method includes: the volume of fluid (VOF) model, the mixture model, and the Eulerian model. The VOF model is useful in modeling two or more immiscible fluids. The mixture model is a simplified multiphase model and is a good substitute for the full Eulerian multiphase model. Besides, the mixture model can be applied in modeling multiphase flows with different velocities of phases and homogeneous multiphase flows with strong coupling. The Eulerian model is the most complicate multiphase model. The Eulerian model can model any number of secondary phases within the limit of computational memory, and calculate each phase using an Eulerian treatment. However, the convergence is the normally the problem for Eulerian model for complex multiphase flows.

The volume of fluids (VOF) was the type of multiphase that was used in these simulations because water and air are immiscible. Appropriate boundary conditions were set carefully for each phase. The dispersed interface, implicit formulation, and implicit body force were selected to help converge results. Others remained default. In the VOF model, the momentum equations were shared by all phases, and the volume fractions of different phases were recorded. Since the flow pattern of the water phase was what should be analyzed, water was set as the primary phase, and air is the secondary phase. The liquid zone in the bioreactor was carefully calculated and marked as in Figure 4.4. Since multiphase model was enabled, the

specific operating density (which is the density of the lightest phase, or air) should also be enabled in the operating conditions from cell zone conditions. Furthermore, the pressure in the head space of the bioreactor was assumed to be atmospheric.

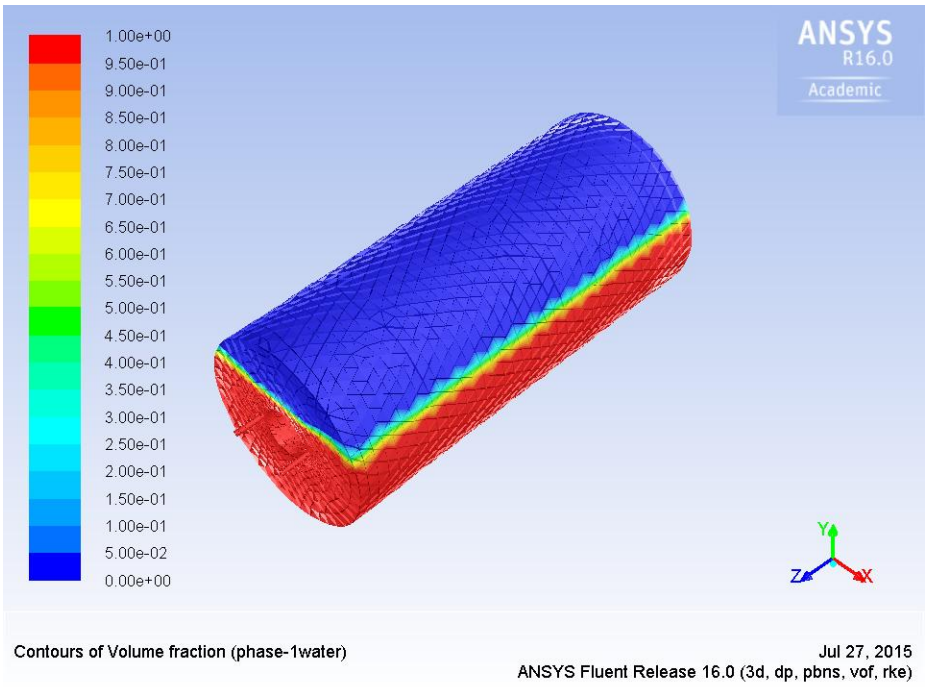

Figure 4.14. Multiphase Contours of Initial Volume Fraction (Phase 1-water @ t=0)

The moving wall of the shell and core were chosen to be rotational with selected values (4 rpm, 6 rpm, 8 rpm). Moreover, the hypothesis was made that no slip shear condition at walls. Velocity inlet was set to two inlets as boundary conditions, and pressure outlet was used to define two outlets. Specific velocity values (0.0006925975 m s^{-1}) were entered for inlets, and hydraulic diameter could be calculated as:

$$D_h = \frac{4A}{P_w} \qquad (4\text{-}43)$$

where A is the cross sectional area (m^2); P_w is the wetted perimeter (m).

The methods of SIMPLE, SIMPLEC, PISO, COUPLED are commonly seen in solution method scheme. The SIMPLE approach is the standard solver (used in this research), while the SIMPLEC approach is suitable for the uncomplicated problems (such as laminar flow with no additional models activated). The PISO method is useful for transient flow or steady-state flow with high average skewness. For transient flow (if large time step is required) and the case when the mesh is poor, the COUPLED method is applied. However, the pressure-based coupled solver is not suitable for multiphase. There are three gradient types: Green-Gauss Cell Based, Green-Gauss Node Based, Least-Square Cell Based. The Least-Square Cell Based gradient is usually the default option. Using the gradient of Green-Gauss Cell Based may lead to false diffusion. The gradient of Green-Gauss Node Based is more accurate, and minimize false diffusion, but had more computational intense. Green-Gauss Node Based gradient was enabled in this research. For VOF and mixture multiphase, only PRESTO and large body forces are available for selection in pressure formulation. On account of the existence of gravity acting on phases with large density difference, the option of large body forces was selected for pressure under spatial discretization, where forces are handled in robust numerical manner. The second order was used for other specifications for improved accuracy.

4.5. Results and Discussions

Though FLUENT will stop the calculation automatically when the convergence reached, it is still necessary to verify that the result is truly converged. The criteria for convergence is as follows: check the residuals profile and see if they reaches the pre-set requirement (for instance, for a good simulation, the residual of continuity is usually less than 10^{-4}); if a good initial guess was made, the unscaled residual could be compared with an appropriate parameter (such as mass

flow rate at inlet); when a poor initial value was used, the convergence conclusion can only be made if the residuals profile continues to decrease or remain low for a period of time (at least 50 iterations). The convergences of all the simulations showed in this research were carefully examined according to the criteria. A typical simulation in this research used several hours of wall clock time on a laptop (Intel(R) Core(TM) i704700MQ CPU @ 2.4 GHz, 8.00 GB RAM and 64-bit operating system).

In Figure 4.5, the inlets were at the left side and the outlets were at the right side. By simulating a continuous flow system, the internal flow and multiphase interactions were investigated. Generally, the simulations for multiphase fluid at different rotational velocities (4, 6, 8 rpm) showed a consistent trend, but in an increasing scale. All the velocity (m s^{-1}) profiles in Figure 4.5 were obtained for YZ plane at x=0, which was the symmetric plane of the reactor. In general, blue color was the minimum value, and red color represented the maximum value. The velocities shown in Figure 4.5 was for linear velocity, which corresponded to the rotational velocities and dimension of the bioreactor. The velocities would be expected to have gradient in radius direction despite of the same angular velocity everywhere.

The bottom of the bioreactor was filled with water. Since the rotational velocities (4, 6 and 8 rpm) and the related Reynolds numbers were small, the water in the reactor would expect to be almost stagnant, but the thin films which were adjacent to the rotating cylinders would have the velocity gradient, which were in consistent with Figure 4.5 (the majority of bottom part of the reactor was in blue color, except the rotational wall areas, for instance, shell, shafts and core). The head space was filled with air. Air is less dense and less viscous than water, hence, the rotating cylinder would have a much larger effect on the air in the head space, which explained the reason why the head space had velocity distributions as shown in Figure 4.5. Besides,

increasing the rotational velocities would act like pushing more fluids to the places which were closer to the moving walls. By comparing Figure 4.5 (a), (b) and (c) (or (d), (e) and (f); or (g), (h), and (i)), as the rotational velocities was increased, the velocity distribution located at the areas which were closer to the revolving cylinders. With comparisons between Figure 4.5 (a), (d) and (g) (or (b), (e), and (h); (c), (f), and (i)), the differences of velocity distribution between rotational outer cylinder, concurrent rotational inner and outer cylinders, and countercurrent rotational inner and outer cylinders were small, except that Figure 4.5 (a) did not have velocity in core area as a result of the stationary core, which may be more convenient to observe this phenomena from velocity vectors in Figure 4.6 (a).

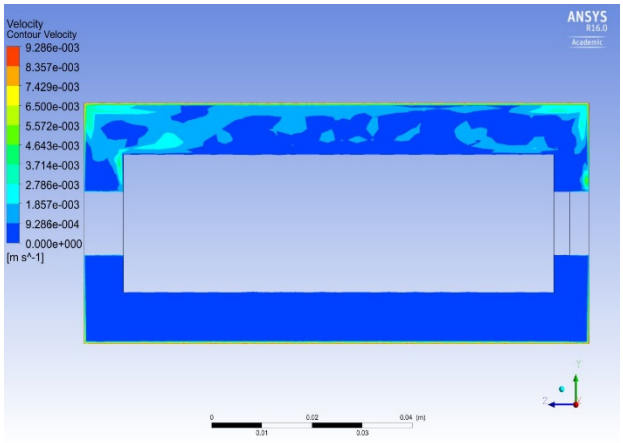

(a) Rotational Outer Cylinder at 4 rpm

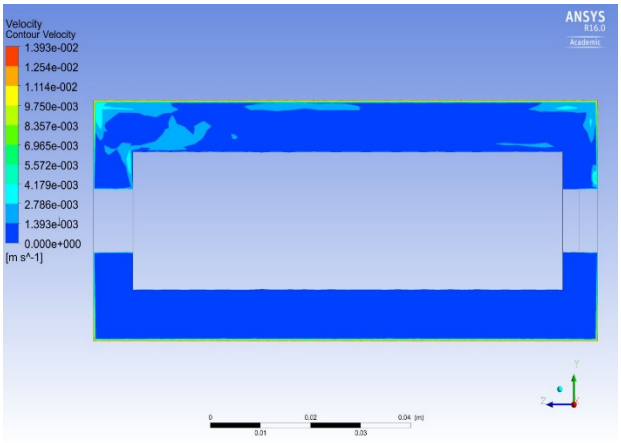

(b) Rotational Outer Cylinder at 6 rpm

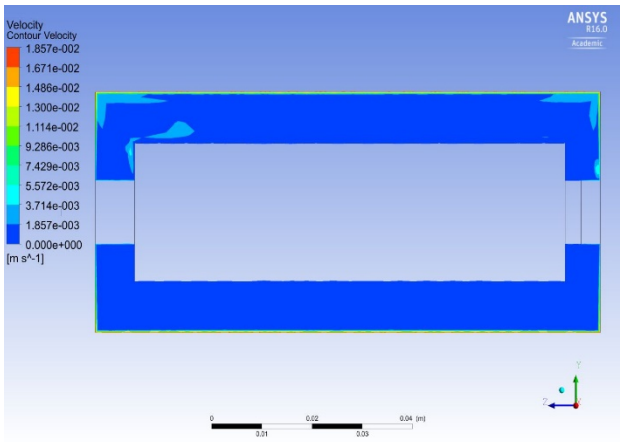

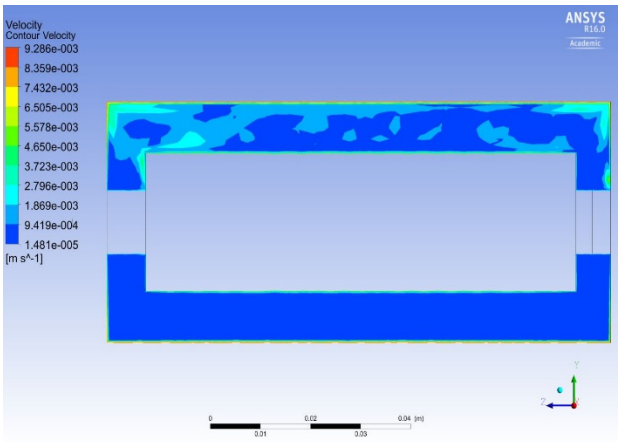

(c) Rotational Outer Cylinder at 8 rpm (d) Concurrent Rotational Inner and Outer Cylinder at 4 rpm

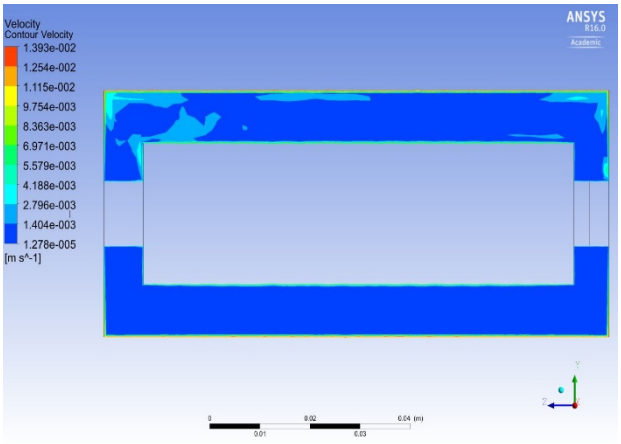

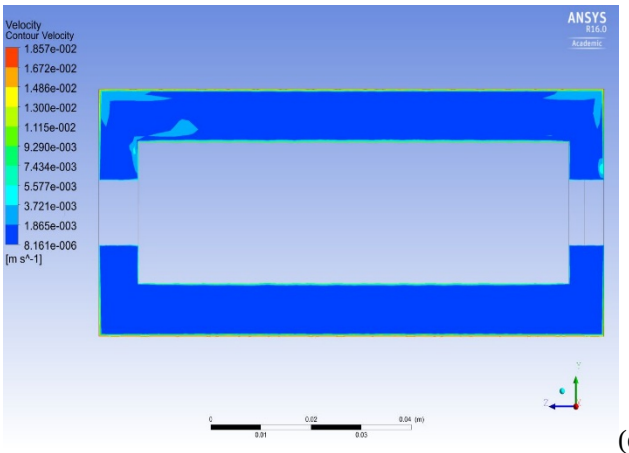

(e) Concurrent Rotational Inner and Outer Cylinder at 6 rpm (f) Concurrent Rotational Inner and Outer Cylinder at 8 rpm

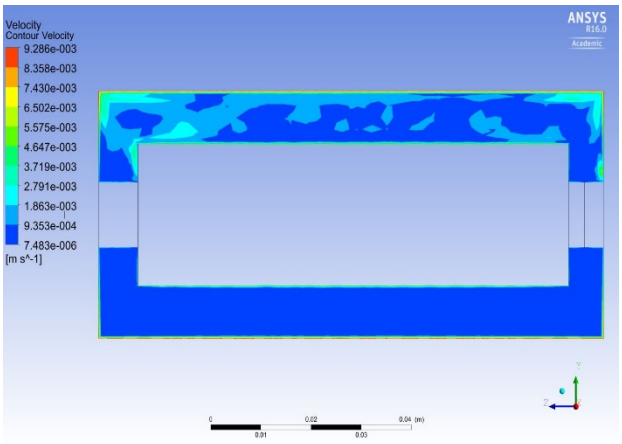

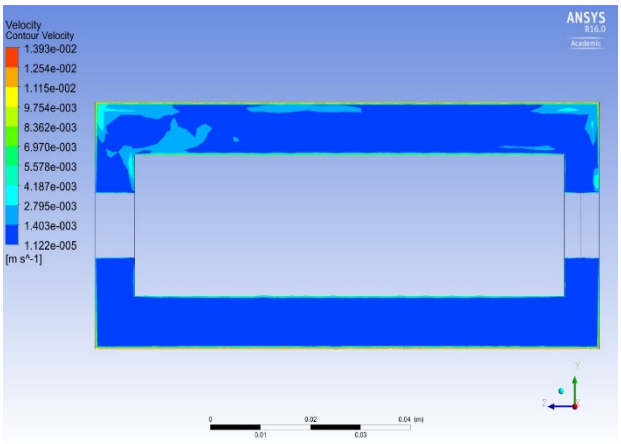

(g) Countercurrent Rotational Inner and Outer Cylinder (h) Countercurrent Rotational Inner and Outer Cylinder

at 4 rpm at 6 rpm

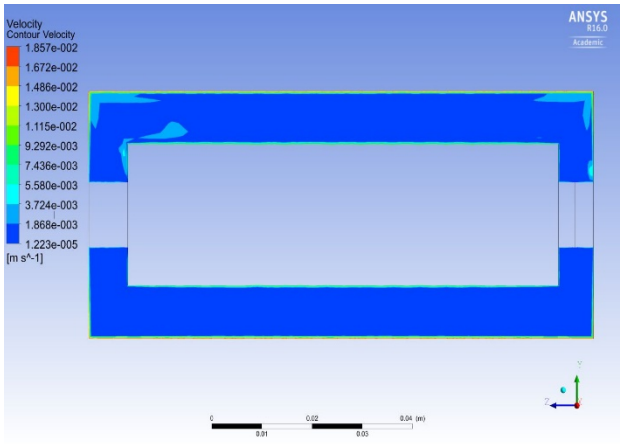

(i) Countercurrent Rotational Inner and Outer Cylinder at 8 rpm

Figure 4.15. Velocity Profiles at Various Operation Conditions (Multiple Phases (2/3 volume of fluids)

Normally, the fluids that close to a moving plane are inclined to have the same or about the same velocity as the plane; this is called the no-slip condition. From the velocity vectors (m s^{-1}) of the fluids in Figure 4.6 (a) to (c), the maximum velocity occurred at the wall of the outer cylinder and had the same value as the outer cylinder (indicated by the red color), while the minimum velocity occurred at the wall of the core cylinder and had the value of 0 (represented in blue). In contrast, it was obvious to see that the velocity of fluids near the core areas was nonzero from Figure 4.6 (d) to (i) due to the rotational core and core shaft at given values, which was marked in yellow color. Figure 4.6 (a) to (c) (or (d) to (f); (g) to (i)) showed a consistent and increasing trend. There is no major difference of velocity profiles upon different rotational velocity. The minor difference of velocity profiles and velocity vectors under different operating conditions may be due to the low rotational velocities of the system and small difference between rotational velocities, which resulted in an almost stationary and low shear system. Both from Figure 4.5 and Figure 4.6, the inlet velocity did not have large effects on the overall

velocity profile (or the flow patterns), which may ascribed to that the inlet velocity (0.0006926 m s^{-1}) was small comparing to the rotational velocities. It has been investigated that inlet velocity (larger than 0.001 m s^{-1}) did have influence on the fluid patterns of this system under current operating rotational velocity (less than 8 rpm). Consequently, instead of inducing problems to the system, the small velocity inlet provided a good approach to medium addition.

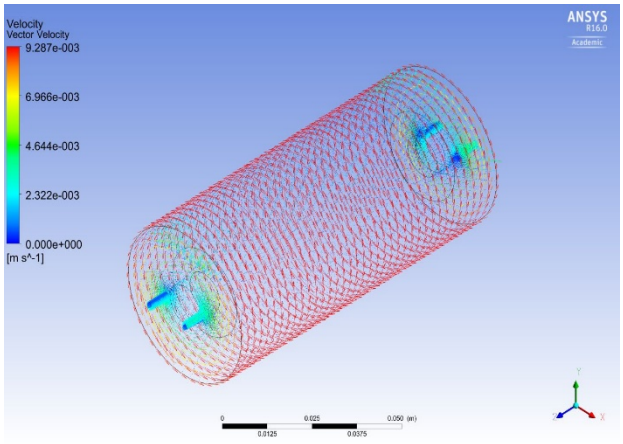

(a) Rotational Outer Cylinder at 4 rpm

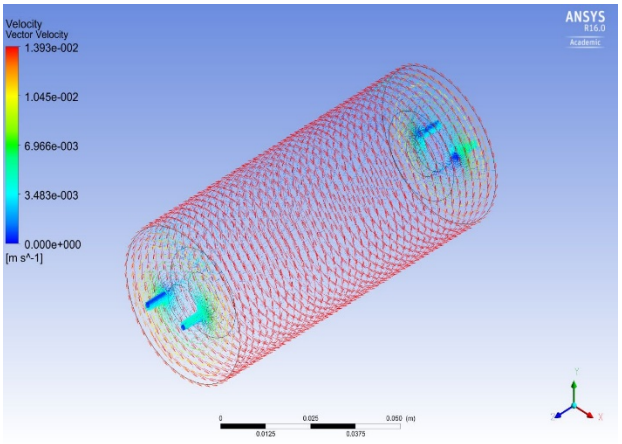

(b) Rotational Outer Cylinder at 6 rpm

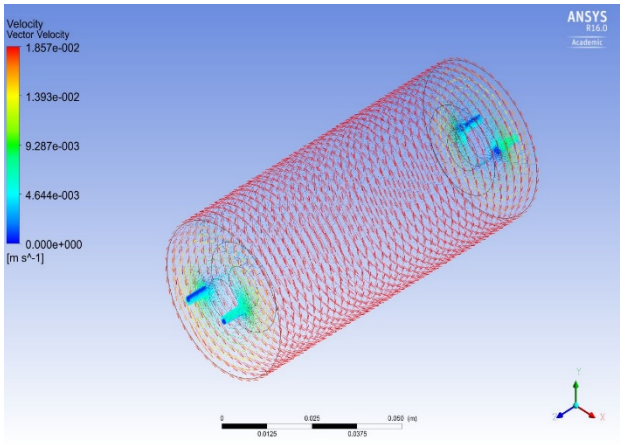

(c) Rotational Outer Cylinder at 8 rpm

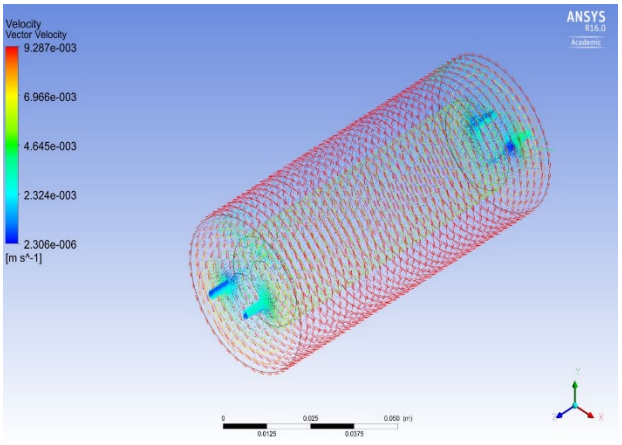

(d) Concurrent Rotational Inner and Outer Cylinder at 4 rpm

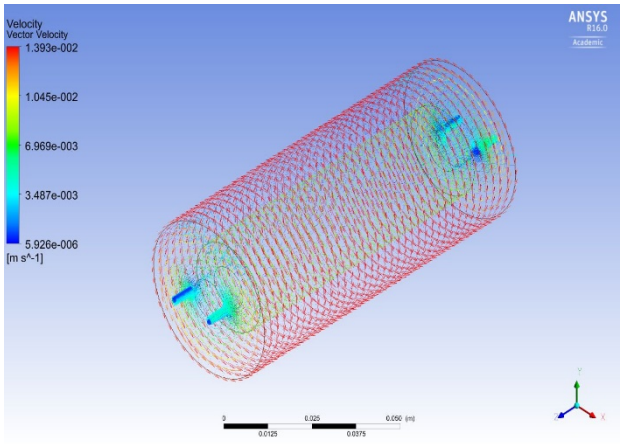

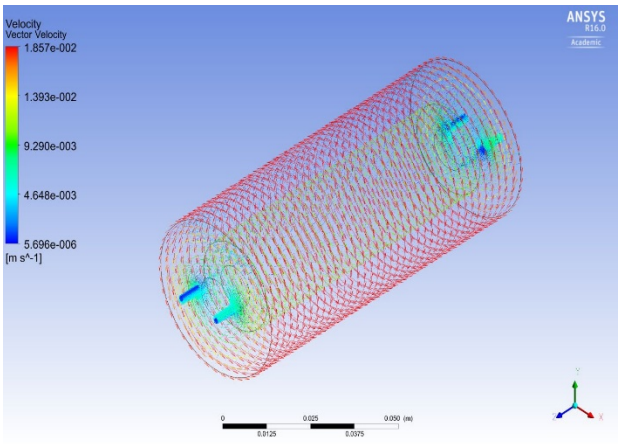

(e) Concurrent Rotational Inner and Outer Cylinder at 6 rpm (f) Concurrent Rotational Inner and Outer Cylinder at 8 rpm

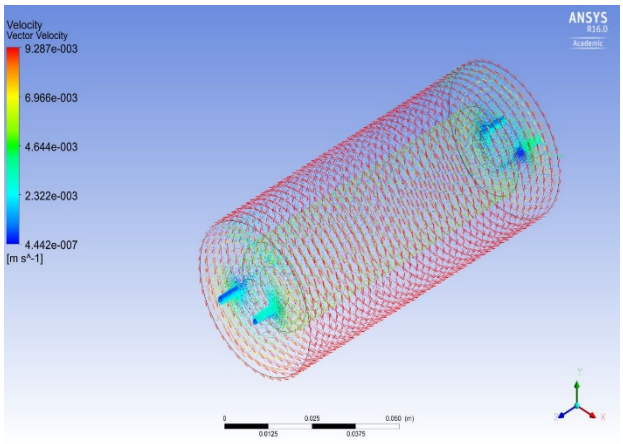

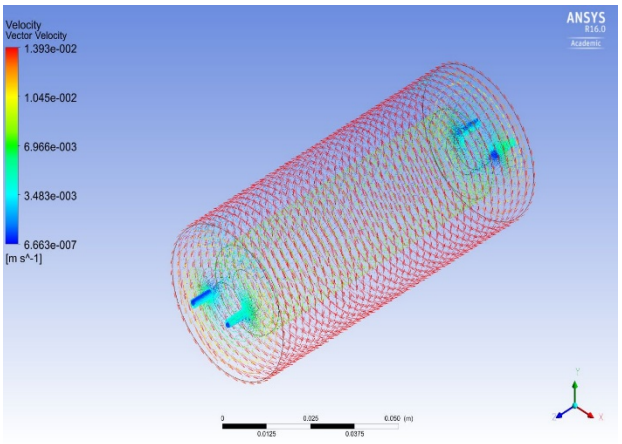

(g) Countercurrent Rotational Inner and Outer Cylinder at 4 rpm (h) Countercurrent Rotational Inner and Outer Cylinder at 6 rpm

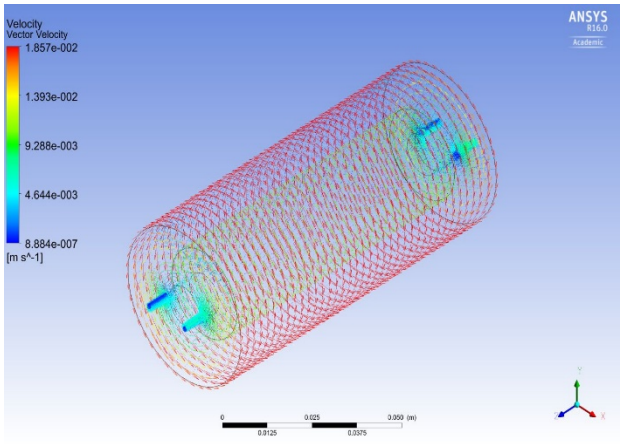

(i) Countercurrent Rotational Inner and Outer Cylinder at 8 rpm

Figure 4.16. Velocity Vectors at Various Operation Conditions (Multiple Phases (2/3 volume of fluids)

Shear stress is one of the key factors to cell lines. Generally, the damage of shear stress resulting from turbulent flow is more severe than that from laminar flow (Chisti, 2001). To inhibit the activation of human cervical carcinoma HeLaS3 and mouse abdominal fibroblast L929 in the environment of turbulent flow through stainless steel capillaries, Augenstein et al. (1971) concluded that the average wall shear stress of (0.1-2.0) x 10^3 N m^{-2} should be achieved. Leukocytes could be sheared away from the vascular endothelium by shear stress at a range of 26.5 and 106 N m^{-2} in the rabbit omentum (Schmid-schoenbein et al., 1975). McQueen et al. (1987) observed that a threshold average wall shear stress of 180 N m^{-2} would commence the lysis of suspended mouse myeloma line in turbulent capillary flow. The biochemical response of human T cells to the lectin phytohemagglutinin-P (PHA-P) would be affected when the shear stress was 10 to 20 N m^{-2} over 10 minutes (Chittur et al., 1988). For erythrocytes in tube flow (3-mm tube and whole blood), hemolysis would occur in the entrance with the shear stress of 4000 N m^{-2} (Blackshear and Blackshear, 1987), which was in agreement with the conclusion from Bernstein et al. (1967) that the critical shear stress for the lysis of erythrocytes in turbulent jet was measure as 6000 N m^{-2} for brief exposures (around 10^{-5} s). For hybridoma cells sheared in a coaxial cylinder Searle viscometer, a shear stress level of over 5 Pa in turbulent regime would damage cells over third fourths exposure hour (Abu-Reesh and Kargi, 1989). A rapid decrease in cytosolic pH of rat aortic endothelial cells cultured in glass capillary tubes resulted from laminar shear stress (1.34 N m^{-2} of shear stress led to the maximal effect 0.09 pH unit) (Ziegelstein et al., 1992).

Figure 4.7 were the images of wall shear stress (Pa) of the outer cylinder. Similarly, the blue color means the minimum value and the red color represents the maximum value. Two thirds of the bioreactor was filled with water. In other words, as shown in Figure 4.7, the top part was air and the bottom part was water. The main shear stress occurred at the rotational shell wall (the water phase) and in the inlet and outlet area where the flow contacts with the wall. Additionally, the shear stress for the outer cylinder only associated with the rotational outer cylinder, which mean the shear stress for the outer cylinder profile would be the same for the same rotational rate of the outer cylinder, no matter how and what speed the inner cylinder rotated. The shear from air was negligible, so the top area has the blue color. The major shear stress would occur in the bottom part or the water phase. As could be concluded from Figure 4.7, the shear stress increased with increasing rotational velocities. Even the maximum shear stress appeared in this system was far more less than the average shear stress that would inhibit the behavior of a plethora of cell lines, which provided the evidence of good performance of this bioreactor in future cell cultivation. The viscosity of water is 8.9×10^{-4} Pa, which was smaller than the viscosity of the mixture of cell lines and medium. Though the shear stress predicted in this research was using water as the fluid, the order of magnitude of the shear stress was 10^{-1} as from Figure 4.7, which was very small. Thus, it could still be anticipated that the shear stress in this bioreactor using the accurate viscosity would still be a small value.

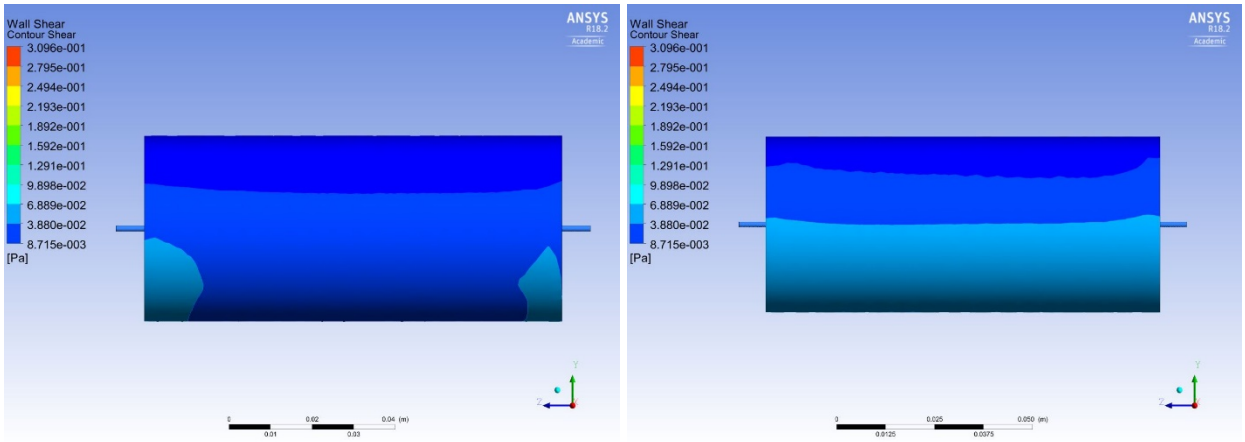

(a) Rotational Cylinder at 4 rpm

(b) Rotational Cylinder at 6 rpm

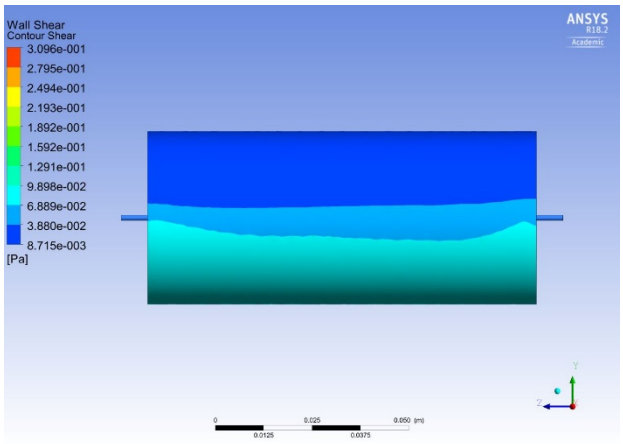

(c) Rotational Cylinder at 8 rpm

Figure 4.17. Wall Shear Stress of Outer Cylinder at Various Operation Conditions (Multiple Phases (2/3 volume of fluids)

Basically, the shear stress was normally caused by the velocity gradient. As the core and the core shaft were stationary in Figure 4.8 (a) to (c), it would be expected that low shear stress occur in these two areas. In Figure 4.8 (a) to (c), the shear stress that occurred in the right part of the inner cylinder was caused by the combination effect from the inlet flow and the rotation of hub part (in the same direction as the shell shaft). Similarly, since the shell shaft was rotating at the controlled velocities, the shear stress would also occur in the shell shaft area or the left part

of the inner cylinder. From Figure 4.7 (d) to (i), the shear stress also occurred in the core area because of the rotation. As the top was filled with air, the shear stress on the top part of the core was negligible as in Figure (d) to (i). Besides, the shear stress distribution on the core provided the shape of free surface of the fluids between the revolving cylinders.

However, the distribution of shear stress on the core seemed to be independent of the rotational directions, as comparing Figure 4.7 (e) and (h). Moreover, the maximum shear stress still appeared in the area where the inlet flow first contacted the system (or the hub part of the inner cylinder) and the outlet flow exited the system (or the shell shaft part). In other words, the value of the maximum shear stress on the core did not depend on whether the core was gyrating or not as comparing Figure 4.7 (b), (e) and (h). In Figure 4.7 (g), (h) and (i), the discontinuity of the shear stress profile in the right part of the inner cylinder resulted from the countercurrent rotating of hub part and core shaft. From Figure 4.5 and 4.8, the conclusion may be obtained that the rotating of the outer cylinder had a larger effect on the wall shear stress and velocity spread than the spinning of the inner cylinder under low rotational velocities.

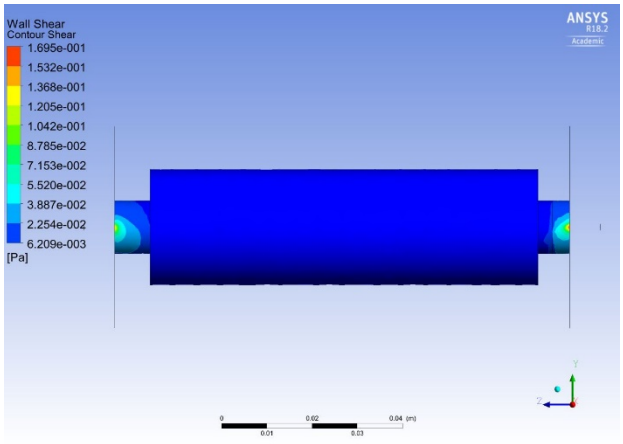

(a) Rotational Outer Cylinder at 4 rpm

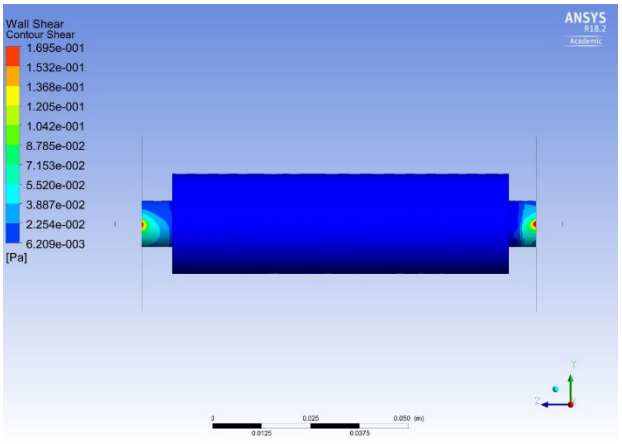

(b) Rotational Outer Cylinder at 6 rpm

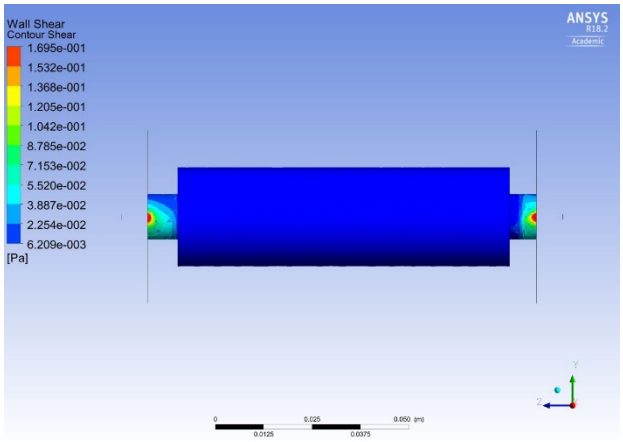

(c) Rotational Outer Cylinder at 8 rpm

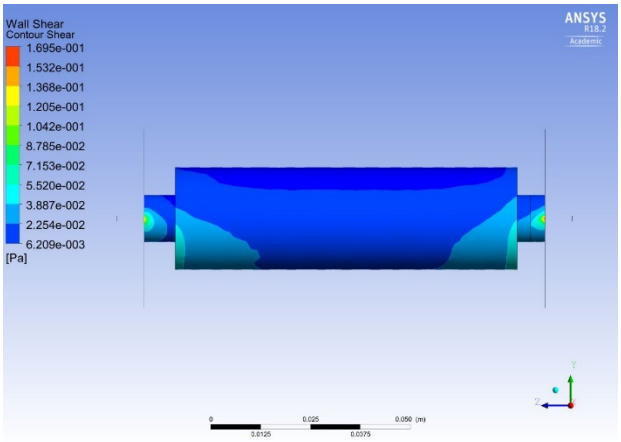

(d) Concurrent Rotational Inner and Outer Cylinder at 4 rpm

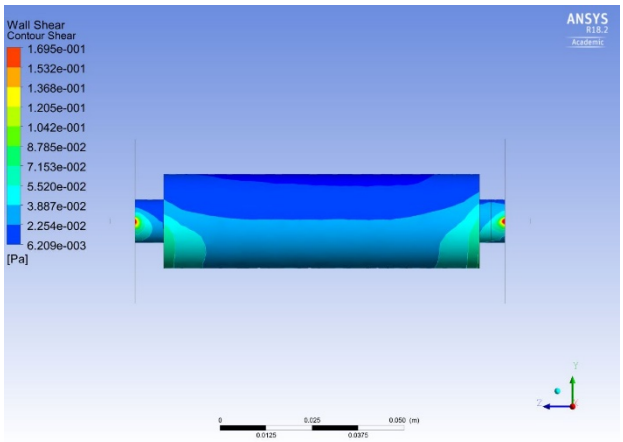

(e) Concurrent Rotational Inner and Outer Cylinder at 6 rpm

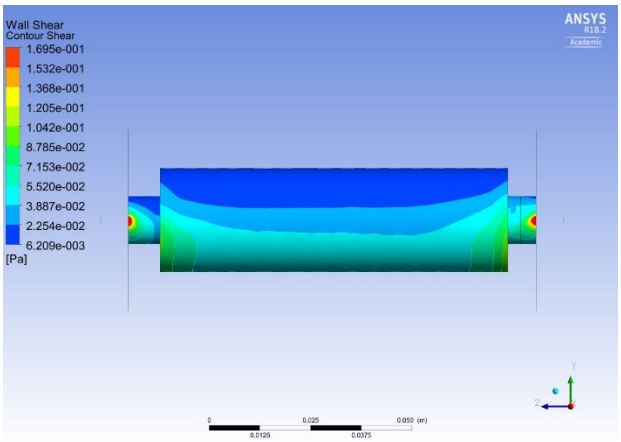

(f) Concurrent Rotational Inner and Outer Cylinder at 8 rpm

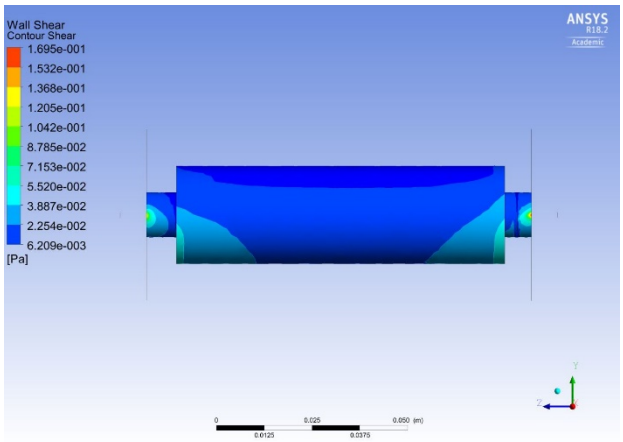

(g) Countercurrent Rotational Inner and Outer Cylinder at 4 rpm

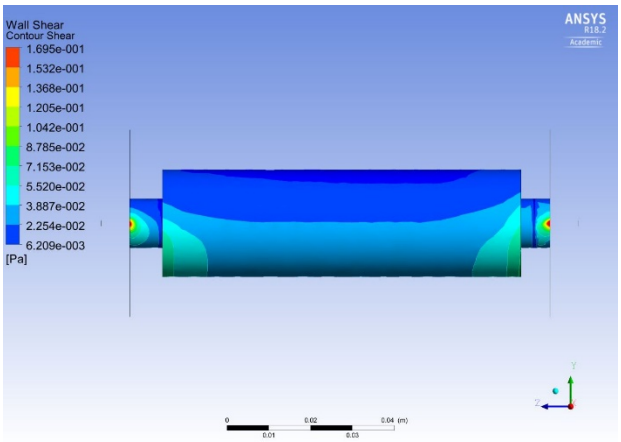

(h) Countercurrent Rotational Inner and Outer Cylinder at 6 rpm

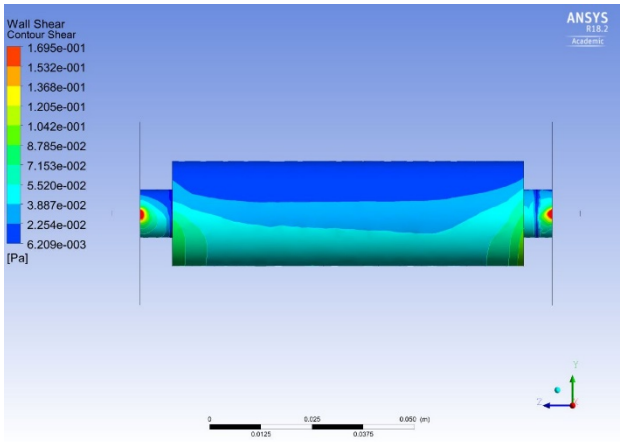

(i) Countercurrent Rotational Inner and Outer Cylinder at 8 rpm

Figure 4.18. Wall Shear Stress of Inner Cylinders at Various Operation Conditions (Multiple Phases (2/3 volume of fluids)

From Figure 4.9 (a), it could be concluded that the average wall shear stress of this bioreactor was small (in the order of 10^{-1}), and the rotation of the inner cylinder did increase the average wall shear stress of the system as expected, however, the average wall shear stress did not differ much on the rotational direction of the inner cylinders at low rotational velocities (less than 8 rpm). The maximum wall shear stress in this bioreactor at 8 RPM was 0.02 Pa, which was far less than the critical shear stress that could damages to most of cells, even the shear sensitive cell line hybridoma (critical shear stress of 5 Pa). As described previously, the eddy viscosity or the turbulent viscosity in the transfer momentum caused by turbulent eddies was analogues to the molecular viscosity in the laminar flow. The rotation of the inner cylinders would increase the turbulence level, as could also be observed from Figure 4.9 (b) and Figure 4.10, the maximum eddy viscosity of the system under the condition of rotational inner cylinders was slightly higher than that with stationary inner cylinders. It was found from Figure 4.10 that the main eddy viscosity distribution took place in the water phase (the bottom part), which could also be predicted from Equation 4.7 (as from Equation 4.7, the eddy viscosity depends on the turbulence

kinetic energy (k), turbulence eddy dissipation rate (ε) and shear stress). Nevertheless, from Figure 4.9 (a), the profiles for the concurrent and the countercurrent rotation of the inner cylinders overlapped, which showed that the rotating direction of inner cylinders did not affect the maximum value and the spread of the eddy viscosity significantly (for example, comparing Figure 4.10 (f) and (i)) when rotational speed was low.

The maximum turbulence kinetic energy per unit mass (k, J kg^{-1}) appeared at the outer cylinder area for the reason that the area near outer cylinder had the maximum linear velocity though the rotational velocity of the system was constant, which was in agreement with the observation from Figure 4.11. The distribution of the turbulence kinetic energy was closely associated with the velocity distribution (in Figure 4.5), in a way that the spread of the turbulence kinetic energy also was prone to be more adjacent to the outer cylinder with increasing rotational speed. The dissipation rate (ε, J kg^{-1} s^{-1} or m^2 s^{-3}) is the rate of resistant work done by the fluctuating viscous stresses to deformation of the fluids by strain rates, and only acts as the reduction to the kinetic energy of the flow. As from Figure 4.12, the maximum energy dissipated at the area near the outer cylinder and did not depend on the rotation of the inner cylinders (Figure 4.12 (b), (e) and (h)), which is reasonable considering the maximum kinetic energy also occurred here. Furthermore, the overlapping of the lines (Figure 4.9 (c) and (d)) under various operating situations verified that the rotation of inner cylinders impact the maximum value of kinetic energy and energy dissipation rate slightly. The rotation of inner cylinders led to the appearance of the turbulence kinetic energy, eddy dissipation rate near the inner cylinders. In summary, the value of average shear stress, maximum eddy viscosity, maximum turbulence kinetic energy and maximum turbulence dissipation rate are positively proportional to the rotational velocity.

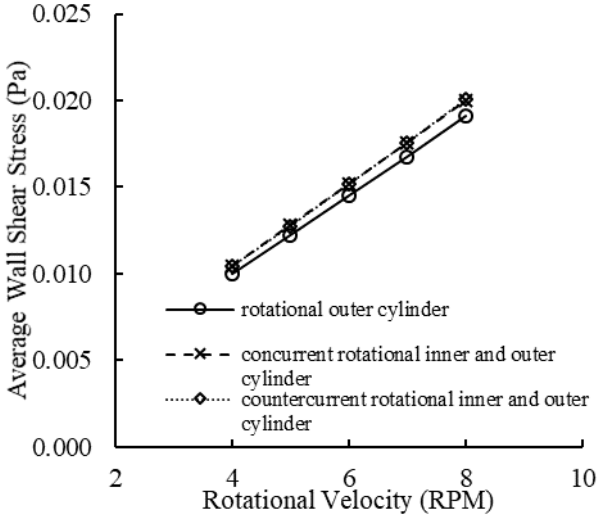

(a) Average Shear Stress versus Rotational Velocity

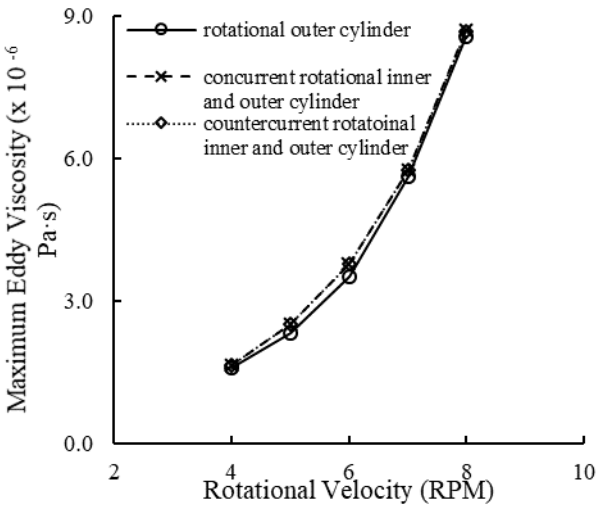

(b) Maximum Eddy Viscosity versus Rotational Velocity

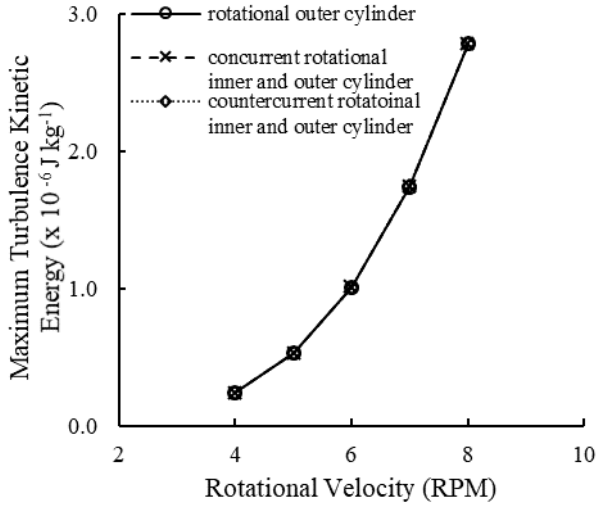

(c) Maximum Turbulence Kinetic Energy versus Rotational Velocity

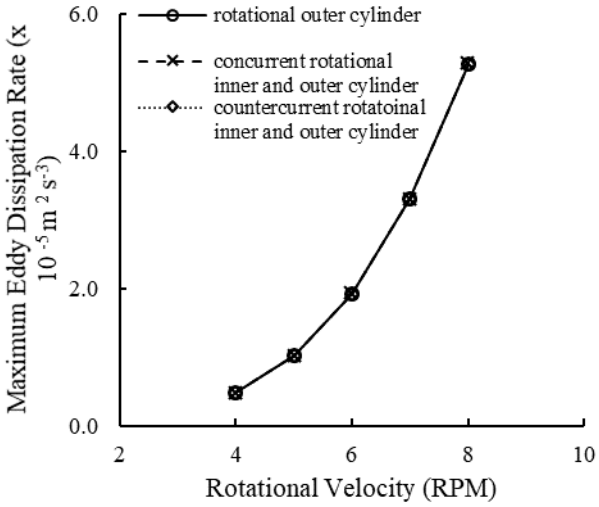

(d) Maximum Eddy Dissipation Rate versus Rotational Velocity

Figure 4.19. Other Parameters versus Rotational Velocity

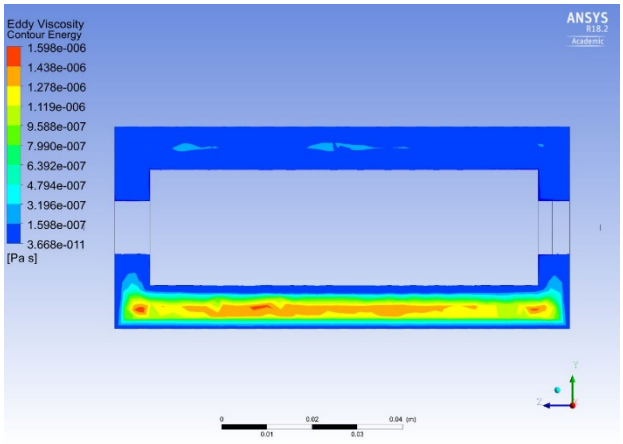

(a) Rotational Outer Cylinder at 4 rpm

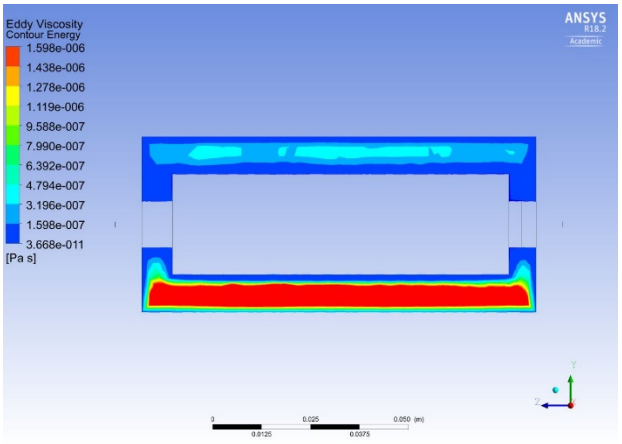

(b) Rotational Outer Cylinder at 6 rpm

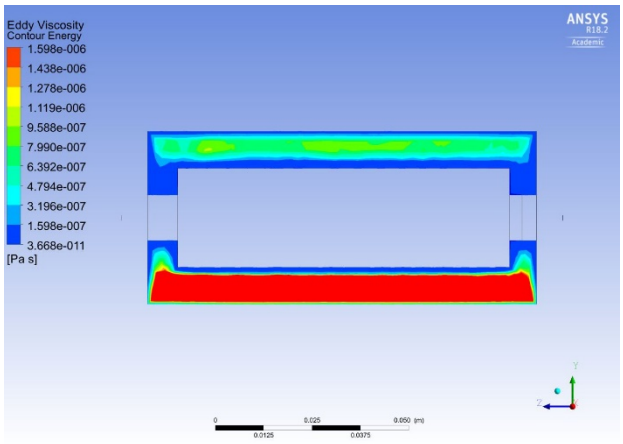

(c) Rotational Outer Cylinder at 8 rpm

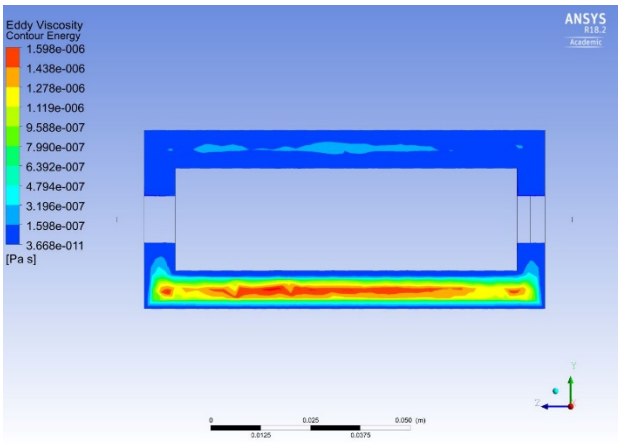

(d) Concurrent Rotational Inner and Outer Cylinder at 4 rpm

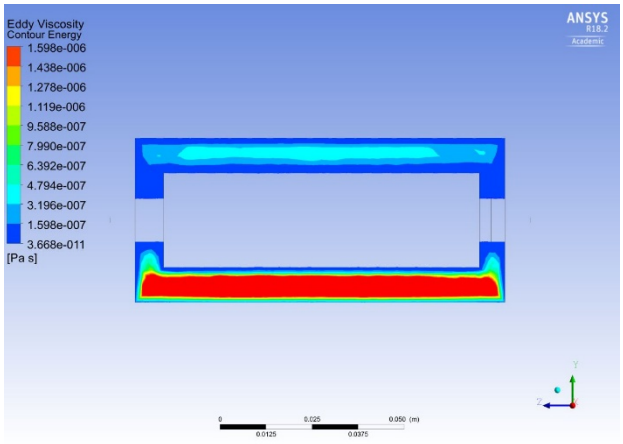

(e) Concurrent Rotational Inner and Outer Cylinder at 6 rpm

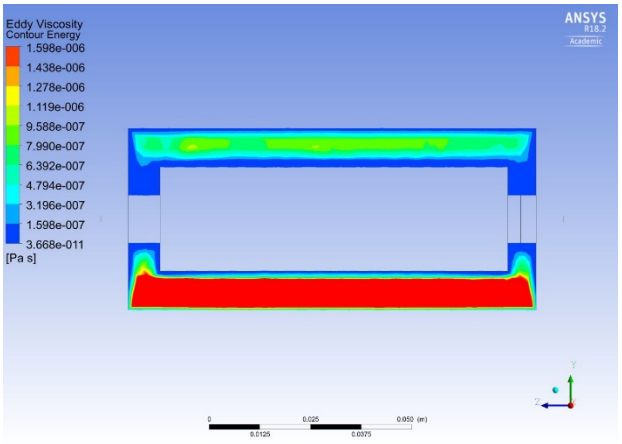

(f) Concurrent Rotational Inner and Outer Cylinder at 8 rpm

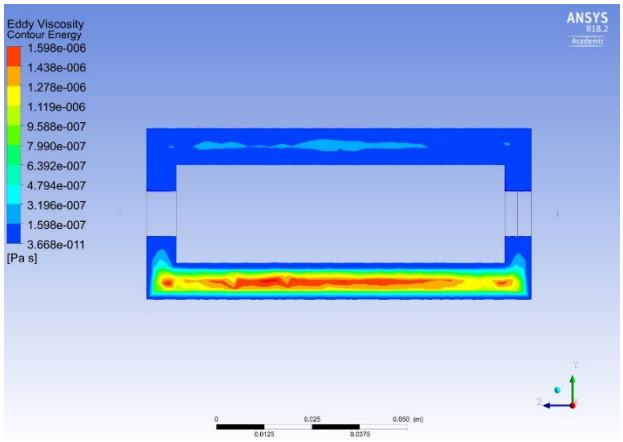

(g) Countercurrent Rotational Inner and Outer Cylinder at 4 rpm

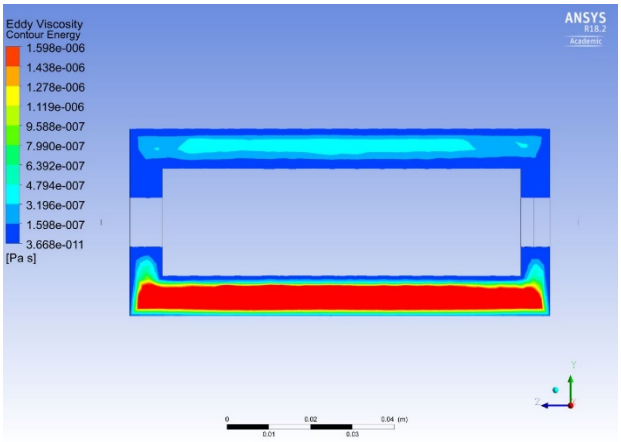

(h) Countercurrent Rotational Inner and Outer Cylinder at 6 rpm

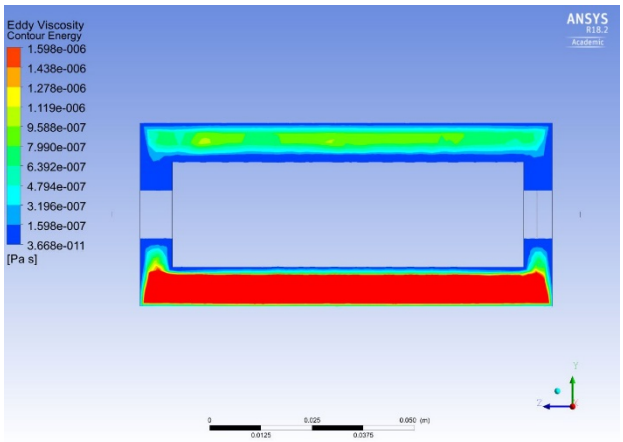

(i) Countercurrent Rotational Inner and Outer Cylinder at 8 rpm

Figure 4.20. Eddy Viscosity at Various Operation Conditions (Multiple Phases (2/3 volume of fluids)

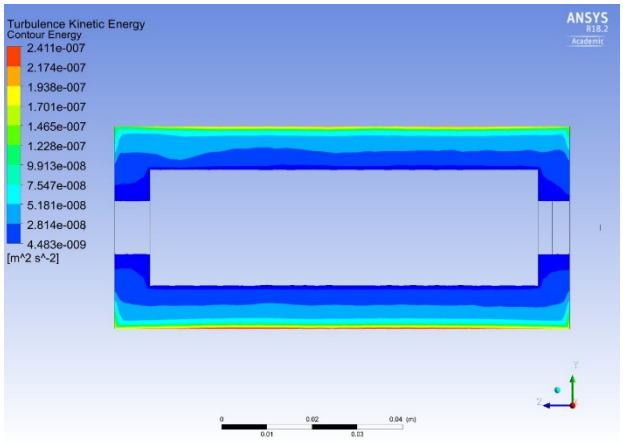

(a) Rotational Outer Cylinder at 4 rpm

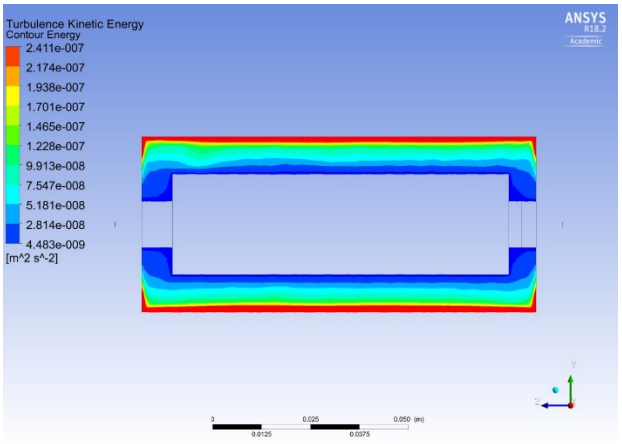

(b) Rotational Outer Cylinder at 6 rpm

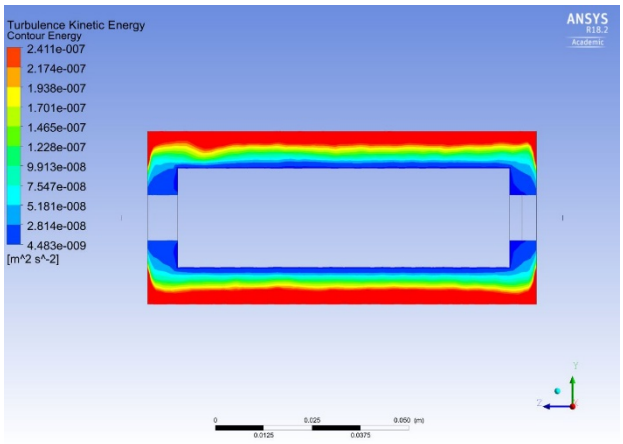

(c) Rotational Outer Cylinder at 8 rpm

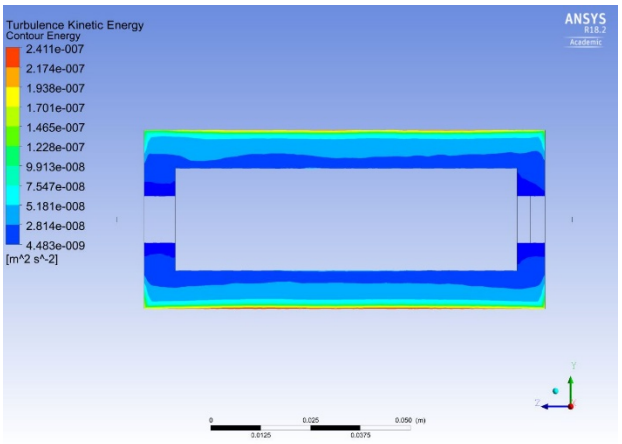

(d) Concurrent Rotational Inner and Outer Cylinder at 4 rpm

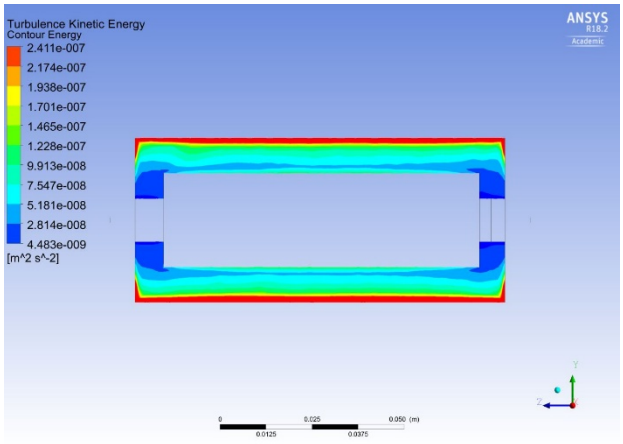

(e) Concurrent Rotational Inner and Outer Cylinder at 6 rpm

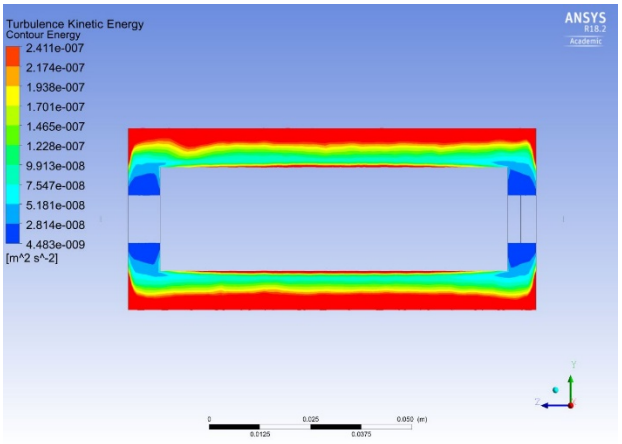

(f) Concurrent Rotational Inner and Outer Cylinder at 8 rpm

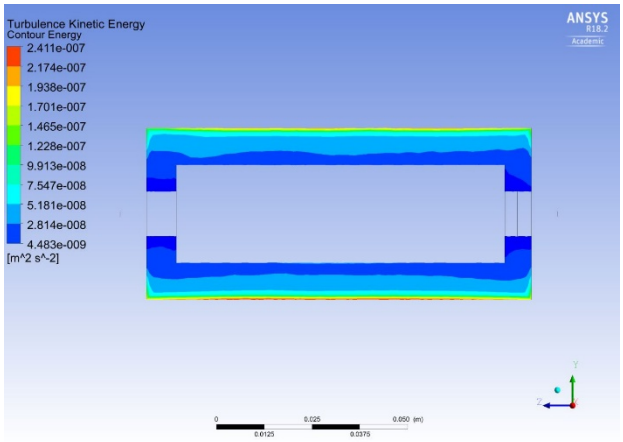

(g) Countercurrent Rotational Inner and Outer Cylinder at 4 rpm

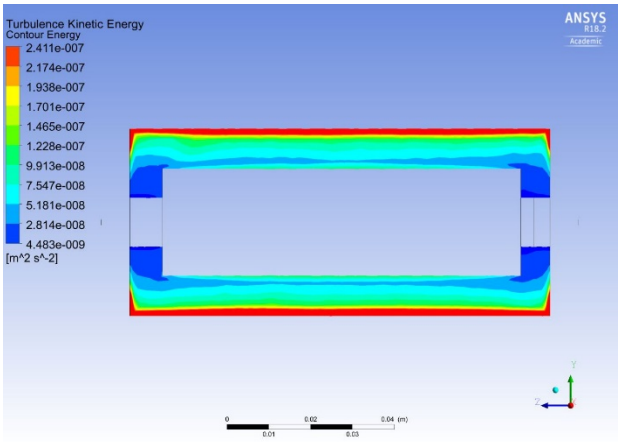

(h) Countercurrent Rotational Inner and Outer Cylinder at 6 rpm

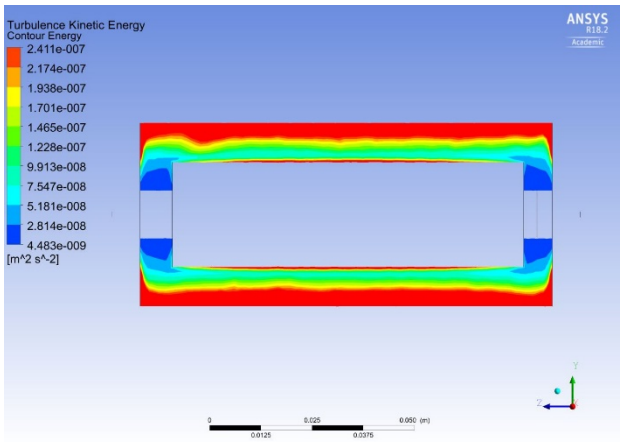

(i) Countercurrent Rotational Inner and Outer Cylinder at 8 rpm

Figure 4.21. Turbulence Kinetic Energy per Unit Mass at Various Operation Conditions (Multiple Phases (2/3 volume of fluids)

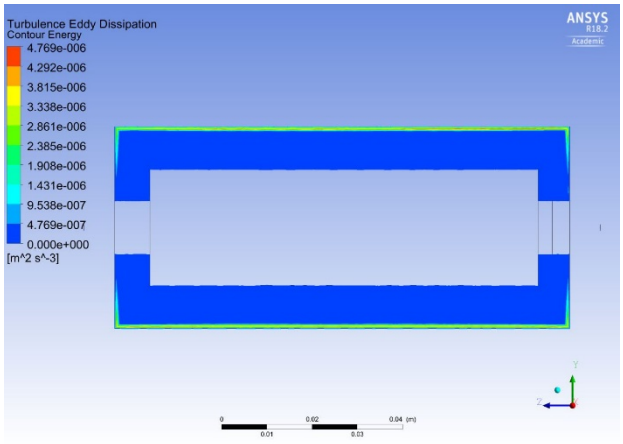

(a) Rotational Outer Cylinder at 4 rpm

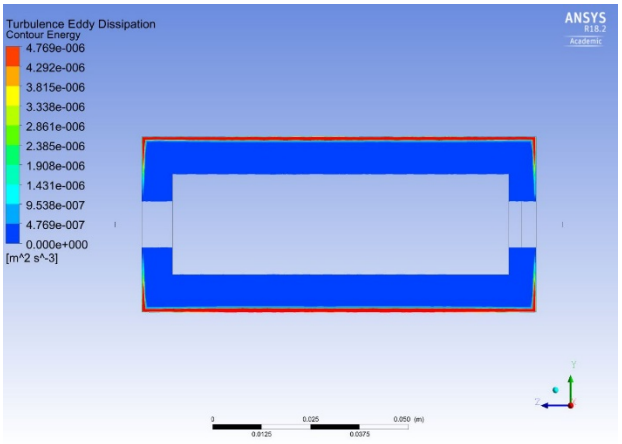

(b) Rotational Outer Cylinder at 6 rpm

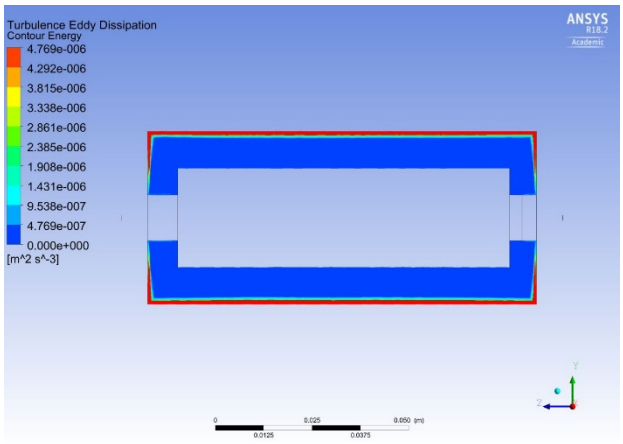

(c) Rotational Outer Cylinder at 8 rpm

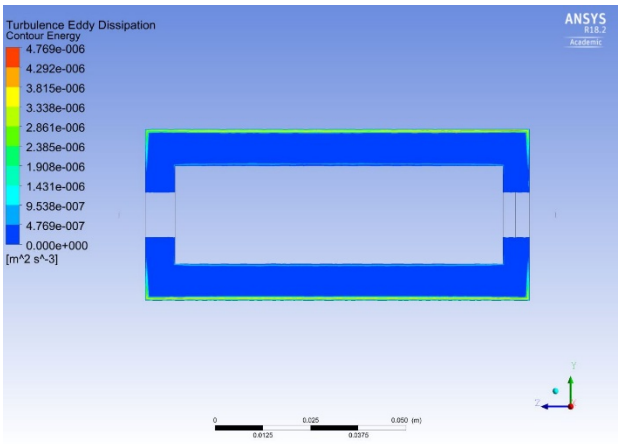

(d) Concurrent Rotational Inner and Outer Cylinder at 4 rpm

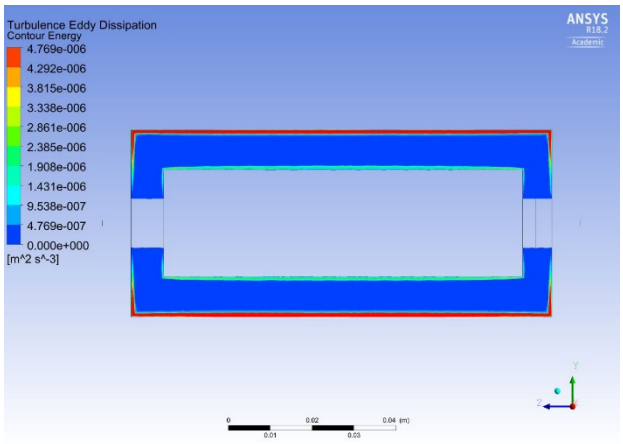

(e) Concurrent Rotational Inner and Outer Cylinder at 6 rpm

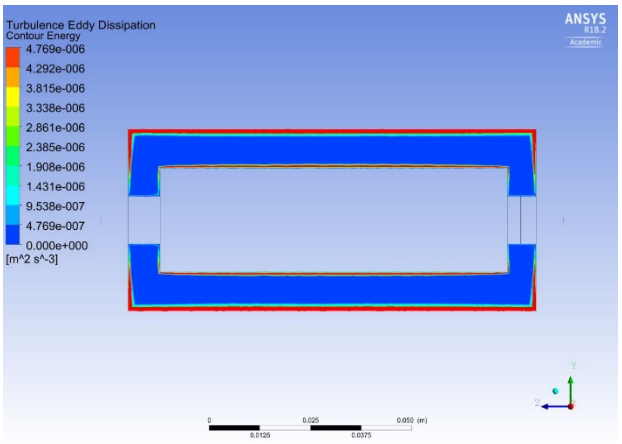

(f) Concurrent Rotational Inner and Outer Cylinder at 8 rpm

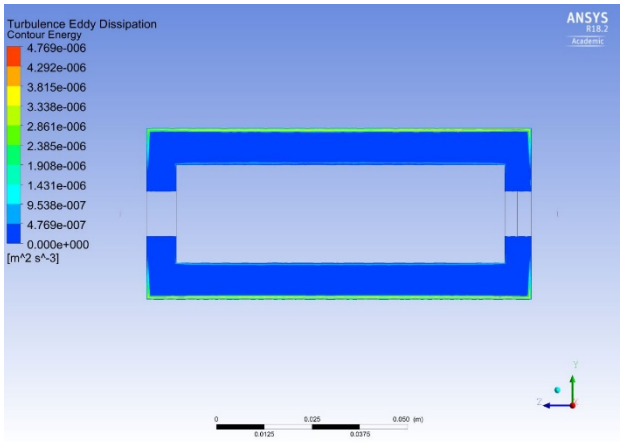

(g) Countercurrent Rotational Inner and Outer Cylinder at 4 rpm

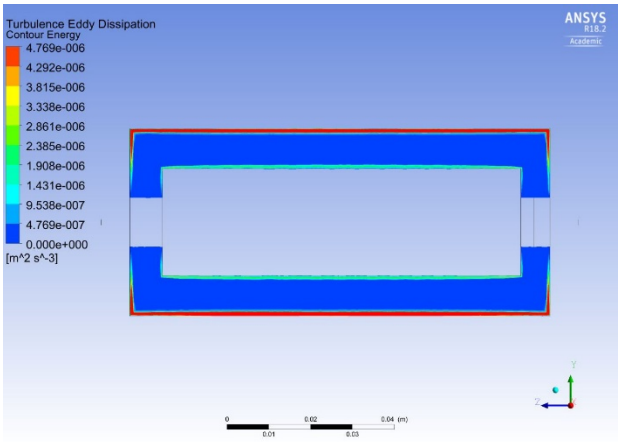

(h) Countercurrent Rotational Inner and Outer Cylinder at 6 rpm

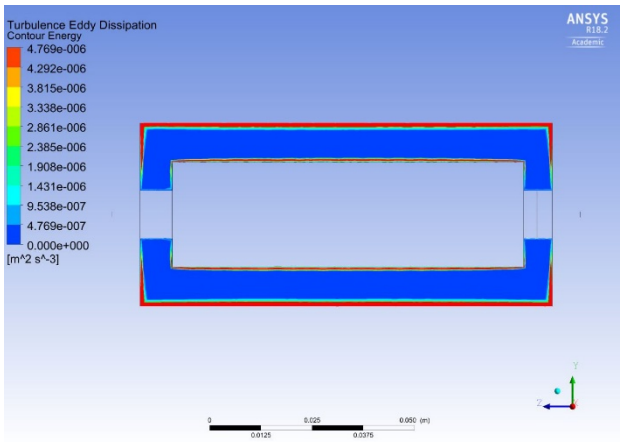

(i) Countercurrent Rotational Inner and Outer Cylinder at 8 rpm

Figure 4.22. Turbulence Eddy Dissipation Rate per Unit Mass at Various Operation Conditions (Multiple Phases (2/3 volume of fluids)

As a rule, streamlines are normally defined as tangent curves to the velocity vector of the flow. Figure 4.13 showed the velocity streamline starting from the inlets to the whole system, which displays a good image of how the fluids flow in the system taking account of the rotational outer and inner cylinders with different rate. From Figure 4.13 (a) to (c) (or (d) to (f); (g) to (i)), the range of the streamlines expanded more through the bioreactor with larger rotating speed, which could be explained by that larger portion of inlet flows were prone to be

transported by the rotating of cylinders (outer and inner) the rotational speed increased (because the centrifugal force was increased), resulting in better mixing outcome. Comparing Figure 4.13 (a) with (d), the fluids flow patterns seemed to expand to a larger area in (d) (concurrent rotation) than that in (a) (stationary inner cylinders), owing to that the revolving of the inner cylinders also contributed to the transportation of the fluids. Moreover, the contrast between Figure 4.13 (d) and (g), (d) (concurrent rotation) still had a more expansive flow area than (g) (countercurrent rotation). It could be summarized from Figure 4.13 that the concurrent rotation method may provide best mixing results as the velocity streamline expanded more in condition of concurrent rotation.

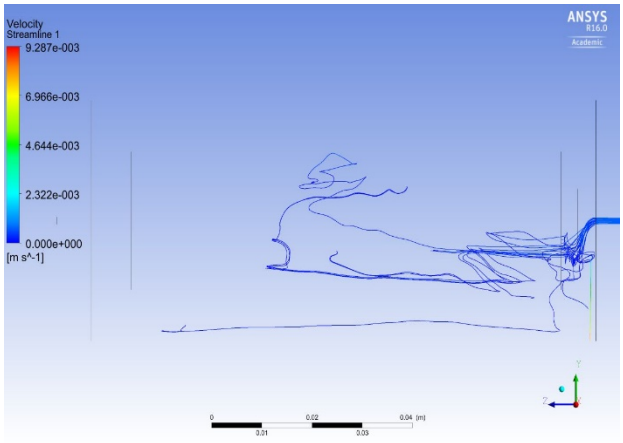

(a) Rotational Outer Cylinder at 4 rpm

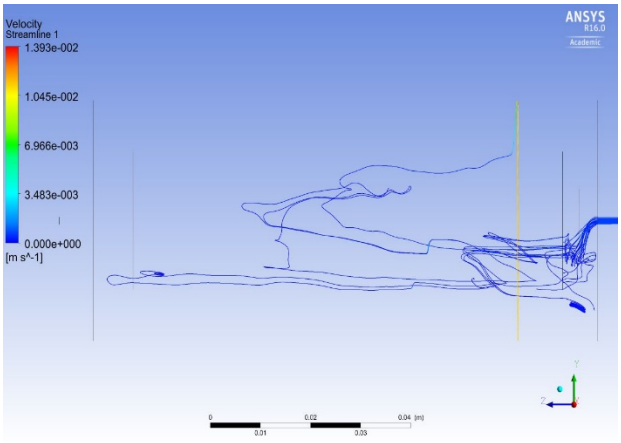

(b) Rotational Outer Cylinder at 6 rpm

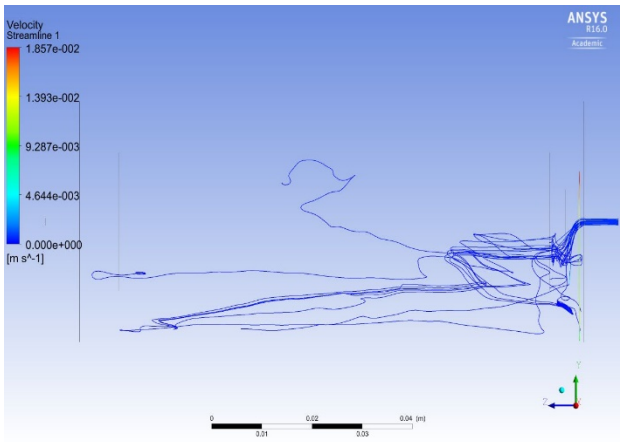

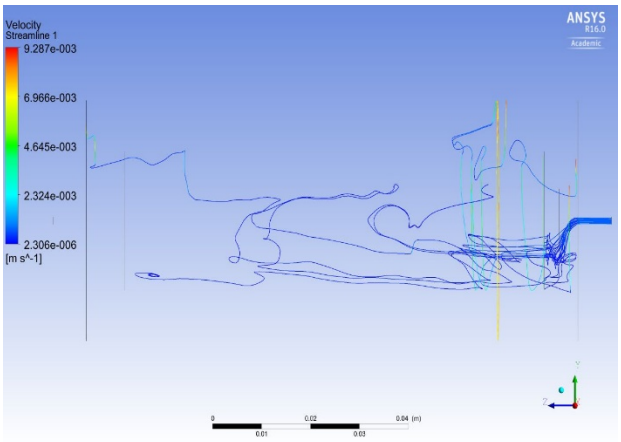

(c) Rotational Outer Cylinder at 8 rpm

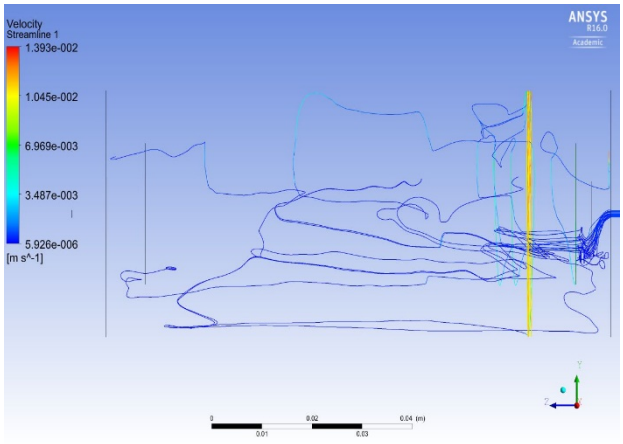

(d) Concurrent Rotational Inner/Outer Cylinder at 4 rpm

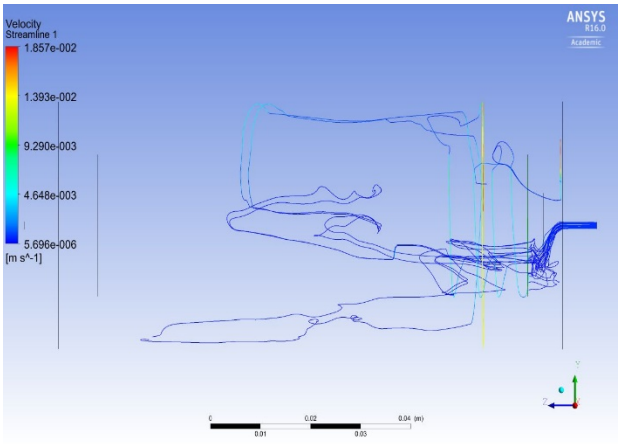

(e) Concurrent Rotational Inner/Outer Cylinder at 6 rpm

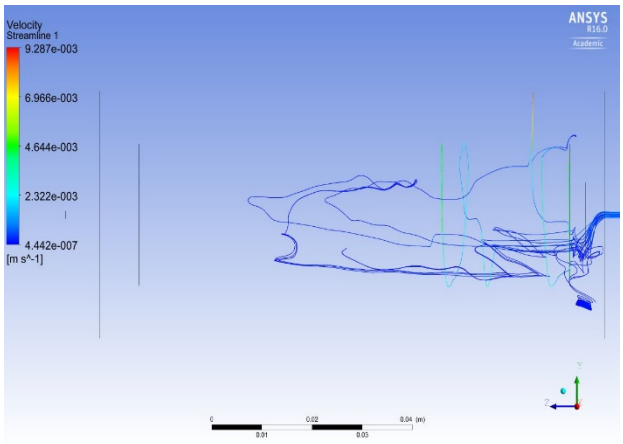

(f) Concurrent Rotational Inner/Outer Cylinder at 8 rpm

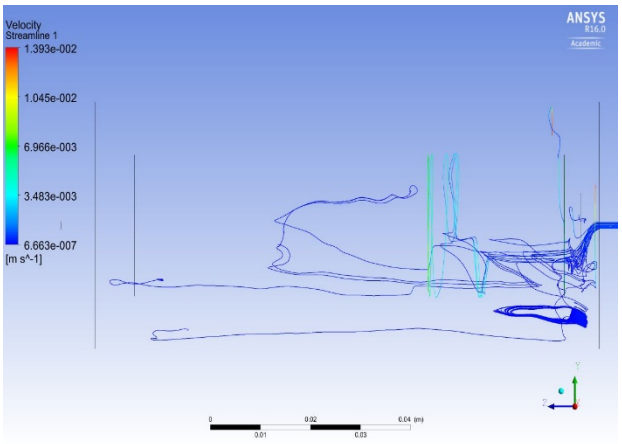

(g) Countercurrent Rotational Inner and Outer Cylinder at 4 rpm

(h) Countercurrent Rotational Inner and Outer Cylinder at 6 rpm

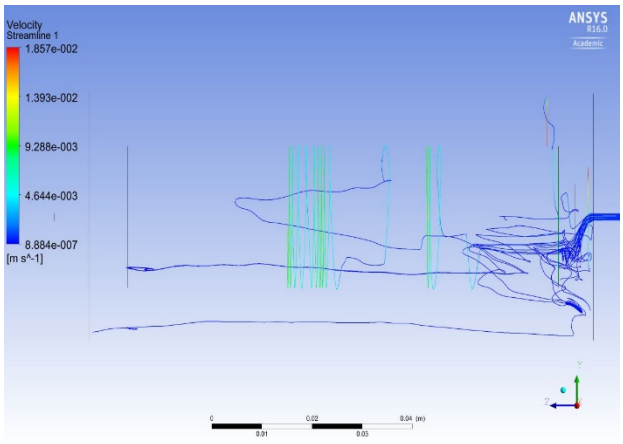

(i) Countercurrent Rotational Inner and Outer Cylinder at 8 rpm

Figure 4.23. Velocity Streamlines from Inlets at Various Operation Conditions (Multiple Phases (2/3 volume of fluids)

4.6. Conclusions

Computational fluid dynamic (CFD) modeling was used to research the complex flow structures that existed in a novel bioreactor. Owing to the low rotation speed and low Reynolds number, the water in the bioreactor was almost stagnant and the velocity distribution mainly took place in the air phase. The small inlet flows did not have a large effect to the whole system, but provided a good way for medium addition. Shear from air was small and can be considered negligible. In addition, the shear stress caused by the bioreactor was small (the order of magnitude was 10^{-1}), providing a more suitable environment for a large number of cell lines production. The impact from the rotation of outer cylinder proved to be larger than rotating inner cylinder to the bioreactor at low rotational velocity, accounting for the profiles of velocity, shear stress, turbulence kinetic energy (k) and eddy dissipation rate (ε). Besides, in the condition of low rotational speed, the rotating direction of inner cylinders seemed to have minor effect on the maximum value of the shear stress, eddy viscosity, turbulence kinetic energy (k) and eddy dissipation rate (ε). Increasing rotational velocities for the cylinders improved the mixing result of this continuous flow system, in addition, concurrent rotation may yield the best mixing performance.

Nomenclature

a	speed of sound, $a = \sqrt{\gamma R_m T}$, m/s
A	cross-sectional area, m^2
A_0	constant, $A_0 = 4.04$
A_S	constant, $A_S = \sqrt{6}cos\phi$
c_p	specific heat, J/(kg·K)
C_1	constant, $C_1 = max\left[0.43, \frac{\eta}{\eta+5}\right]$
$C_{1\varepsilon}$	constant, 1.44
C_2	constant, 1.9
$C_{3\varepsilon}$	constant, $C_{3\varepsilon} = tanh\left\|\frac{v_{//}}{v_{\perp}}\right\|$
C_μ	constant, $C_\mu = \frac{1}{A_0 + A_S\frac{kU^*}{\varepsilon}}$
D_h	hydraulic diameter, m
F_{Nk}	force per unit volume which exerts on the inclusion, N/ m^3
F'_{Dk}	force per unit volume owing to the relative motion between the phases, N/m^3
g	gravitational acceleration, m/s^2
g_i	ith direction component of the gravitational vector, m/s^2
G_b	generation term due to the buoyancy, $G_b = \beta g_i \frac{\mu_t \partial T}{Pr_t \partial x_i}$ or $G_b = -g_i \frac{\mu_t \partial \rho}{\rho Pr_t \partial x_i}$ (for idea gases), $J/(s\cdot m^3)$ or $kg/(m\cdot s^3)$
G_k	generation term because of the mean velocity gradients, $G_k = -\rho\overline{v_i' v_j'}\frac{\partial v_j}{\partial x_i}$ or $G_k = \mu_t S^2$ (Boussinesq hypothesis), $J/(s\cdot m^3)$ or $kg/(m\cdot s^3)$

I_N	mass interaction term, kg/(m^3·s)
k	turbulence kinetic energy per unit mass, J/ kg^1 or m^2/s^2
k_c	thermal conductivity, W/(m·K)
M_t	turbulent Mach number, $M_t = \sqrt{\frac{k}{a^2}}$
p	pressure, Pa
Pr_t	turbulent Prandtl number, $Pr_t = \frac{\mu c_p}{k}$, the default value of Pr_t for realizable k-ε models is 0.85
P_w	wetted perimeter, m
r_o	radius of outer cylinder, m
r_i	the radius of inner cylinder, m
R_m	gas constant, $R_m = 286$ (for ideal gas), m^2/(s^2·K)
RPM	rotational velocity of the reactor, revolution per minute
$R_{e_{\phi m}}$	Reynolds number
S	modulus of the mean strain rate tensor, $S = \sqrt{2S_{ij}S_{ij}}$, s^{-1}
S_{ij}	mean strain rate, $S_{ij} = \frac{1}{2}\left(\frac{\partial v_j}{\partial x_i} + \frac{\partial v_i}{\partial x_j}\right)$, s^{-1}
S_k	user-defined source term, J/(s·m^3) or kg/(m·s^3)
S_ε	user-defined source term, J/(s·m^3) or kg/(m·s^3)
$\tilde{S}$	$\tilde{S} = \sqrt{S_{ij}S_{ij}}$, s^{-1}
t	time, s
T	temperature, K

U^* $U^* = \sqrt{S_{ij}S_{ij} + \widetilde{\Omega}_{ij}\widetilde{\Omega}_{ij}}$, s^{-1}

$v_{//}$ component of the flow velocity parallel to the gravitational vector, m/s

$v_{\perp}$ component of the flow velocity perpendicular to the gravitational vector, m/s

$\overline{v_i'}$ mean fluctuating velocity ith direction component, m/s

$\overline{v_j'}$ mean fluctuating velocity jth direction component, m/s

$\overrightarrow{v_N}$ velocity vector of phase N, m/s

W constant, $W = \frac{S_{ij}S_{jk}S_{ki}}{\tilde{S}^3}$

Y_M effects from the fluctuating dilatation in the compressible turbulence on the overall dissipation rate, $Y_M = 2\rho\varepsilon M_t^2$, $J/(s \cdot m^3)$ or $kg/(m \cdot s^3)$

Greek Letters

α_N volume fraction of phase N, percent

β thermal expansion, $\beta = -\frac{1}{\rho}\left(\frac{\partial \rho}{\partial T}\right)_p$, K^{-1}

γ ratio of specific heats (adiabatic index), $\gamma = 1.4$ (for calorically perfect air)

δ_N constant, 0 for the disperse phase and 1 for the continuous phase

ε dissipation rate, m^2/s^3

ε_{ijk} permutation symbol, $\varepsilon_{ijk} = \frac{1}{2}(i-j)(j-k)(k-i)$

η constant, $\eta = S\frac{k}{\varepsilon}$

μ molecular dynamic viscosity, Pa-s

μ_t turbulent or eddy viscosity, Pa-s

ν kinematic viscosity, m^2/s

ρ	density of the fluids, kg m^{-3};
ρ_N	density of phase N, kg/m^3
σ_k	turbulent Prandtl number for k, $\sigma_k = 1.0$
σ_ε	turbulent Prandtl number for ε, $\sigma_\varepsilon = 1.2$
τ_{ki}	shear stress, Pa
ϕ	constant, $\phi = \frac{1}{3} cos^{-1}(\sqrt{6}W)$;
ω_k	angular velocity of the moving reference frame, rad/s
Ω_{ij}	$\Omega_{ij} = \overline{\Omega}_{ij} - \varepsilon_{ijk}\omega_k$, s^{-1}
$\overline{\Omega}_{ij}$	mean rate of rotation tensor based on a moving reference frame, $\overline{\Omega}_{ij} = \frac{1}{2}\left(\frac{\partial v_i}{\partial x_j} - \frac{\partial v_j}{\partial x_i}\right)$, s^{-1}
$\widetilde{\Omega}_{ij}$	$\widetilde{\Omega}_{ij} = \Omega_{ij} - 2\varepsilon_{ijk}\omega_k$, s^{-1}
Ω_o	angular velocity of outer cylinder, radians per s

Subscripts

i, j, k	three directions (x, y, z axis) separately
C	continuous phase
D	dispersed phase

References

Abu-Reesh I, Kargi F. 1989. Biological Responses of Hybridoma Cells to Defined Hydrodynamic Shear Stress. *J. Biotechnol.* **9**:167–178.

ANSYS Inc. 2012. ANSYS FLUENT Theory Guide. Canonsburg 46-56 p.

Argyropoulos CD, Markatos NC. 2014. Recent Advances on the Numerical Modelling of Turbulent Flows. *Appl. Math. Model.* **39**:693–732.

Augenstein DC, Sinskey AJ, Wang DIC. 1971. Effect of Shear on the Death of Two Strains of Mammalian Tissue Cells. *Biotechnol. Bioeng.* **13**:409–418.

Bernstein EF, Blackshear PL, Keller KH. 1967. Factors Influencing Erythrocyte Destruction in Artificial Organs. *Am. J. Surg.* **114**:126–138.

Bilgen E, Boulos R. 1973. Functional Dependence of Torque Coefficient of Coaxial Cylinders on Gap Width and Reynolds Numbers. *J. Fluid Engeering* **95**:122–126.

Blackshear PL, Blackshear GL. 1987. Mechanical Hemolysis. In: . *Handb. Bioeng.*, p. 15.1-15.19.

Brennen CE. 2005. Fundamentals of Multiphase Flows. *Cambridge Univ. Press* 19-36 p.

Chisti Y. 2001. Hydrodynamic Damage to Animal Cells. *Crit. Rev. Biotechnol.* **21**:67–110.

Chittur KK, McIntire L V., Rich RR. 1988. Shear Stress Effects on Human T Cell Function. *Biotechnol. Prog.* **4**:89–96.

Dhanasekharan KM, Sanyal J, Jain A, Haidari A. 2005. A Generalized Approach to Model Oxygen Transfer in Bioreactors Using Population Balances and Computational Fluid Dynamics. *Chem. Eng. Sci.* **60**:213–218.

Fayolle Y, Cockx A, Gillot S, Roustan M, Héduit A. 2007. Oxygen Transfer Prediction in Aeration Tanks Using CFD. *Chem. Eng. Sci.* **62**:7163–7171.

Kawase Y, Hashimoto N. 1996. Gas Hold-Up and Oxygen Transfer in Three-Phase External-Loop Airlift Bioreactors: Non-Newtonian Fermentation Broths. *J. Chem. Technol. Biotechnol.* **65**:325–334.

Lathrop DP, Fineberg J, Swinney HL. 1992. Turbulent Flow between Concentric Rotating Cylinders at Large Reynolds Number. *Phys. Rev. Lett.* **68**:1515–1519.

McQueen A, Meilhoc E, Bailey JE. 1987. Flow Effects on the Viability and Lysis of Suspended Mammalian Cells. *Biotechnol. Lett.* **9**:831–836.

Mudde RF, Van Den Akker HE a. 2001. 2D and 3D Simulations of an Internal Airlift Loop Reactor on the Basis of a Two-Fluid Model. *Chem. Eng. Sci.* **56**:6351–6358.

Pérez T, Nava JL. 2013. Simulation of Turbulent Flow of a Rotating Cylinder Electrode. Influence of Using Plates and Concentric Cylinder as Counter Electrodes. *Int. J. Electrochem. Sci.* **8**:4690–4699.

Sarkar S, Lakshmanan B. 1990. Application of a Reynolds Stress Turbulence Model to the Compressible Shear Layer. *AIAA J.* **29**:743–749.

Schmid-schoenbein GW, Fung Y, Zweifach BW. 1975. Vascular Endothelium-Leukocyte Interaction: Sticking Shear Force in Venules. *Circ. Res.* **36**:173–184.

Sukumaran AK, Reji R V., Santhosh KS. 2010. Fluid Flow Simulations within Rotating Annulus. In: . *Proc. 37th Nat. 4th Conf. Fluid Mech. Fluid Power*.

Ziegelstein RC, Cheng L, Capogrossi MC. 1992. Flow-Dependent Cytosolic Acidification of Vascular Endothelial Cells. *Science (80-.).* **258**:656–659.

Chapter 5 - Modeling and Scale-up of a Multiphase Rotating Bioreactor with Improved Oxygen Transfer and Cell Growth

Abstract

A prototype novel multiphase rotating bioreactor with an internal spiroid was shown to offer enhanced oxygen delivery. The scaling rules for this unique design were characterized in modeling and experimental studies. This bioreactor was scaled up from 1.11 x 10^{-4} m^3 to 0.986 x 10^{-3} m^3 to enable evaluation of its potential for cell production. In this novel design the internal spiroid occupying the inside wall of the bioreactor was shown to increase the liquid-gas interface, leading to better oxygen transfer performance. The size (diameter and total volume) of the internal spiroid was also scaled-up corresponding to the increased bioreactor volume thereby increasing the inner surface area by a factor of three. Paired rotatory unions at the reactor inlet and outlet facilitated continuous or batch feeding and continuous measurements of dissolved oxygen and cell number. Oxygen measurements were conducted at different rotational rates to compare the oxygen transfer rates with the original bioreactor with and without the spiroid. Additionally, mathematical models were established to simulate the oxygen transfer rates and obtain the volumetric mass transfer coefficients (k_La). Oxygen transfer increased two times when employing the spiroid. *E. coli* have been selected to demonstrate enhanced biomass production.

Key words: multiphase continuous bioreactor, oxygen transfer, cell cultivation, spiroid

5.1. Introduction

Bioreactors provide the optimal environment for cell culture and play important roles in increasing cell productivity in both scientific and pharmaceutical areas (Health and Kiss, 2007). Previously, a novel continuous bioreactor with significant improvement in gas-liquid transport phenomena has been demonstrated (Fang et al., 2017). The innovative design of spiroid tubing inside the wall of the bioreactor enabled faster oxygen transfer by two times. However, the volume of the previous bioreactor was 1.109×10^{-4} m^3, limiting the capacity of cell culture. Thus, an effective scale-up for this bioreactor is essential for the cell production.

Bioprocesses can occur at four levels: flask level (low working capacity and low cost), laboratory level (preliminary procedures), pilot level (optimal operating conditions) and production level (large scale and financial return) (Lonsane et al., 1992). The scale-up process can be defined as magnifying or transferring the successful mode of the small-scale to large-scale in order to increase the manufacturing potential of the process. A successful scale-up results when the new process can reproduce the process results in the small scale (Diaz and Acevedo, 1999; Hubbard, 1987; Takors, 2012). In scale-up, some parameters are held constant, such as reactor geometry similarity, power consumed per unit volume (P_g/V), volumetric mass transfer coefficient (k_La), maximum shear, and Reynold's Number (Re) (Hewitt and Nienow, 2007; Ju and Chase, 1992; Oldshue, 1966; Schmidt, 2005; Varley and Birch, 1999; Vilaça et al., 2000). These parameters are usually involved in different mechanisms of the bioprocess, thus, the performance and the phenome of the system are considered as the same during the scale-up if some of these parameters are kept constant (Garcia-Ochoa and Gomez, 2009). For aerobic bioprocess in large scale, the criteria consideration of mass transfer is normally aggravated (Gill et al., 2008; Kallos et al., 2003; Marks, 2003; Schmidt, 2005).

The scale-up strategy has always played an important role in the biotechnology and pharmaceutical industry as it is directly related to the large manufacturing applications. Many publications focus on bioprocess scale-up (Gill et al., 2008; Gorenflo et al., 2002; Maranga et al., 2004; Micheletti et al., 2006; Vasconcelos et al., 1998). Chisti scaled up a stirred bioreactor from 0.02 to 0.3 m^3 with similar geometry and taking account of tip speed, Reynold number, specific power input and specific pumping capacity, while maintaining a high concentration for hybridoma cells (Chisti, 1993). Yabannavar et al. scaled a non-clogging spinfilter perfusion bioreactor from 16 liters to 240 liters where the agitation rate and spinfilter speed rate were obtained from maintaining constant power input and ratio of permeation drag to lift drag (Yabannavar et al., 1994). Shukla et al. used the volumetric mass transfer coefficient (k_La) as a standard to scale up the biotransformation process in shake flask (100 ml) to a stirred tank (5 L) which used dual impellers (Shukla et al., 2001). Xing et al. (2009) scaled up a bioreactor with multiple marine impellers for CHO cell culture process to 5,000 L from the bench scale 5- and 20-L bioreactor using parameters of oxygen transfer coefficient, mixing time and carbon dioxide removal rate (Xing et al., 2009).

This research investigated a bioreactor using a spiroid attached to the chamber that was scaled up to 0.986×10^{-3} m^3, or about 9 times of the old version (1.11×10^{-4} m^3). The size of the spiroid tubing inside was also increased accordingly. Oxygen transfer measurements were repeated to characterize the bioreactor and analyze the effects of the spiroid tubing in the larger bioreactor. *E. coli* were grown in a chemostat at several rotational rates and medium flow rates, allowing continuous production.

5.2. Materials and method

5.2.1 Bioreactor Scale-up

Figure 5.1 illustrates the design of the scaled-up bioreactor with the spiroid. This bioreactor has a volume of 0.986 x 10^{-3} m^3, about 9 times of the old version (1.11 x 10^{-4} m^3) (Fang et al., 2017). The dimensions of the bioreactor entrance and exit were maintained in order to use the original hubs. The increase of the volume resulted from doubling the diameter and extending the length from 0.1 m to 0.193 m. The length of the spiroid was also doubled, resulting in 12 turns. The purpose of attaching the spiroid the wall of the bioreactor chamber was to improve the oxygen transport through increasing the gas-liquid contact areas. Spiroid ports are located at the reactor exit and entrance. The detailed comparison of the dimensions between two bioreactors were showed in Table 5.1.

The scaled-up bioreactor maintained similar reactor geometry as the original bioreactor (constant $D_s/D_{R,}$ diameter ratio of the spiroid over bioreactor chamber). By adding the spiroid into the new bioreactor, the internal surface area was increased approximately three times, from 0.0489 m^2 to 0.142 m^2. The surface to volume ratio was changed from 95.9 m^{-1} to 216 m^{-1}. The bioreactor with the spiroid was prototyped using a 3D printer. Two ends were designed to be removable, making the cleaning of the spiroid easier. As the inner cylinder had little impact on the performance under current operating conditions (low rotational rates) (Fang et al., 2017) and was omitted from the scaled-up bioreactor. Additionally, part of the spiroid was embedded in the inside wall of the shell to reduce loss of reactor volume. In place or motors, a roller bed (Model No: 88881003, Thermo Scientific, Waltham, MA, USA) was used to rotate the bioreactor, making it easier to control the rotation rate for the larger bioreactor.

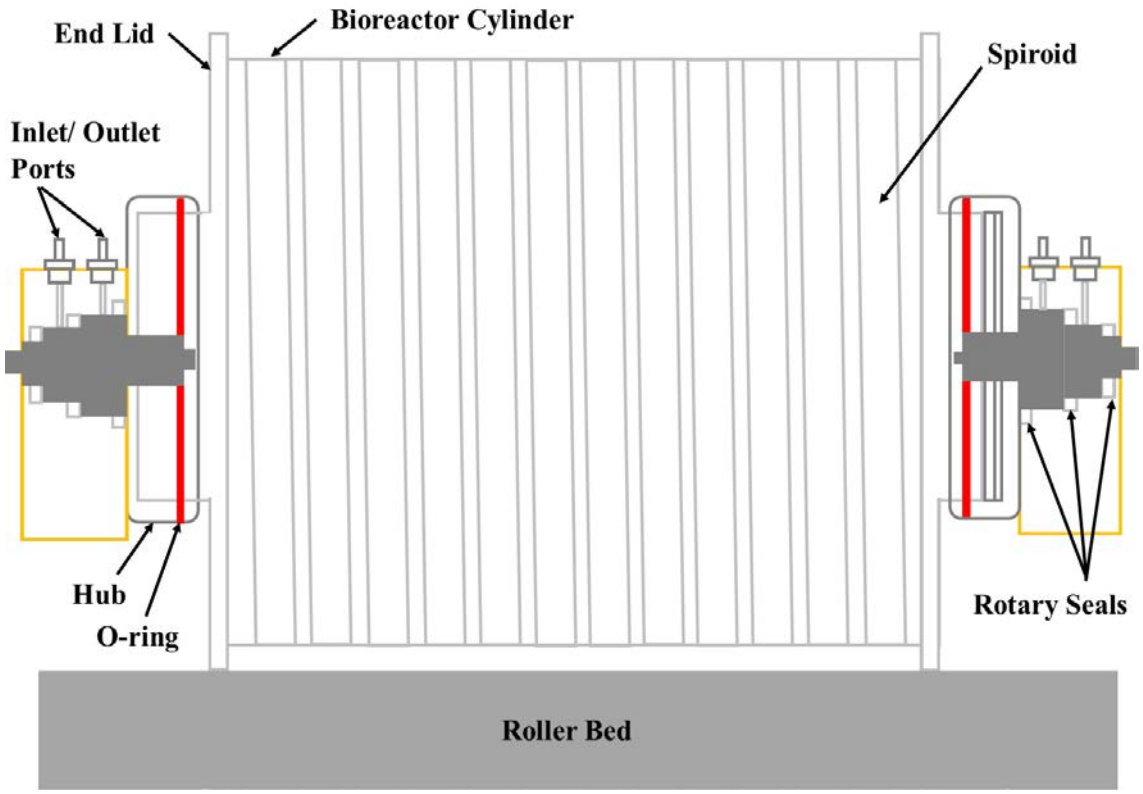

Figure 5. 24. Bioreactor design. For dimensions see Table 5.1.

Table 5. 4. Comparison between two bioreactors (the data for original bioreactor was published (Fang et al., 2017))

	Original Bioreactor	Scaled-up Bioreactor
Chamber Length (m)	0.100	0.193
Chamber Inner Diameter (m)	0.0444	0.0889
Spiroid Length (m)	1.09	3.12
Spiroid Inner Diameter (m)	0.00476	0.00953
Spiroid Turns	8	12
Volume (10^{-4} m^3)	1.11	9.86

5.2.2. Mathematical Modeling for Measuring Gas-liquid Mass Transfer Coefficients k_La

In this research, volumetric mass transfer coefficients (k_La) were calculated from oxygen measurements and were considered as one of the criteria for the scale-up process. The procedures for oxygen measurements has been described in previous published paper (Fang et al., 2017). Ultra-purified water was used in the oxygen experiments and was pre-treated with nitrogen before experiments. Meanwhile, the oxygen was aerated through the reactor for a long period of time before experiments. The pretreated water was pumped into the system at high flow rate to reduce the contact time with oxygen. Tubes were reconnected to create a closed system so that fluids can flow through a micro oxygen probe connected to the outlet of the bioreactor (MI-730, Microelectrodes Inc., Bedford, New Hampshire, USA). Oxygen data was measured automatically and periodically by the oxygen electrode. Mathematical models were established to fit the oxygen data and to calculate the volumetric mass transfer coefficients (k_La) for bioreactor with and without the spiroid.

To determine the volumetric mass transfer coefficients (k_La) in the reactor without a spiroid loop, oxygen data were measured when both inlet and outlet of the spiroid were plugged, and then the collected data were fitted into the mass balance equation for batch system directly:

$$\frac{dc_L}{dt} = k_L a(c_L^* - c_L) \quad (5\text{-}44)$$

Rearranging,

$$c_L = c_{L.}^* - (c_{L.}^* - c_{L0})\exp(-k_L at) \quad (5\text{-}45)$$

When the spiroid is used, fluid from the reactor enters the spiroid near the reactor exit and is pumped to the reactor inlet. The process was illustrated in Figure 5.2.

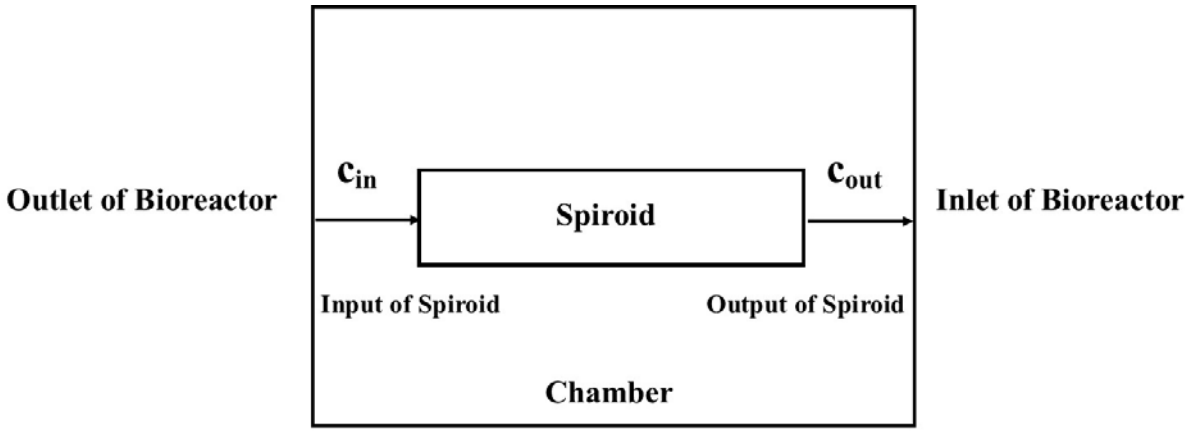

Figure 5.25. Circulation Process

To simplify the calculation, two mass balance equations were established for the spiroid loop and the chamber, respectively. For mass balance in the spiroid loop, the spiroid loop was treated as a long tube with inlet and outlet as shown in Figure 5.2 (Fang et al., 2017):

$$\frac{v}{V_{sp}}(c_{in} - c_{out}) + k_L a_{sp}(c_L^* - c_{out}) = \frac{dc_{out}}{dt} \quad (5\text{-}46)$$

For simplified calculation, the mass balance in the chamber was written using the same form of the inlet and outlet of the spiroid as:

$$\frac{v}{(V_r - V_{sp})}(c_{out} - c_{in}) + k_L a_c(c_L^* - c_{in}) = \frac{dc_{in}}{dt} \quad (5\text{-}47)$$

With negligible dynamic lag in the spiroid from experimental observation, the boundary conditions for these two mass balance equations are:

$$c_{in}(t = 0) = c_{L0} \quad (5\text{-}48)$$

$$c_{out}(t = 0) = c_{L0} \quad (5\text{-}49)$$

Thus, by fitting the models with the collected experimental data using non-linear regression method, the volumetric mass transfer coefficients for the spiroid loop ($k_L a_{sp}$) and the chamber ($k_L a_c$) can be estimated.

5.2.3. Bacterial culture

5.2.3.1 Strain and Medium

The bacteria used in this research was *E. coli* (K91BlueKan) from Dr. Allen David's laboratory (Department of Chemical Engineering, Auburn University, AL, USA). The medium used for *E. coli* was NZY medium, which contained 10 g casein hydrolysate enzymatic (MP Biomedicals, LLC, Santa Ana, California, USA), 5 g yeast extract (AMRESCO, Inc., Solon, OH, USA), 5 g sodium chloride (AMRESCO, Inc., Solon, OH, USA) per liter. The pH of NZY medium was adjusted to 7.5 by using 5M sodium hydroxide (Alfa Aesar, Haverhill, MA, USA), and then the medium was autoclaved before use. Glucose (AMRESCO, Inc., Solon, OH, USA) was added to the medium to reach the final concentration of 5 $g \cdot L^{-1}$.

5.2.3.2. Operating Conditions

E. coli was precultured in shake flask at 200 rpm and 37°C using NZY medium with 0.1 $g \cdot L^{-1}$ Kanamycin sulfate (to reduce contamination) (Corning Inc., Corning, NY, USA) overnight. The overnight culture was expanded to shake flask propagation again and then adjusted to OD_{600} of 0.1 before transferring into the bioreactor. Bioreactor was operated in the batch mode first for three hours, and then the continuous mode with different rotational rates (6 rpm and 8 rpm) and different fresh medium flow rates (0.6 $ml \cdot min^{-1}$, 1.5 $ml \cdot min^{-1}$ and 3 $ml \cdot min^{-1}$) was enabled.

Exponential growth in the batch could be described as:

$$\frac{1}{X}\frac{dX}{dt} = \mu \qquad (5\text{-}50)$$

where X is the biomass concentration (dry weight per unit volume, $g \cdot L^{-1}$) at time t (hr); μ is the specific growth rate (hr^{-1}). The exponential equation was only applied when the substrates are in excess (Herbert et al., 1956).

In addition, if the feed media are sterile, the changes of bacterial concentration in a continuous system (or a chemostat) could be described as follows (Herbert et al., 1956; Jannasch et al., 1969):

$$\frac{dX}{dt} = \mu X - DX \qquad (5\text{-}51)$$

where D is the dilution rate (hr^{-1}). When the specific growth rate is less than the dilution rate, the cells cannot maintain the concentration and will be washed out; if the growth rate is equal to dilution rate, the system reached steady state, i.e. cells maintain a constant concentration. Thus, through manipulating the dilution rate, the growth rate could be controlled.

The process flow diagram was showed in Figure 5.3. Oxygen was provided to the system periodically by aeration along with venting to approximately maintain the constant oxygen level in the bioreactor. After three hours, fresh medium was pumped into the bioreactor and the same amount of the culture was removed to maintain the constant volume. The components in the flow medium was the same as the basal medium.

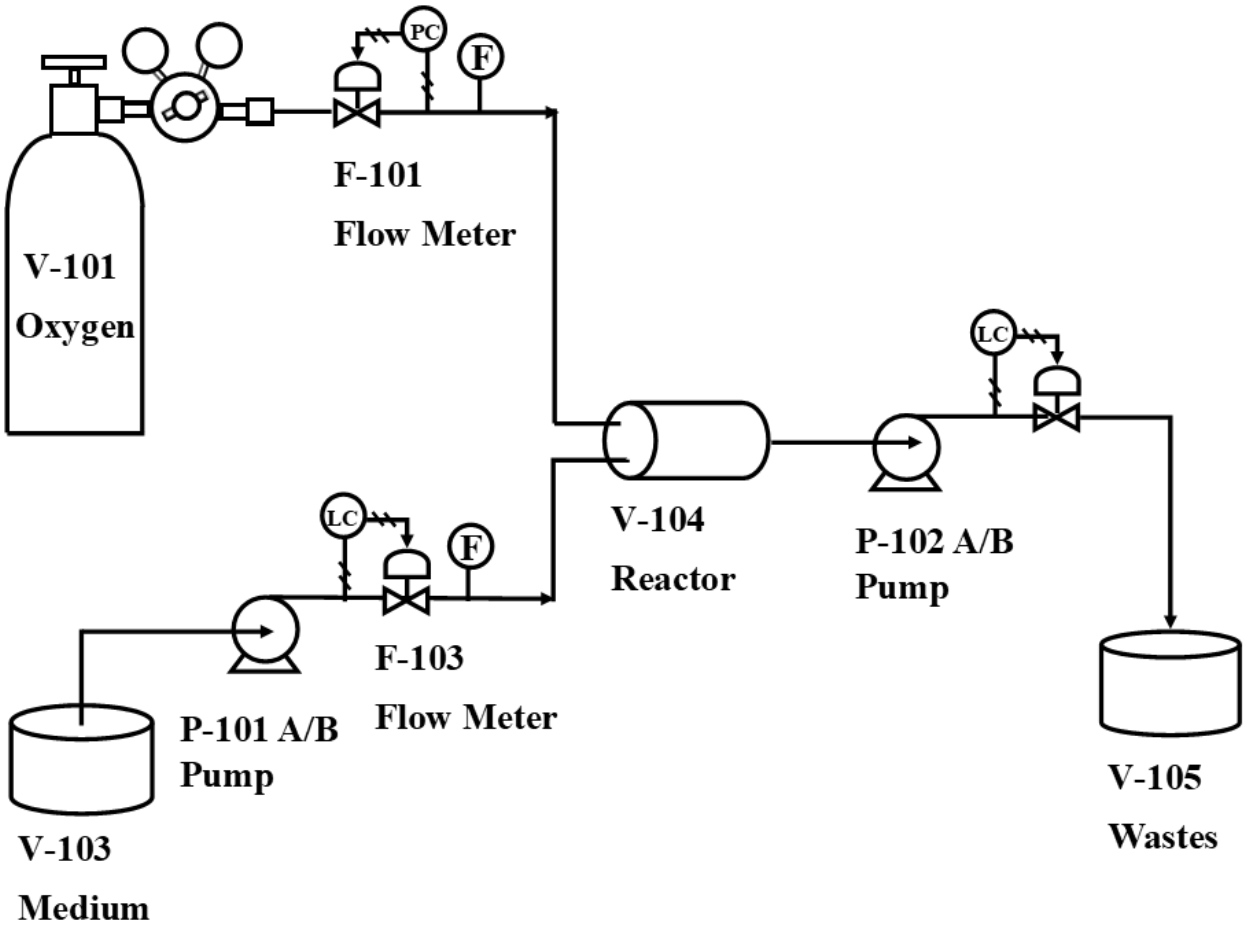

Figure 5.26. Process flow diagram for the bacterial culture experiments.

5.2.3.3. Analytical Methods

The growth of E. coli was monitored by measuring OD_{600} of culture samples using SpectraMax® i3 Multi-Mode Microplate Reader (Molecular Devices, LLC, San Jose, CA, USA). Glucose consumption in the culture was measured by using a glucose monitor (GM100, BioReactor Sciences, Inc., Lawrenceville, GA, USA).

5.3. Results and Discussion

5.3.1. Oxygen Measurements

The normal rotational rates for roller bottle is less than 10 rpm, thus, rotation speeds were selected at 2 rpm, 4 rpm, 6 rpm and 8 rpm. At least five experiments were conducted and averaged for each operating condition in order to reduce the experimental error. Experimental data was fit to theoretical models using nonlinear regression.

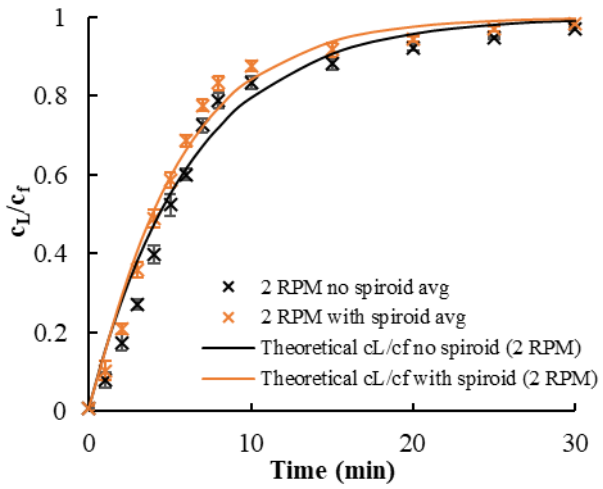

(a) Dissolved oxygen profile under 2 rpm

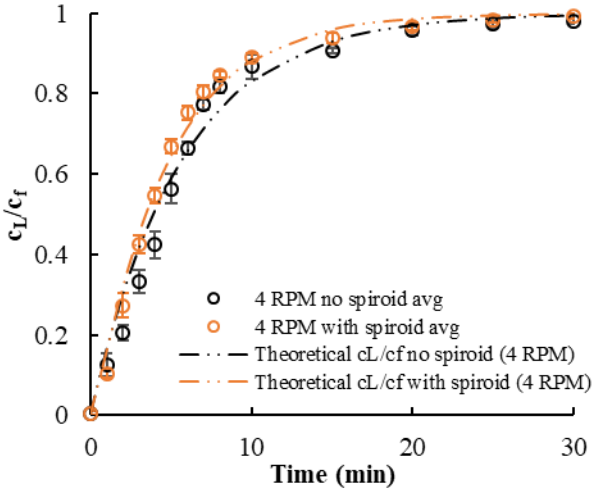

(b) Dissolved oxygen profile under 4 rpm

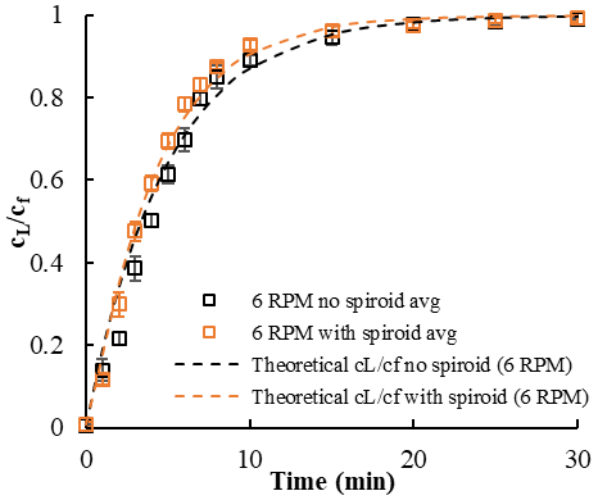

(c) Dissolved oxygen profile under 6 rpm

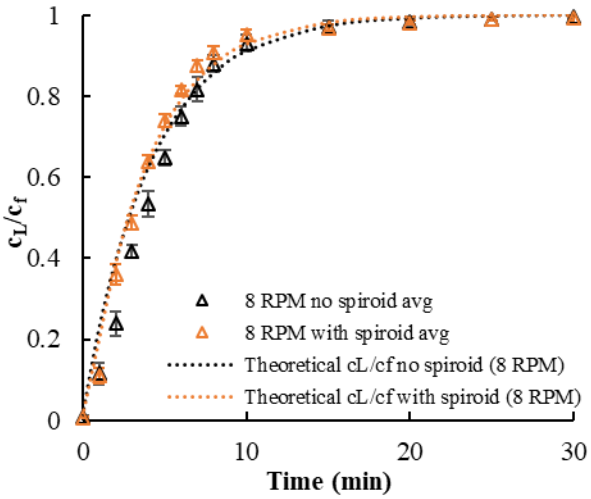

(d) Dissolved oxygen profile under 8 rpm

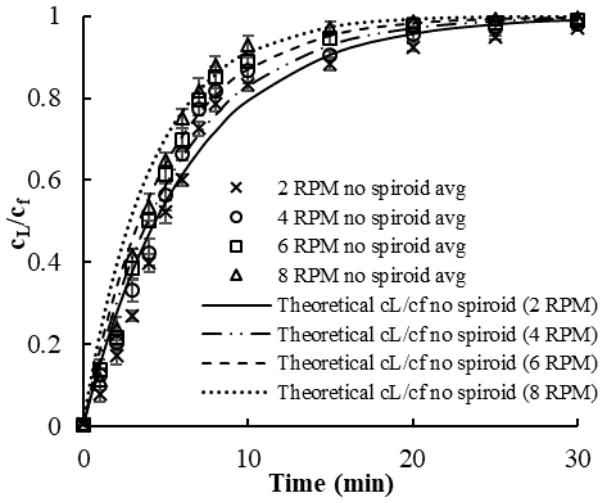

(e) Dissolved oxygen profile (no spiroid)

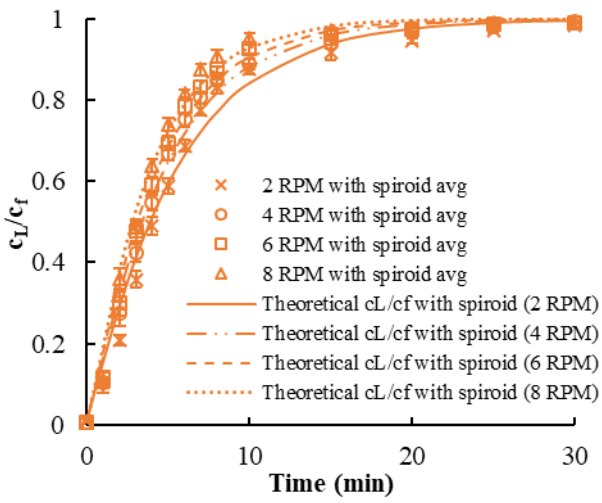

(f) Dissolved oxygen profile (with spiroid)

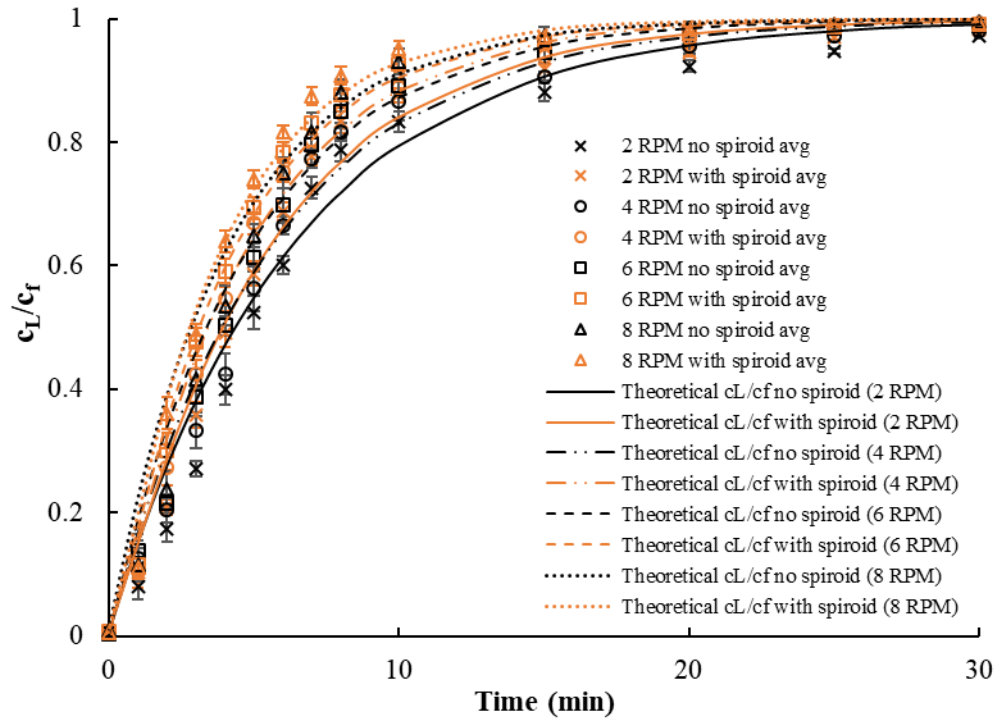

(g) Dissolved oxygen profile under various operating conditions

Figure 5.27. Dissolved oxygen concentration curve in the bioreactor with and without spiroid.

Adding the spiroid to the system improved the oxygen transfer rate, decreasing the oxygen saturation time. However, the positive impact of the spiroid lessened as the rotation speed increased as shown in Figure 5.4 (a) to (d). The most significant difference between the system with spiroid and without spiroid occurred at 2 rpm and 4 rpm. Spiroid improved the oxygen transfer phenomenon by a factor of around two under 2 rpm and 4 rpm, while the factor is only 1.3 under 8 rpm. The oxygen transfer in the bioreactor with spiroid consisted of mass transfer both in chamber and spiroid. The increase of the mass transfer in the chamber at higher rotational rate weakened the effect of the spiroid as the liquid volume in the chamber was much higher. Both Figure 5.4 (e) and (g) showed that oxygen reached saturation state faster with higher rotational rates. However, the positive effect of increasing rotational speed on oxygen data in the bioreactor with spiroid was not as significant as that in the one without spiroid.

Table 5.2 and Figure 5.5 summarized the volumetric mass transfer coefficients obtained from the modeling under various conditions. Through one-way analysis of variance (ANOVA), the P-value of the F-test is less than 0.05, thus, there is a statistically significant difference between the k_La values under four variables (four different rotational rates) for bioreactor with and without spiroid at the 95.0% confidence level. All the k_La values seemed to have a positive linear relation to the rotational speeds, and the rotational speed had the largest impact on kla value in the spiroid over other cases. The values of volumetric mass transfer coefficients are much higher in spiroid than in chamber (no spiroid) due to higher interfacial area than that in the chamber. The k_La values in spiroid were about seven times of that in bioreactor without spiroid, however, this increase of k_La from spiroid only improved the oxygen transport in the overall system by a factor of 1.5 at maximum. The k_La values in the large-scale bioreactor with spiroid were about 14% less than that in the small scale, which could be due to the smaller interfacial

area per unit volume (or surface area to volume ratio) in the large scale as it removed the inner cylinder. However, the results still showed promising advantages by using spiroid as a method of improving oxygen transfer and the volume of the large scale (around 1 L) also enables the potentials in cell culture.

Table 5.5. Summary of the volumetric mass transfers (k_La)

Liquid Fraction	Outer Cylinder (RPM)	k_La (s^{-1}) without spiroid	k_La (s^{-1}) with spiroid	k_La (s^{-1}) in spiroid
2/3	2	0.00263	0.00311	0.0132
	4	0.00296	0.00344	0.0184
	6	0.00342	0.00394	0.0227
	8	0.00401	0.00441	0.0276

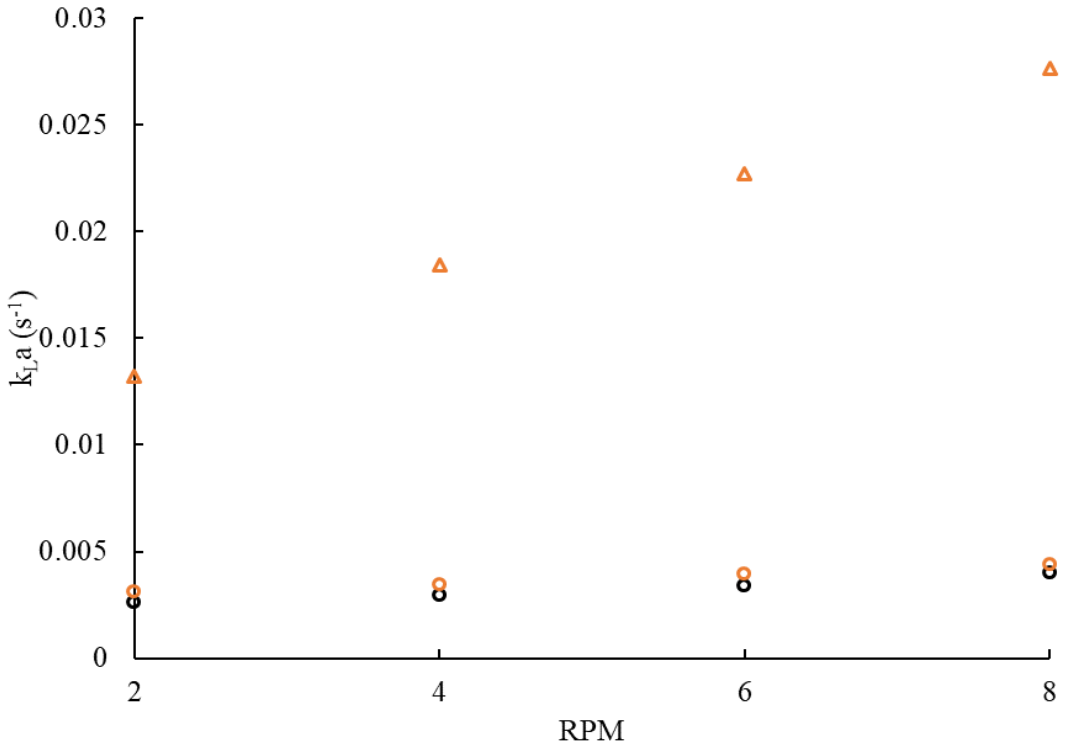

Figure 5.28. Comparison of k_La values in the bioreactor with and without the spiroid: ○: k_La for the bioreactor without spiroid; ○: k_La for the bioreactor with spiroid; Δ: k_La in the spiroid loop.

5.3.2. Bacterial Culture Results

E. coli growth and yield were relatively low under 2 RPM in the preliminary experiments which could be due to the poor mixing and low oxygen delivery. Thus, rotation rates of 6 rpm and 8 rpm were selected for these tests. The bioreactor was first operated in the batch mode for three hours and then changed to continuous mode. Three flow rates (0.6 $ml \cdot min^{-1}$, 1.5 $ml \cdot min^{-1}$ and 3 $ml \cdot min^{-1}$) were used in the continuous mode to demonstrate different steady state levels. The mean residence time could also be calculated based on flow rates and the liquid volume in the bioreactor.

Duplicate bacterial experiments were conducted for each condition. Cells grew in the exponential phase in the batch and eventually reached the steady state with continuous flow as in both biomass growth profiles and the glucose consumption profiles. Figure 5.6 (a) illustrates the different steady state levels controlled by flow rate. The batch growth curves were consistent; in the continuous mode, the steady state concentration decreased with increased flow rates. Cells in the bioreactor decreased because of inlet flows until the growth rate matched the dilution rates, and constant concentration was maintained at steady state. Maintaining higher concentration leads to lower glucose level or lower substrate level in the system (Figure 5.6 (b)). Though the biomass concentration was maintained at lower level through higher flow rates, the amount of harvest cells in the case of 3ml/min was the maximum among three flow rates in the long-term aspects (Table 5.3). For a 24-hour steady-state operation, the production rate at 3 ml min^{-1} is about 3.4 times larger than the production rate 0.6 $ml \cdot min^{-1}$.

Figure 5.6 (c) showed the effect of different rotational rates (6 rpm and 8 rpm) on the cell growth. As from the previous oxygen measurements, enhanced oxygen delivery was achieved by using higher rotation rates. While keeping other parameters as constant, cell growth under 6

rpm was slower than that under 8 rpm (growth rate of 0.365 hr^{-1} versus 0.398 hr^{-1}) in the batch mode. Additionally, lower oxygen deliver capacity leads to lower steady state concentration in the low rotational rates (0.112 $g \cdot L^{-1}$) comparing to that in high rotational rates (0.12 $g \cdot L^{-1}$).

In Figure 5.6 (e), *E. coli* grows faster in the system with the spiroid for the first three hours in batch (growth rate of 0.398 hr^{-1} over 0.362 hr^{-1} as summarized in Table 5.3). The difference between two systems within the first three hours in the batch could be attributed to the enhanced oxygen delivery using the spiroid. The biomass was increased by 15% by using spiroid in the batch. Additionally, a two-hour process with spiroid could be used to replace a three-hour process without spiroid in the batch, which shorten the operating time by 33%. However, when the flow was established, there was no major difference between two systems in both biomass steady state concentration (Figure 5.6 (e)) and overall glucose consumption profile (Figure 5.6 (f)). The possible reasons could be summarized into two aspects: the fresh incoming medium provided extra aqueous/dissolved oxygen to the cell culture; the oxygen transfer was mainly due to the mass transfer in chamber at higher rotation rate or the effect of spiroid was weaken at higher rotation rate as from previous oxygen measurement.

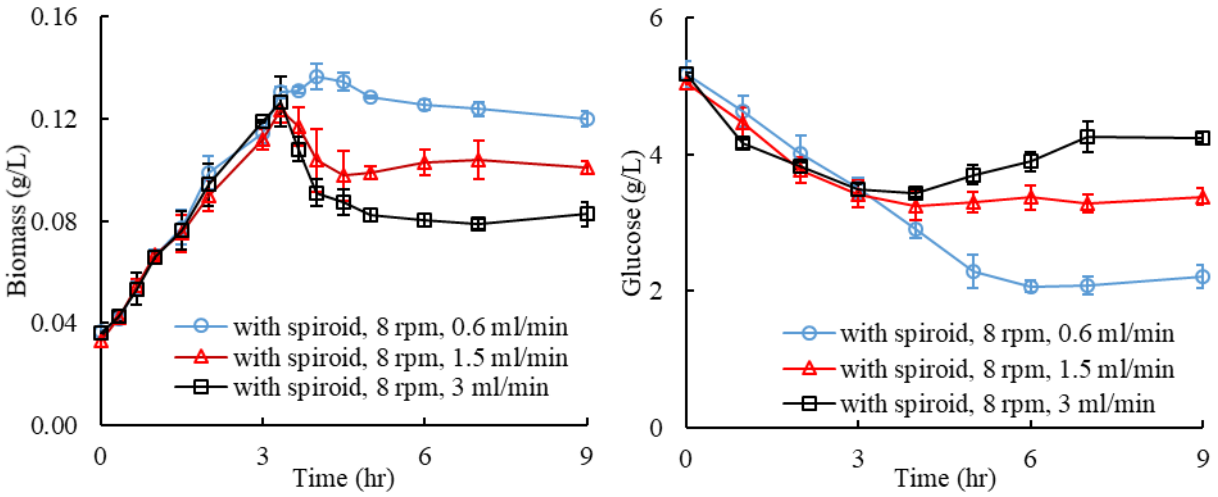

(a) Growth curve (various flow rates)

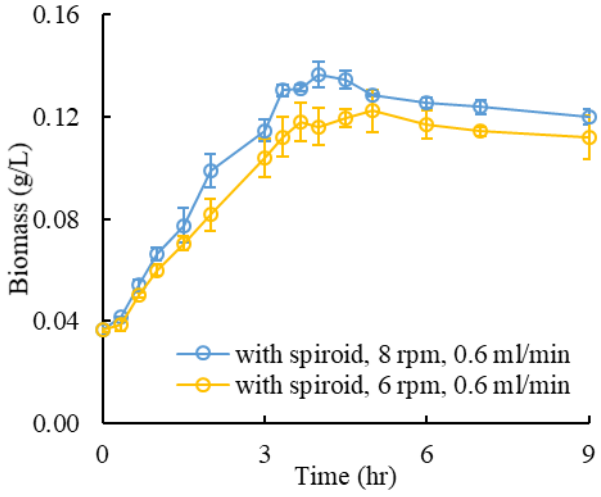

(b) Glucose profile (various flow rates)

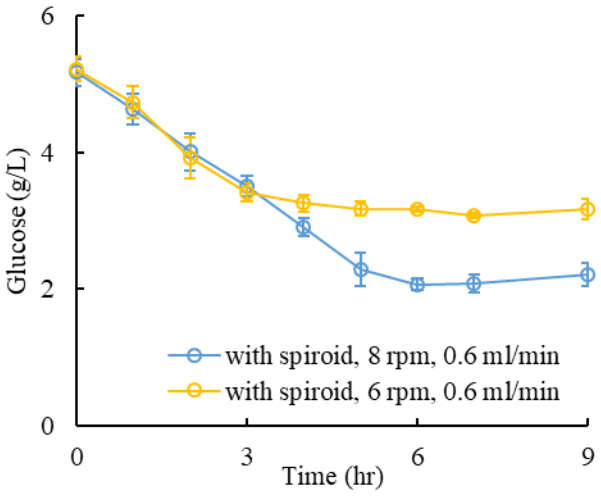

(c) Growth curve (various rotation rates)

(d) Glucose profile (various rotation rates)

(e) Growth curve (with and without spiroid)

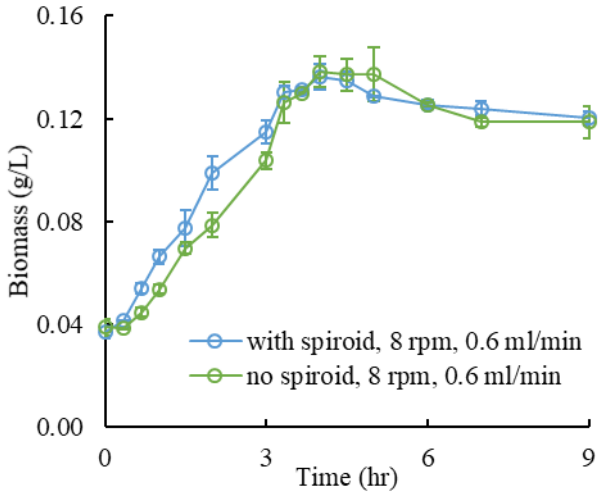

(f) Glucose profile (with and without spiroid)

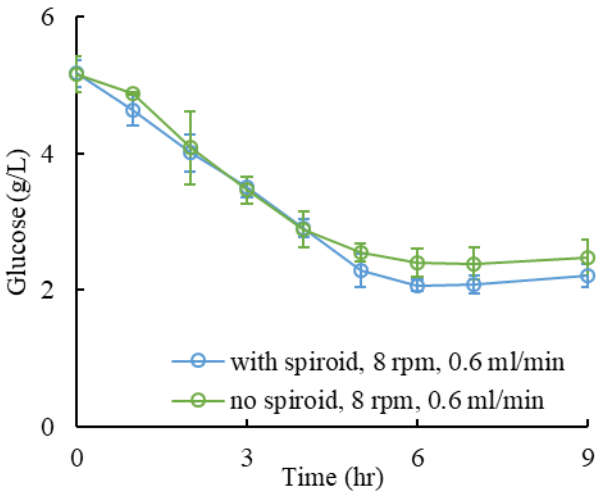

Figure 5.29. Bacterial growth curve and glucose profile in bioreactor with and without the spiroid

Table 5.6. Summary of the parameters in bacterial experiments

	rpm	μ, batch (hr^{-1})	F ($ml \cdot min^{-1}$)	D (hr^{-1})	τ, mean residence time (hr)	Harvest cells, 24 hours (g)
with spiroid	6	0.365	0.6	0.09	11.1	0.097
	8	0.398	0.6	0.09	11.1	0.104
	8	0.394	1.5	0.23	4.4	0.218
	8	0.404	3	0.45	2.2	0.358
no spiroid	8	0.362	0.6	0.09	11.1	0.103

5.4. Conclusions

Scale up techniques are commonly used in the bioprocessing. This paper investigated a bioreactor with enhanced oxygen transfer by adding spiroid loop to the wall of the bioreactor. This bioreactor was scaled up from a previously demonstrated bioreactor by about nine times from 1.11 x 10^{-4} m^3 to 0.986 x 10^{-3} m^3 to enable its potential for cell production. The performance of the bioreactor was characterized by measuring oxygen data and volumetric mass transfer coefficients (k_La). The comparison between the results of the bioreactor with and without spiroid loop provided support for the advantages of using spiroid loop. For this new bioreactor, adding the spiroid loop reduced the oxygen saturation time by half at maximum under current operating conditions. Furthermore, some biological tests were also used in this bioreactor to verify the potential of the cellular production in this bioreactor. The results from *E. coli* experiments not only verified the advantages of the spiroid in oxygen delivery, but also showed the feasibility of continuous operation in our bioreactor, which enabled the continuous biomass harvest. Some further work still could be done basing on optimizing the design of spiroid loop to increase the interfacial area as the k_La values in the new bioreactor were still less than that of the old version (small bioreactor). Other cells lines, especially those that are more

shear sensitive, could also be tested in this bioreactor to explore the potential of this design for other cell culture applications.

Nomenclature

c_{L0}	initial dissolved oxygen concentration in liquid phase, mol·L^{-1}
c_L	dissolved oxygen concentration in liquid phase (water), mol·L^{-1}
c_L^*	saturated oxygen concentration in liquid phase at certain temperature, mol·L^{-1}
c_f	final dissolved oxygen concentration in the bioreactor, mol·L^{-1}
c_{in}	dissolved oxygen concentration entering spiroid loop, mol·L^{-1}
c_{out}	dissolved oxygen concentration exiting from spiroid, mol·L^{-1}
D	dilution rate, hr^{-1}
F	Flow rate, ml·min^{-1}
$k_L a$	volumetric gas-liquid mass transfer coefficient, s^{-1}
$k_L a_C$	volumetric gas-liquid mass transfer coefficient in bioreactor chamber, s^{-1}
$k_L a_{sp}$	volumetric gas-liquid mass transfer coefficient in spiroid loop, s^{-1}
rpm	rotational velocity of the reactor, revolution per minute
t	time, s
v	volumetric flow rate through spiroid loop, L·s^{-1}
V_r	liquid volume of bioreactor, m^3
V_{sp}	liquid volume of spiroid tube, m^3
X	biomass concentration, dry weight per unit volume, g·L^{-1}
μ	specific growth rate, hr^{-1}
τ	mean residence time, hr

References

Chisti Y. 1993. Animal cell culture in stirred bioreactors: observations on scale-up. *Process Biochem.* **28**:511–517.

Diaz A, Acevedo F. 1999. Scale-up strategy for bioreactors with Newtonian and non-Newtonian broths. *Bioprocess Eng.* **21**:21–23.

Fang S, Todd PW, Hanley TR. 2017. Enhanced oxygen delivery to a multiphase continuous bioreactor. *Chem. Eng. Sci.* **170**:597–605.

Garcia-Ochoa F, Gomez E. 2009. Bioreactor scale-up and oxygen transfer rate in microbial processes: An overview. *Biotechnol. Adv.* **27**:153–176.

Gill NK, Appleton M, Baganz F, Lye GJ. 2008. Quantification of power consumption and oxygen transfer characteristics of a stirred miniature bioreactor for predictive fermentation scale-up. *Biotechnol. Bioeng.* **100**:1144–1155.

Gorenflo VM, Smith L, Dedinsky B, Persson B, Piret JM. 2002. Scale-up and optimization of an acoustic filter for 200 L/day perfusion of a CHO cell culture. *Biotechnol. Bioeng.* **80**:438–444.

Health C, Kiss R. 2007. Cell culture process development: advances in process engineering. *Biotechnol Prog.* **23**:46–51.

Herbert D, Elsworth R, Telling RC. 1956. The continuous culture of bacteria; a theoretical and experimental study. *J. Gen. Microbiol.* **14**:601–622.

Hewitt CJ, Nienow AW. 2007. The scale-up of microbial batch and fed-batch fermentation processes. *Adv. Appl. Microbiol.* **62**:105–135.

Hubbard DW. 1987. Scaleup Strategies for Bioreactors Containing Non-Newtonian Broths. *Ann. N. Y. Acad. Sci.* **506**:600–606.

Jannasch HW, Sp. P, Marinorubra S. 1969. Estimations of bacterial growth rates in natural waters. *J. Bacteriol. 1 ; 156-160* **99**:156–160.

Ju LK, Chase GG. 1992. Improved scale-up strategies of bioreactors. *Bioprocess Eng.* **8**:49–53.

Kallos MS, Sen A, Behie LA. 2003. Large-scale expansion of mammalian neural stem cells: A review. *Med. Biol. Eng. Comput.* **41**:271–282.

Lonsane BK, Saucedo-Castaneda G, Raimbault M, Roussos S, Viniegra-Gonzalez G, Ghildyal NP, Ramakrishna M, Krishnaiah MM. 1992. Scale-up strategies for solid state fermentation systems. *Process Biochem.* **27**:259–273.

Maranga L, Cunha A, Clemente J, Cruz P, Carrondo MJT. 2004. Scale-up of virus-like particles production: Effects of sparging, agitation and bioreactor scale on cell growth, infection kinetics and productivity. *J. Biotechnol.* **107**:55–64.

Marks DM. 2003. Equipment design considerations for large scale cell culture. *Cytotechnology* **42**:21–33.

Micheletti M, Barrett T, Doig SD, Baganz F, Levy MS, Woodley JM, Lye GJ. 2006. Fluid mixing in shaken bioreactors: Implications for scale-up predictions from microlitre-scale microbial and mammalian cell cultures. *Chem. Eng. Sci.* **61**:2939–2949.

Oldshue JY. 1966. Fermentation mixing scale-up techniques. *Biotechnol. Bioeng.* **8**:3–24.

Schmidt FR. 2005. Optimization and scale up of industrial fermentation processes. *Appl. Microbiol. Biotechnol.* **68**:425–435.

Shukla VB, Parasu Veera U, Kulkarni PR, Pandit AB. 2001. Scale-up of biotransformation process in stirred tank reactor using dual impeller bioreactor. *Biochem. Eng. J.* **8**:19–29.

Takors R. 2012. Scale-up of microbial processes: Impacts, tools and open questions. *J. Biotechnol.* **160**:3–9.

Varley J, Birch J. 1999. Reactor design for large scale suspension animal cell culture. *Cytotechnology* **29**:177–205.

Vasconcelos JMT, Alves SS, Nienow AW, Bujalski W. 1998. Scale-up of mixing in gassed multi-turbine agitated vessels. *Can. J. Chem. Eng.* **76**:398–404.

Vilaça PR, Badino Jr. a. C, Facciotti MCR, Schmidell W. 2000. Determination of power consumption and volumetric oxygen transfer coefficient in bioreactors. *Bioprocess Eng.* **22**:0261–0265.

Xing Z, Kenty BM, Li ZJ, Lee SS. 2009. Scale-up analysis for a CHO cell culture process in large-scale bioreactors. *Biotechnol. Bioeng.* **103**:733–746.

Yabannavar VM, Singh V, Connelly N V. 1994. Scaleup of spinfilter perfusion bioreactor for mammalian cell retention. *Biotechnol. Bioeng.* **43**:159–164.

Chapter 6 - Summary

A novel bioreactor with low shear and enhanced oxygen transfer performance was successfully demonstrated. The bioreactor was not entirely filled. This created a multiple microenvironment encountered by the cultured cell line. The multiphase environment proved to be beneficial for improving the gas-liquid transport phenomena. Enhanced gas and nutrient mass transfer resulted from the unique design, which included a spiroid tube. The spiroid tube was attached to the wall of the bioreactor's outer cylinder to increase gas-liquid contact area, thereby improving oxygen transfer.

Computational fluid dynamic (CFD) modeling was used to predict the complex flow structures in this novel bioreactor. The results from the CFD simulations showed the rotating inner cylinder had little effect on the overall system (velocity profile, shear stress, turbulence kinetic energy (k) and eddy dissipation rate (ε)) and assisted in selecting the experimental conditions for oxygen measurements (mainly test rotating outer cylinder). A mathematical model was also created to calculate the volumetric mass transfer coefficients (kLa) from oxygen data at different operating conditions (2 RPM, 4 RPM, 6 RPM and 8 RPM) for bioreactor with and without the spiroid.

Experiments were conducted to measure oxygen profile for the bioreactor with and without the spiroid under different operating conditions (2 RPM, 4 RPM, 6 RPM and 8 RPM). The comparison verified the advantages of using the spiroid. There was a direct relationship between OTP and rotational rate. To increase the cell culture capacity, the bioreactor was scaled up by nine times (from 1.11×10^{-4} m^3 to 0.986×10^{-3} m^3) and oxygen measurements were repeated in the large-scale bioreactor. The oxygen measurements showed adding spiroid could help improved the oxygen delivery by two time. E. coli was cultured in the bioreactor to further

investigate the novel behavior of the spiroid in enhancing oxygen transfer. E. coli was found to grow faster in the bioreactor with the spiroid. The bioreactor was operated in the batch mode and then changed to continuous mode under various conditions (various flow rate of 0.6 $ml \cdot min^{-1}$, 1.5 $ml \cdot min^{-1}$ and 3 $ml \cdot min^{-1}$at different rotation rate 6 RPM and 8 RPM).

There is still some optimization work that could be done in the future. Although the volumetric mass transfer coefficients (k_La) in the spiroid were larger than that in the bioreactor without spiroid, adding the spiroid to the bioreactor only increased the overall oxygen transfer in the system by a factor of twofold. Optimization should focus on developing simulation models to predict and analyze the relationship between design of the spiroid (diameter and length) to obtain the optimal design with the spiroid. This bioreactor could also be used to produce large number of cells for shear sensitive cell lines and related antibody production.